Hydrogen Burning of ^{17}O

by
Joseph Newton

A dissertation submitted to the faculty of the University of North Carolina at Chapel Hill in partial fulfillment of the requirements for the degree of Doctor of Philosophy in the Department of Physics and Astronomy.

Chapel Hill
2010

Approved by:

Christian Iliadis, Advisor

Arthur Champagne, Reader

Gerald Cecil, Reader

Jonathan Engel, Reader

Reyco Henning, Reader

ABSTRACT

Joseph Newton: Hydrogen Burning of ^{17}O.
(Under the direction of Christian Iliadis.)

Classical novae are explosive binary systems involving the accretion of hydrogen rich material from a main sequence star onto the surface of a white dwarf partner, reaching peak temperatures of T = 0.1-0.4 GK. Observed elemental abundances from the ejecta provide much needed constraints for the modeling of these explosions. Novae are thought to be the most significant source of ^{15}N and ^{17}O in the universe. The ^{17}O(p,γ)^{18}F and ^{17}O(p,α)^{14}N reactions have an important effect on nucleosynthesis in novae, since they determine the creation and destruction of ^{17}O and ^{18}F, which produces detectable γ-radiation. The dominant contributor to the ^{17}O(p,α)^{14}N reaction is a resonance at E_r^{lab} = 193 keV. The strength of this resonance has been measured and the results are presented. For the ^{17}O(p,γ)^{18}F reaction, the dominant contribution comes from the nonresonant direct capture process. The literature direct capture cross sections currently differ by a factor of two. This cross section has been measured in the current work and the results are also presented. New reaction rates have been calculated with these measured cross sections using a new Monte Carlo technique and these new rates have significantly reduced uncertainties compared to the current literature.

”Remember, man, that you are dust

and to dust to you will return.”

Genesis 3:19

ACKNOWLEDGMENTS

Christian, thank you for being a truly great advisor and teacher. Your support and guidance has been incredible and I appreciate every bit of it. Thank you for always having time to answer my questions and for showing enthusiasm for my project. Thank you for always encouraging me and pushing me to go further. You have made my time in graduate school a wonderful, exciting and memorable experience. I could not have asked for a better advisor.

Art, thank you for always having an open door and for all the time you spent helping me at LENA. Thank you for always having time to answer questions and for all the physics that you have taught me. You are an amazing teacher and I am sincerely grateful for having you to talk to.

Rich, thank you for everything. I cannot possibly do you justice in a few sentences. You have been with me through it all and I could not have finished this work without you. Thank you for fixing my computer, the countless hours we spent chasing broken cables at LENA, the overnight shifts taking data, all the tea that I stole from you and all the other help and support you have given me. Most of all, thank you for always just being there. You are a true friend despite the fact that you say aluminium.

To my bistros: Thank you guys. You have been my friends, my heros, and the ones that made me smile through everything. Thank you for sitting shifts and nights on Franklin Street. Johnny, thank you for always having time to help me in the lab, for going for wings with me, for teaching me to make awesome shop drawings, and for all of your advice. Stephen, thank you for being so tall, for trips to the disc golf course, for all of your detector help, for always keeping me honest and for checking my grace plots. I could not have two better friends and thanks again, especially, for my brofile.

Charles, thank you for being my roommate, my officemate, my teammate and my friend. You are truly one of the good guys and I am blessed to have you around. You make me laugh like no else that I know. Thank you for always being there for me and for giving me the tough word when I need to hear it.

Tim and Mitzi, thank you two for all that you have done for me. Thank you for always being there to talk out ideas and problems. Thank you for Monday Night Pints and trips to the Bryan Center. Tim,

thank you for all the second breakfasts when I needed a break and the advice when I had a problem. Mitzi, thank you for your qualifier notes; I would not have passed without them. Thank you two for your friendship in and out of the lab. It has meant a lot to me.

Peter, thank you for coming back to grad school. It was truly a pleasure getting to know you. Thank you for providing trips to Notre Dame and for allowing me to never have to be the senior graduate student. Thank you for all of your help with my research and for being such a good friend.

Dr. Fox, thank you for teaching me so much. You have always been a great source of knowledge, experience and advice for me. You are a great friend and I wish I got to see you more. Claudio, thank you for all of your help with my experiments and for always having time to answer questions for me. I thoroughly enjoyed having you as a neighbor and friend.

Bret, Patrick and Alex, thank you guys for all of your support. Thank you for always having time to help and teach me and for the many hours you have spent fixing my computer and electronics. I could not have done it without you.

Chris, John, Richard and Jeff, thank you for all of your help pulling cables, fixing pumps and all other sorts of things. Thank you for always having a second to come answer questions and teach me how things work. Thank you for helping to keep the lab working. Hey John, GO SEC!

Lauren, thank you for being you. Thank you for putting up with me while I wrote this thesis. Thank you for the constant encouragement, love and support. Thank you for always thinking of me and for making me smile.

Mary, thank you for leading the way. Thank you for being such a support to me and for all the advice and love you have given me. Everyone should have a sister as amazing as you.

Mom and Dad, thank you for all of your love and support. Thank you for giving me guidance, prayers and worthy examples. I would not be who I am today if it were not for you two. Thank you.

TABLE OF CONTENTS

LIST OF TABLES

LIST OF FIGURES

1 Introduction

1.1 Classical Novae

Classical novae are binary stellar systems made up of a white dwarf that accretes hydrogen rich material from a partner main sequence star. The slow rate of accretion onto the surface of the white dwarf results in the system reaching degenerate conditions in which the accreted material is no longer able to expand with increasing temperature. As this hydrogen rich material accumulates on the surface of the white dwarf the density increases and hydrogen burning begins, resulting in an increased surface temperature. Since the nuclear cross sections increase with increasing temperature and there is no expansion of the accreted material to quench the burning, a thermonuclear runaway occurs leading to an explosion [1]. Unlike type 1a supernovae, which are completely destroyed by the violence of the explosion, a classical nova explosion does not destroy the parent white dwarf, allowing for recurrence of the explosion. The period of recurrence is typically on the order of 10^4 - 10^5 years. Classical novae are responsible for a very small fraction of the existent Galactic dust and therefore they do not significantly affect the elemental abundances in the Galaxy. They are, however, thought to be a significant source of certain isotopes, including ^{17}O, ^{15}N and ^{13}C [2]. Chemical abundance information is obtained from the spectral lines of the ejected material from classical novae for many of the CNO elements (see Sec. 1.2). One very important isotope is ^{18}F which β-decays, producing 511 keV γ-radiation that is currently detectable by satellites and the β-decay is one of the energy sources that power the optical display.

Nuclear physics cross sections present crucial inputs to classical nova simulations. These models have been significantly improved in recent years and present specialized tools for identifying which specific reactions should be further investigated in the laboratory. By varying the current reaction rates within the experimental uncertainties in the nova model input, the effects on the final isotopic abun-

dances can be simulated. Despite investigation of hundreds of nuclear reactions in nova simulations, only a very small number of reactions significantly affect the final isotopic abundances of the ejected material [2]. Two of these reactions include ^{17}O(p,γ)^{18}F and the competing ^{17}O(p,α)^{14}N reaction. ^{17}O(p,γ)^{18}F creates ^{18}F, which is a major source of the detectable 511 keV γ-radiation in nova ejecta, while ^{17}O(p,α)^{14}N is the final step in the CNO II cycle (see section 1.2). The goal of this project is to enhance the current understanding of these two reaction rates by experimentally obtaining higher precision measurements of their cross sections. This will improve nuclear physics inputs for the modeling of classical novae and other stellar environments where the quality of nucleosynthesis results is highly dependent upon the use of accurate reaction rates [2].

1.2 The CNO Cycles

A stellar environment consisting only of hydrogen and helium will burn hydrogen for energy generation only through the pp chains. For second generation stars, like our sun, the hydrogen burning region may contain nontrivial amounts of carbon, nitrogen and oxygen. These higher mass nuclei aid in the burning of hydrogen in what are known as the CNO cycles. At stellar temperatures below 0.1 GK the CNO cycles consist of a total of four cycles known as the cold CNO cycles (Tab. 1.1). The first three cold CNO cycles are illustrated in Fig. 1.1. Each of the four cold CNO cycles yields, effectively, the same result as the pp chains; that is they convert four protons into one α-particle, two neutrinos and two positrons, or symbolically 4H $\longrightarrow$^{4}He + 2ν + 2e^{+} [1]. Carbon, nitrogen and oxygen function as catalysts and though their relative abundances may change from those at the formation of the star, the total number of higher mass nuclei remains constant throughout the cold CNO cycles. The relative abundances of these nuclei are highly sensitive to temperature because they depend on the reaction rates of the proton captures involved.

The existence of four cycles comes about because, of the eight stable nuclei in the process which can capture a proton, four of them have an open α-particle exit channel. The production of an α-particle returns each chain to the start; however, if the reaction involves the emission of a γ-ray a different cycle begins. Consider, for instance, hydrogen burning of ^{14}N. The cold CNO I cycle is completed with the ^{15}N(p,α)^{12}C reaction. If, instead, the reaction follows the ^{15}N(p,γ)^{16}O route, the

CNO I	CNO II	CNO III	CNO IV
^{12}C(p,γ)^{13}N	^{14}N(p,γ)^{15}O	^{15}N(p,γ)^{16}O	^{16}O(p,γ)^{17}F
↓	↓	↓	↓
^{13}N($\beta^+\nu$)^{13}C	^{15}O($\beta^+\nu$)^{15}N	^{16}O(p,γ)^{17}F	^{17}F($\beta^+\nu$)^{17}O
↓	↓	↓	↓
^{13}C(p,γ)^{14}N	^{15}N(p,γ)^{16}O	^{17}F($\beta^+\nu$)^{17}O	^{17}O(p,γ)^{18}F
↓	↓	↓	↓
^{14}N(p,γ)^{15}O	^{16}O(p,γ)^{17}F	^{17}O(p,γ)^{18}F	^{18}F($\beta^+\nu$)^{18}O
↓	↓	↓	↓
^{15}O($\beta^+\nu$)^{15}N	^{17}F($\beta^+\nu$)^{17}O	^{18}F($\beta^+\nu$)^{18}O	^{18}O(p,γ)^{19}F
↓	↓	↓	↓
^{15}N(p,α)^{12}C	^{17}O(p,α)^{14}N	^{18}O(p,α)^{15}N	^{19}F(p,α)^{16}O

Table 1.1: Cold CNO cycles I-IV: Each cycle converts four protons into one α, two neutrinos and two positrons. The two ^{17}O + p reactions are in red. Table concept was borrowed from [1].

CNO II cycle is entered. These two cycles operate simultaneously in the star and in about 1 out of 1000 operations of the cold CNO I cycle there will be a branch into the cold CNO II cycle.

There exists a branch point between the cold CNO II and CNO III cycles, involving the proton capture of ^{17}O. If the reaction proceeds through the ^{17}O(p,α)^{14}N path, then the cold CNO II cycle will continue. However, if the ^{17}O(p,γ)^{18}F reaction occurs, the cold CNO III cycle is entered and new nuclei, not reachable by the cold CNO I or CNO II cycle, can now be synthesized. The ratio of these two reaction rates is highly energy dependent and will determine the ^{17}O hydrogen burning pathway. A great deal of uncertainty exists in the current literature for the rates of these two reactions, particularly at the lowest stellar energies of T $<$ 10 MK where it is not even certain which rate is larger. The ultimate path followed by the cold CNO cycles will not be greatly affected by the branch point at ^{17}O + p, since the cold CNO II cycle is so rarely entered. Furthermore, over the stellar temperature range of interest, the ^{17}O(p,α)^{14}N reaction rate is two orders of magnitude greater than the rate of ^{17}O(p,γ)^{18}F. The final isotopic abundances of oxygen, however, may be greatly affected by the CNO II and CNO III branch point, providing a crucial constraint on the stellar modeling of sites where the CNO cycles are in operation.

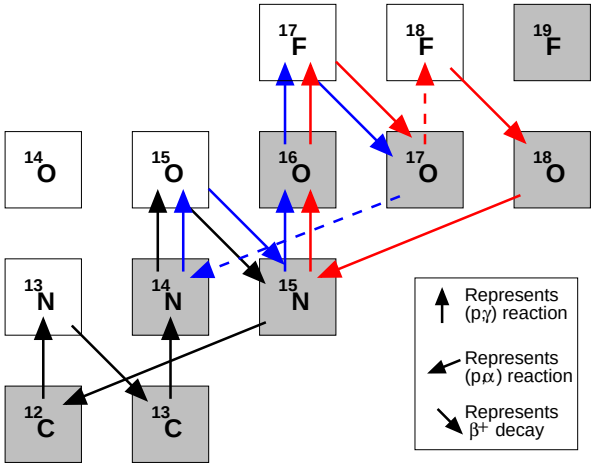

Figure 1.1: The cold CNO cycles I (black), II (blue) and III (red) with stable nuclei shaded. Dashed lines indicate the reaction branch at ^{17}O + p. The legend arrows representing the three nuclear reactions are not to scale.

1.2.1 The Hot CNO Cycles

Classical novae burn hydrogen explosively at very high temperatures (T = 0.1-0.4 GK). At these elevated temperatures the burning is described by the hot CNO cycles. These three cycles are illustrated in Fig. 1.2. While the first hot CNO cycle, HCNO I, is similar to the first cold CNO cycle, at high temperatures ^{13}N is more likely to capture a proton to form ^{14}O than to undergo β-decay to form ^{13}C. High nova temperatures also allow the reactions involved in this cycle to all occur much faster than the β-decays of ^{14}O and ^{15}O, resulting in accumulation of ^{14}O and ^{15}O, the most abundantly produced nuclides in the hot CNO cycles. The HCNO I cycle completes in $\approx$ 300 s, while the length of a typical nova explosion is a few hundred seconds. This means that novae are not operating in equilibrium [1].

The HCNO II and HCNO III cycles are critically important to the final isotopic abundances of oxygen, since these cycles determine what happens to the initial ^{16}O in the nova. There are several possible ways to break out of these two cycles and into higher mass burning regions [1]. These breakout possibilities are the reason that hundreds of reactions must be taken into account when simulating classical novae. In order to further investigate the critical ^{17}O(p,γ)^{18}F and ^{17}O(p,α)^{14}N reaction rates, it is helpful to be familiar with a few very important concepts in nuclear physics. The rest of this chapter is dedicated to presenting the fundamental concepts in the calculation of reaction rates.

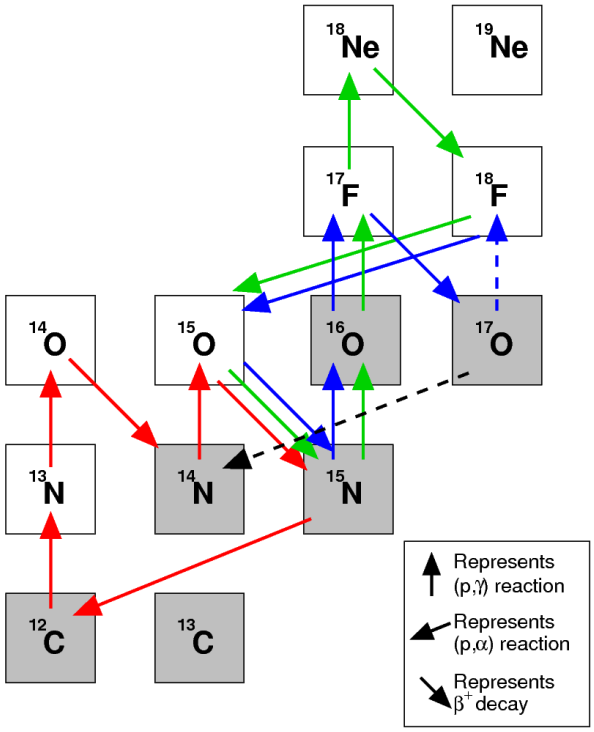

Figure 1.2: The hot CNO cycles I (red), II (blue) and III (green) with stable nuclei shaded. Dashed lines indicate the reaction branch at ^{17}O + p. The black line representing the ^{17}O(p,α)^{14}N is not a part of any of the three cycles. The legend arrows representing the three nuclear reactions are not to scale.

1.3 Reaction Rates and Cross Sections

A commonly used quantity in nuclear astrophysics is the reaction rate per particle pair, $< \sigma v >$, for a specific set of nuclei. Knowledge of the reaction rate is necessary for determining the direction of stellar nucleosynthesis and the resulting isotopic abundances of specific elements. The purpose of this section is to summarize, following the presentation of Ref. [1], the major concepts involved in the calculations of the reaction rate for a given pair of nuclei.

The reaction rate per particle pair for a thermonuclear environment is given by

$$< \sigma v >= \sqrt{\frac{8}{\pi\mu}} \frac{1}{(kT)^{3/2}} \int_0^\infty E\sigma(E) e^{-E/kT} dE, \tag{1.1}$$

where μ is the reduced mass of the projectile and target; k is Boltzmann's constant; T is the temperature; E is the relative energy between projectile and target and σ(E) is the cross section of the reaction of interest. The cross section describes the probability of the reaction occurring given the relative energy between the projectile and target. The factor $e^{-E/kT}$ originates from the Maxwell-Boltzmann distribution of relative particle energies in a thermonuclear environment. The form of the cross section may be different depending on the reaction specifics, but regardless of the description of the cross section one may always construct the astrophysical S-factor, which is defined by

$$\sigma(E) \equiv \frac{1}{E} e^{-2\pi\eta} S(E), \tag{1.2}$$

where $\eta \equiv \sqrt{\frac{\mu}{2E}} Z_p Z_t \frac{e^2}{\hbar}$ is the Sommerfeld parameter and Z_p, Z_t are the charge of the projectile and target nucleus, respectively. The known major energy dependencies of the cross section have been separated out, leaving only the S-factor. The $\frac{1}{E}$ term describes a semi-classical cross section [3], and the $e^{-2\pi\eta}$ term, called the Gamow factor, describes the s-wave transmission through the Coulomb barrier at very low bombarding energies [1]. The remaining S-factor is significantly less energy dependent than the cross section and contains all of the nuclear physics. It will be a much smoother varying curve than the cross section and thus more easily extrapolated to energies of stellar importance from energies where experimental measurements can be made. Combining Eqs. 1.1 and

1.2 gives the following form for the thermonuclear reaction rate per particle pair:

$$< \sigma v >= \sqrt{\frac{8}{\pi\mu}} \frac{1}{(kT)^{3/2}} \int_0^\infty e^{-2\pi\eta} S(E) e^{-E/kT} dE. \tag{1.3}$$

1.3.1 Nonresonant Cross Sections

Since the major energy dependence of the cross section has been removed to define the S-factor, it is often the case that S(E) may be assumed to be constant, significantly simplifying the integral in Eq. 1.3 and the resultant form of the reaction rate. If S(E) is approximated as a constant, S_0, the form of the reaction rate becomes

$$< \sigma v >= \sqrt{\frac{8}{\pi\mu}} \frac{1}{(kT)^{3/2}} S_0 \int_0^\infty e^{-2\pi\eta} e^{-E/kT} dE. \tag{1.4}$$

The integrand now consists of two energy dependent terms which are illustrated in Fig. 1.3. The Maxwell Boltzmann factor, which is $\propto e^{-E/kT}$, describes the energy distribution of the particles in a thermonuclear environment and the Gamow factor, $e^{-2\pi\eta}$, is proportional to the probability of tunneling through the Coulomb barrier. The product of these two terms forms a peak, known as the Gamow peak, which describes the effective energy region where the thermonuclear reactions occur. The effective energy region is shifted to a higher energy than the average thermal energy of the particles, since the probability of interaction is vanishingly small where the energy distribution of the particles peaks. The result of the interplay between the increasing cross section at very high energies and the very low thermonuclear energies of most of the particles is that the bulk of the nuclear reactions will occur where the Gamow peak is a maximum.

Approximating the Gamow peak with a Gaussian allows for a position and width of the Gamow peak to be defined, which results in an effective analytical tool for describing the energy burning region of nonresonant thermonuclear reactions. This is derived by constructing a Gaussian curve which has the same amplitude and curvature at the maximum as the Gamow peak. That is

$$\exp\left[-\frac{E}{kT} - \frac{b}{\sqrt{E}}\right] = I_{max} \exp\left[\frac{-(E-E_0)^2}{\left(\frac{\Delta}{2}\right)^2}\right] \tag{1.5}$$

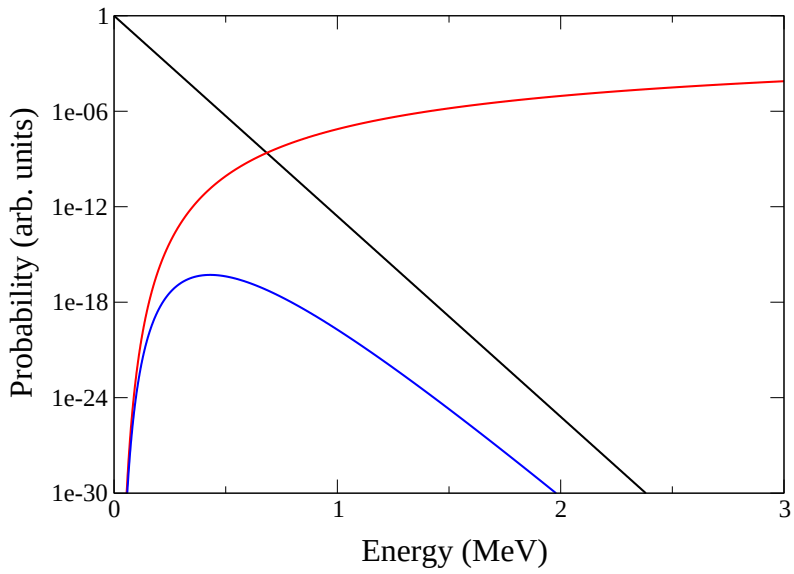

Figure 1.3: The Gamow factor (red curve), the Maxwell-Boltzmann factor (black curve) and the resultant Gamow peak (blue curve) for the reaction ^{17}O + p at a stellar temperature of 0.4 GK

where $b \equiv \frac{\sqrt{2\mu}\pi e^2 Z_1 Z_2}{\hbar}$ and I_{max} is the amplitude of the Gaussian which is to be matched with the amplitude of the Gamow peak. The position of the maximum and the $1/e$ width of the Gaussian are given by E_0 and Δ, respectively. To find E_0 it is necessary to set the first derivative of the Gamow peak to zero and solve for the energy [1]

$$\begin{aligned} \frac{d}{dE}\left[\exp\left(-\frac{E}{kT}-\frac{b}{\sqrt{E}}\right)\right]_{E=E_0} &= 0 \\ \left[\left(-\frac{1}{kT}+\frac{b}{2E^{\frac{3}{2}}}\right)\exp\left(-\frac{E}{kT}-\frac{b}{\sqrt{E}}\right)\right]_{E=E_0} &= 0. \end{aligned} \tag{1.6}$$

This gives

$$\begin{aligned} \frac{1}{kT} &= \frac{b}{2E_0^{\frac{3}{2}}} \\ E_0 &= \left(\frac{bkT}{2}\right)^{\frac{2}{3}}. \end{aligned} \tag{1.7}$$

Solving for the width of the Gaussian requires matching the second derivatives of the two peaks at the maximum, E_0. This gives

$$\frac{d^2}{dE^2}\left[\exp\left(-\frac{E}{kT}-\frac{b}{\sqrt{E}}\right)\right]_{E=E_0}=\frac{d^2}{dE^2}\left(I_{max}\exp\left[-\frac{(E-E_0)^2}{\left(\frac{\Delta}{2}\right)^2}\right]\right)_{E=E_0}. \tag{1.8}$$

Now consider the following:

$$\frac{d^2}{dE^2}\left[e^{f(E)}\right]=\frac{d}{dE}\left[f'(E)e^{f(E)}\right]=f''(E)e^{f(E)}+f'(E)f'(E)e^{f(E)}. \tag{1.9}$$

Since the second derivative is to be evaluated at E = E_0 for both functions and E_0 is defined as the maximum of both curves, the first derivative of each function evaluated at E = E_0 will be 0. That is

$$\frac{d}{dE}e^{f(E)}\Big|_{E=E_0}=f'(E)e^{f(E)}\Big|_{E=E_0}=0. \tag{1.10}$$

This means that $f'(E)f'(E)e^{f(E)}\big|_{E=E_0}=0$ for both the constructed Gaussian and the Gamow peak functions. This simplifies the calculations for both the Gamow peak

$$\begin{aligned}&\frac{d^2}{dE^2}\left[\exp\left(-\frac{E}{kT}-\frac{b}{\sqrt{E}}\right)\right]_{E=E_0}\\&=\frac{d}{dE}\left(-\frac{1}{kT}\frac{b}{2E^{\frac{3}{2}}}\right)\exp\left(\frac{-E}{kT}-\frac{b}{\sqrt{E}}\right)_{E=E_0}\\&=\frac{-3b}{4E_0^{\frac{5}{2}}}\exp\left(\frac{-E_0}{kT}-\frac{b}{\sqrt{E_0}}\right)\end{aligned} \tag{1.11}$$

and the Gaussian approximation

$$\begin{aligned}&\frac{d^2}{dE^2}\left(I_{max}\exp\left[-\frac{(E-E_0)^2}{\left(\frac{\Delta}{2}\right)^2}\right]\right)_{E=E_0}\\&=\left(\frac{d}{dE}\left[\frac{2(E-E_0)}{\left(\frac{\Delta}{2}\right)^2}\right]\times I_{max}\exp\left[\frac{-(E-E_0)^2}{\left(\frac{\Delta}{2}\right)^2}\right]\right)_{E=E_0}\\&=\frac{-8}{\Delta^2}I_{max}.\end{aligned} \tag{1.12}$$

Combining Eqs. 1.8, 1.11 and 1.12 and gives

$$\begin{aligned} \frac{-3b}{4E_0^{\frac{5}{2}}} \exp\left(\frac{-E_0}{kT} - \frac{b}{\sqrt{E_0}}\right) &= \frac{-8}{\Delta^2} I_{max}; \\ \frac{-3}{4kTE_0} &= \frac{-8}{\Delta^2}; \\ \Delta &= \frac{4}{\sqrt{3}}\sqrt{kTE_0}, \end{aligned} \tag{1.13}$$

where $b = \frac{2E_0^{\frac{3}{2}}}{kT}$ is substituted, as derived from Eq. 1.7, and $I_{max} = \exp\left(\frac{-E_0}{kT} - \frac{b}{\sqrt{E_0}}\right)$ since the height and position of the two peaks have been matched. Using Eqs. 1.7 and 1.13, E_0 and Δ may now be found numerically, in units of MeV [1]:

$$E_0 = 0.1220 \left[\frac{m_p m_t}{m_p + m_t} \left(Z_p Z_t T_9\right)^2\right]^{\frac{1}{3}} \tag{1.14}$$

and

$$\Delta = 0.2368 \left(\frac{m_p m_t}{m_p + m_t} \left(Z_p Z_t\right)^2 T_9^5\right)^{\frac{1}{6}}. \tag{1.15}$$

The temperature in units of GK is denoted by T_9. The range $E_0 \pm \frac{1}{2}\Delta$ describes the energy region in which the majority of non-resonant nuclear reactions will occur. This range can be used to determine the most important energy regions to explore experimentally. It will not always be appropriate to approximate the S-factor as a constant, but for nonresonant reactions the cross section will always be slowly varying and can therefore be expanded in a Taylor series [1, 3].

1.3.2 Narrow Resonance Cross Sections

Another simplification of the thermonuclear reaction rate formula results if the thermonuclear reactions of interest proceed through narrow resonances. A resonance is considered narrow if the partial widths, Γ_i, can be considered constant across the width of the resonance and approximated by their values at E = E_r [1]. Partial widths and their effect on the reaction rate will be discussed in more detail in Chap. 2. In the case of a narrow resonance, the cross section can be described by the

Breit-Wigner formula, giving

$$\sigma(E) = \frac{\lambda^2}{4\pi}\frac{(2J+1)(1+\delta_{tp})}{(2j_t+1)(2j_p+1)}\frac{\Gamma_a\Gamma_b}{(E_r-E)^2+\Gamma^2/4}, \tag{1.16}$$

where λ is the de Broglie wavelength; Γ_a and Γ_b are the partial widths of the resonance entrance and exit channels, respectively and Γ is the total width of the resonance. These are all in the center of mass frame. The spins of the projectile, target and resonance are given by j_p, j_t and J, respectively. The energy of the resonance, in the center of mass system, is given by E_r. Combining Eqs. 1.16 and 1.1 and the relation $\lambda^2 = \frac{(2\pi\hbar)^2}{2\mu E}$ gives, for the narrow resonant reaction rate,

$$< \sigma v >= \frac{\sqrt{2\pi}\hbar^2}{(\mu kT)^{\frac{3}{2}}}\int_0^\infty \omega\frac{\Gamma_a\Gamma_b}{(E_r-E)^2+\Gamma^2/4}e^{-\frac{E}{kT}}dE, \tag{1.17}$$

where $\omega \equiv \frac{(2J+1)(1+\delta_{pt})}{(2j_p+1)(2j_t+1)}$. Since this is a narrow resonance, symmetric around E = E_r, it will not change the result of the above integration to integrate from a lower limit of $-\infty$ rather than from 0. Using the following identity:

$$\int_{-\infty}^{\infty}\frac{a}{(E_r-E)^2+a^2}dE = \pi, \tag{1.18}$$

the contribution to the reaction rate from a single narrow resonance is simplified to the following:

$$< \sigma v >= \left(\frac{2\pi}{\mu kT}\right)^{\frac{3}{2}}\hbar^2\omega\gamma e^{-\frac{E_r}{kT}}, \tag{1.19}$$

where $\gamma \equiv \frac{\Gamma_a\Gamma_b}{\Gamma}$. The product of ω and γ is known as the resonance strength. Since a narrow resonance is an isolated peak in the cross section, the contribution to the total reaction rate from a single narrow resonance will be unaffected by the existence of other narrow resonances. Thus, in an environment where the cross section is dominated by several narrow resonances, the integral will effectively identify each resonance separately and the total narrow resonant contribution to the reaction rate will be an incoherent sum over these individual resonances, resulting in

$$< \sigma v >_{nr}= \left(\frac{2\pi}{\mu kT}\right)^{\frac{3}{2}}\hbar^2\sum_i(\omega\gamma)_i e^{-\frac{E_i}{kT}}. \tag{1.20}$$

At certain temperatures, this narrow resonant contribution will dominate the total reaction rate and all that is necessary for a simple calculation of the the total reaction rate is a list of the resonance energies and their associated strengths, $\omega\gamma$.

It is interesting to note the exponential term in the narrow resonant reaction rate formula. It is clear that lower energy resonances will be favored. However, these resonances are typically weak, since the incident particle must tunnel through the Coulomb barrier and this tunneling probability drops exponentially with decreasing energy (see Eq. 1.4). This creates an interplay between the Coulomb barrier and the exponential, which favor higher and lower energy resonances, respectively. This will be discussed in depth in Chap. 2. As a result of the very small resonance strengths, the low energy resonances are often extremely difficult, if not impossible, to measure with current technology. At certain temperatures, the contribution to the total reaction rate may be completely dominated by one or two of these low-energy resonances and it is often the case that the largest contribution to the total uncertainty for a given reaction rate in a given temperature range comes from an unmeasured or very uncertain low energy resonance strength.

1.3.3 Broad Resonance Cross Sections

Often when calculating reaction rates, the energy dependence of the partial widths must be included explicitly. If this is the case, the narrow resonance formalism presented in Sec. 1.3.2 is not sufficient to properly calculate the contribution of this resonance to the reaction rate. If the energy dependence of a resonance becomes important, it is necessary to integrate the cross section of that resonance to determine its contribution to the reaction rate. The cross section for a broad resonance can be described by the one-level Breit-Wigner formula [1]

$$\sigma_{BW}(E) = \frac{\pi\hbar^2\omega}{2\mu E}\frac{\Gamma_a(E)\Gamma_b(E+Q-E_f)}{(E_r-E)^2+\frac{1}{4}\Gamma(E)^2}, \tag{1.21}$$

which is the same as Eq. 1.16 with the energy dependence of the partial widths indicated. The energy dependence of the particle partial width may be approximated as $\Gamma_i(E) \approx P_i(E)$, where P(E), the penetration factor, represents the transmission probability of s-wave particles through the Coulomb and centripetal barriers of the nucleus and should be numerically calculated. The γ-ray partial width

is approximated as $\Gamma_\gamma \approx E_\gamma^{2L+1}$, where E_γ is the energy and L is the multipolarity of the emitted γ-ray. Substituting these approximations for the partial widths into Eq. 1.21 gives [1]

$$\sigma_{BW}(E) = \frac{\pi\hbar^2\omega}{2\mu E}\frac{\frac{P_a(E)}{P_a(E_r)}\Gamma_a(E_r)\frac{P_b(E+Q-E_f)}{P_b(E_r+Q-E_f)}\Gamma_b(E+Q-E_f)}{(E_r-E)^2+\frac{1}{4}\Gamma(E)^2}, \tag{1.22}$$

for reactions involving particle emission. For reactions involving photon emission, like ^{17}O(p,γ)^{18}F, the cross section becomes:

$$\sigma_{BW}(E) = \frac{\pi\hbar^2\omega}{2\mu E}\frac{\frac{P_a(E)}{P_a(E_r)}\Gamma_a(E_r)\left[\frac{(E+Q-E_f)}{(E_r+Q-E_f)}\right]^{2L+1}\Gamma_\gamma(E+Q-E_f)}{(E_r-E)^2+\frac{1}{4}\Gamma(E)^2}. \tag{1.23}$$

The cross section can then be integrated to determine the single resonance contribution to the reaction rate. This is given by [1]

$$<\sigma v> = \sqrt{2\pi}\frac{\omega\hbar^2}{(\mu kT)^{\frac{3}{2}}}\int_0^\infty \exp\left(\frac{-E}{kT}\right)\frac{\Gamma_a(E)\Gamma_b(E+Q-E_f)}{(E_r-E)^2+\frac{1}{4}\Gamma(E)^2}dE. \tag{1.24}$$

With Eq. 1.24 it is now possible to numerically integrate the reaction rate contribution for a resonance which has significant energy dependence in the cross section. Explicit integration of the cross section to calculate the reaction rate is always a valid procedure but is not always necessary, as in the case of a narrow resonance. Comparing the integrated cross section with the result of the narrow resonant form of the reaction rate contribution for a specific resonance allows one to determine whether the narrow resonance approximation is valid near a specific temperature, or whether it is necessary to numerically integrate.

In the case of subthreshold resonances ($E_r^{cm} < 0$), the calculation of the proton partial width requires the spectroscopic factor, C^2S, and the single particle reduced width, θ_{sp}^2 [4]. The procedure for calculating θ_{sp}^2 can be found in Ref. [4]. The spectroscopic factor is an experimentally measured quantity that can often be found in the literature and is discussed in detail in App. A.1. These quantities are combined to yield the particle partial width:

$$\Gamma_p(E) = \frac{2\hbar^2}{\mu R^2}P(E)C^2S\theta_{sp}^2. \tag{1.25}$$

The penetration factor, P(E), gives the major energy dependence of the partial width. This form of the partial width can be used to find the contribution to the reaction rate arising from the tail of a subthreshold resonance.

1.4 The Direct Capture Process

Direct capture is a process by which a proton is captured by a nucleus to form a bound state of a final nucleus without the formation of a compound nucleus. This occurs along with the emission of a γ-ray. The interaction of the proton with the electromagnetic field allows for the transition of the proton from an initial scattering state to a final bound state. Since the electromagnetic interaction is well known, the direct capture cross section can be calculated analytically. However, a suitable nuclear potential must be used to describe the initial scattering and final bound state wave functions. The dominant contribution to the direct capture cross section comes from the E1 transition of a scattering state with initial angular momentum, ℓ_i, to a bound state of final angular momentum, ℓ_f. The following describes this cross section [5, 6]:

$$\begin{aligned}\sigma_{calc}(E1) &= 0.0716\mu^{\frac{3}{2}}\left(\frac{Z_p}{A_p}-\frac{Z_t}{A_t}\right)^2\frac{E_\gamma^3}{E^{\frac{3}{2}}} \\ &\quad\times\frac{(2J_f+1)\,(2\ell_i+1)}{(2j_p+1)\,(2j_t+1)\,(2\ell_f+1)}\,(\ell_i 010|\ell_f 0)^2\,R^2_{n\ell_i 1\ell_f},\end{aligned} \tag{1.26}$$

where Z_p, Z_t, A_p and A_t are the charges and masses of the projectile and target respectively; J_f, j_p and j_t are the spins of the final state, projectile and target respectively; E is the bombarding energy and E_γ is the energy of the γ-ray transition; $R_{n\ell_i 1\ell_f}$ is known as the radial integral and is defined as

$$R_{n\ell_i 1\ell_f} = \int_0^\infty u_c(r) O_{E1} u_b(r) r^2 dr. \tag{1.27}$$

O_{E1} is the radial part of the E1 multipole operator and u_c, u_b are the initial scattering and final bound state radial wave functions, respectively [5, 6].

The major energy dependence of the direct capture cross section comes from the radial integral, $R_{n\ell_i 1\ell_f}$, as a result of the energy sensitivity of the radial wave functions of the initial scattered and

final bound states. The choice of the scattering and bound state potentials used to describe the nuclear potential is very important and must be treated carefully. First, it is important to understand the procedure for determining the initial and final orbital angular momenta, ℓ_i and ℓ_f. Given J_f, j_p and j_t, it is possible to solve for both, which are necessary for the calculation of the radial integral. The reaction ^{17}O(p,γ)^{18}F will be used as an example for this calculation and the angular momentum coupling will be described as follows:

$$^{17}O + p + \ell_i \longrightarrow {}^{18}F + E1; \tag{1.28}$$

$$^{17}O + p + \ell_f \longrightarrow {}^{18}F. \tag{1.29}$$

Consider, specifically, the capture of a proton by ^{17}O to form a 1^+ state in ^{18}F; ^{17}O and p have angular momenta of $\frac{5}{2}^+$ and $\frac{1}{2}^+$, respectively, and can therefore couple to a total momentum of 2^+ or 3^+. Similarly, ^{18}F and E1 have angular momenta of 1^+ and 1^- respectively and can couple to 0^-, 1^-, or 2^-. Since the final parity is proportional to $(-1)^\ell$, then ℓ_i must be odd. This allows for an initial angular momentum of 1, 3 or 5. Usually, only the first two ℓ values are kept since higher contributions are negligible.

Similarly, Eq. 1.29 may be solved for ℓ_f. Again, ^{17}O and p will couple to form momenta of 2^+ or 3^+. To form the final angular momentum of 1^+, ℓ_f must be even, allowing for $\ell_f = 2$ or 4, resulting in combinations of $\ell_i = 1, 3$ and $\ell_f = 2, 4$. These values are needed as inputs for calculation of the initial scattering and final bound state wave functions of the direct capture of a proton on ^{17}O to form a 1^+ state of ^{18}F.

1.4.1 The Bound State Wave Function

Though the direct capture mechanism occurs through interaction with the electromagnetic field, the nuclear potential will determine the form of the initial scattering state and final bound state wave functions of the captured proton. In the past, the two most popular choices for the bound state potential have been the square well and the Woods-Saxon potentials [5]. It will be shown later in this section that the radial position at which direct capture occurs is actually outside of the nuclear radius. At first glance this might suggest that it does not matter what choice of bound state potential is used to

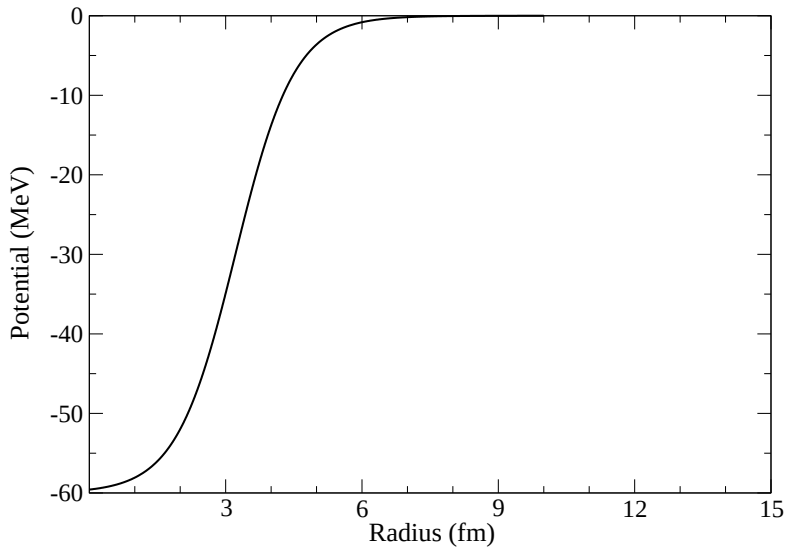

Figure 1.4: A Woods-Saxon potential for ^{17}O with $r_0 = 1.25$ fm, $a = 0.65$ fm and $V_0 = -60$ MeV.

describe the nucleus, as long as the chosen depth, V_0, reproduces the binding energy of the final state. Figure 7 from Ref. [7], however, illustrates the fact that the choice of bound state potential can in fact have a significant effect on the final S-factor and should be chosen carefully. For this reason, a Woods-Saxon potential will be used for the bound state potential, as it is a more realistic description of the nuclear potential than a square well. The Woods-Saxon potential is defined by

$$V_{WS}(r) = \frac{-V_0}{1 + \exp\left(\frac{r-R}{a}\right)}, \tag{1.30}$$

where $R = r_0 A_t^{\frac{1}{3}}$, with $r_0 = 1.25$ fm and $a = 0.65$ fm. These are typical values used for the Woods-Saxon potential, taken from Ref. [5] and illustrated in Fig. 1.4.

The full potential for calculating the bound state wave function is a combination of a Woods-Saxon potential with the Coulomb potential of a uniformly charged sphere. The code used to calculate the bound state wave function resulting from this choice of potential is the same code used in Refs. [5, 7]. The radial wave function for the direct capture of a proton by ^{17}O via the $E_x = 4360$ keV state in ^{18}F is shown in Fig. 1.5. The bound state wave function illustrated in Fig. 1.5 peaks outside the

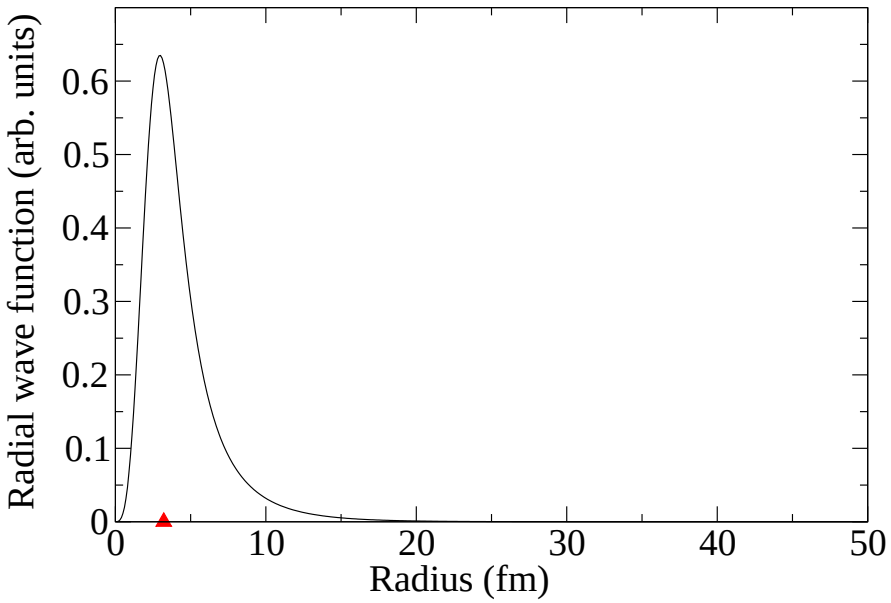

Figure 1.5: Bound state wave function for direct capture to the $E_x = 4360$ keV $J^\pi = 1^+$ and $\ell_f = 2$ state in ^{18}F. The red triangle marks the nuclear radius of the Woods-Saxon potential at 3.2 fm.

nuclear radius of 3.2 fm, meaning that the contribution to the radial integral from the bound state wave function will be primarily outside the nuclear surface. States that are less bound in the final nucleus will extend further outside the nuclear radius, so direct capture to less bound states will result in a contribution to the cross section which is peaked further outside the nuclear radius.

1.4.2 The Scattered State Wave Function

The scattered state wave function is the second component of the radial integrand that requires careful consideration. The choice of scattering potential is not trivial. It may seem obvious to simply use the same potential for the scattered state as was used for the bound state, but this may lead to problems since the choice of either a Woods-Saxon or square well for the scattering potential will inherently lead to resonances in the cross section as the depth of the potential is varied, making each an obviously improper choice of potential for describing direct capture which is a nonresonant interaction [5]. Therefore a new potential must be chosen for the scattered state that does not give rise to resonances. The hard sphere is a simple potential arising from scattering theory and will be used as the scattering potential for the calculation of the scattering state wave function, radial integral,

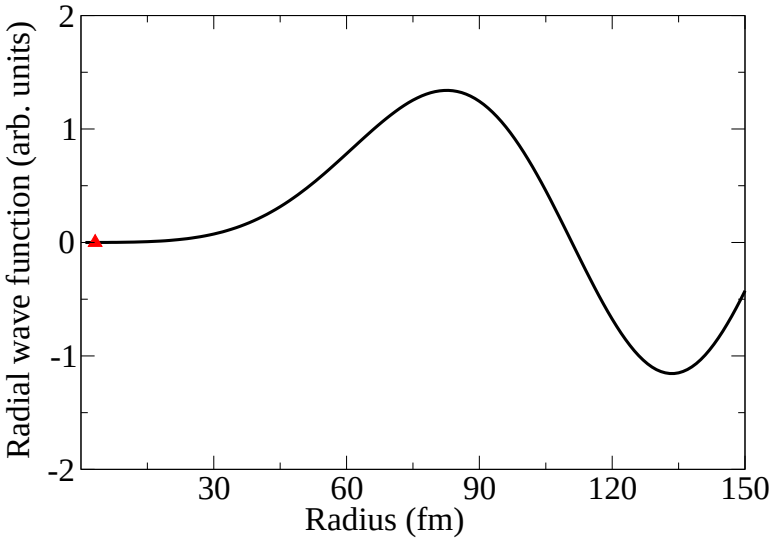

Figure 1.6: Scattered state wave function for an incoming proton with center of mass energy of E_{cm} = 200 keV and orbital angular momentum ℓ_i = 1 incident on a hard sphere of radius, R = 3.2 fm (denoted by the red triangle).

and finally the direct capture cross section. A radius of $R = 1.25A_i^{\frac{1}{3}} = 3.2$ fm for the hard sphere will be chosen to match the nuclear radius of the bound state potential [5]. It is clear from Fig. 1.6 that the scattered state wave function oscillates and the first maximum is very far outside the nuclear radius. This, along with the fact that the bound state wave function also peaks outside the nuclear radius, results in a negligible contribution to the cross section from the scattered state near the nuclear radius. This means that the specific choice of the scattering potential is not very important, as long as it is not a potential that gives rise to unphysical resonances. The less bound the final state, the less important the choice of scattering potential will be, making the simple choice of the hard sphere perfectly acceptable for the current application. Now that the bound state and scattered state wave functions have been constructed it is possible to calculate the radial integral.

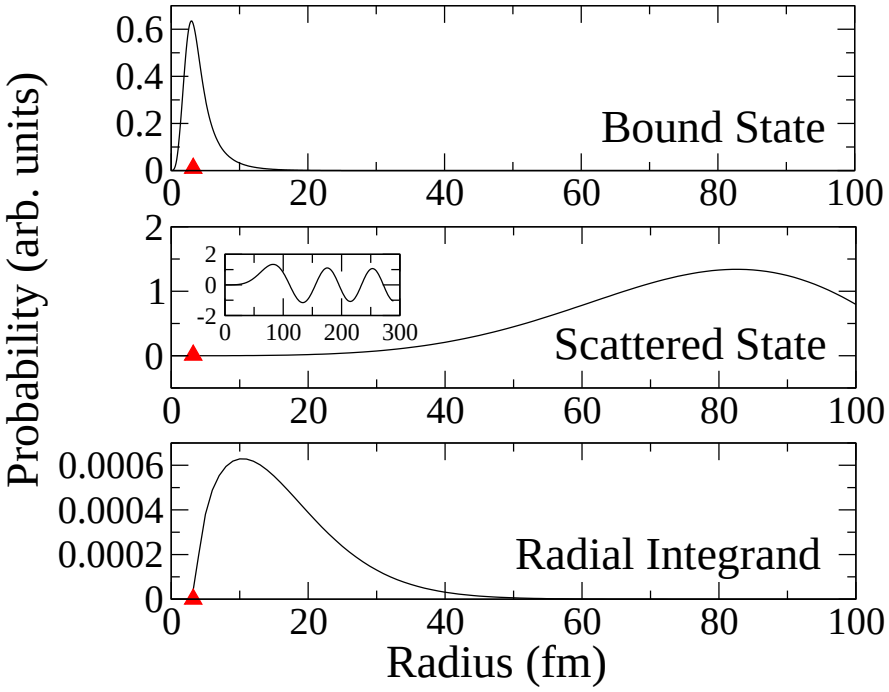

Figure 1.7: Integrand of radial integral (bottom panel) calculated for the capture of a 200 keV proton with ℓ_i = 1 into the E_x = 4360 keV state in ^{18}F. For comparison, the corresponding bound state (top panel) and scattered state (middle panel) wave functions have been included. The red triangle denotes the nuclear radius of 3.2 fm.

1.4.3 The Radial Integral and Direct Capture Cross Section

Using the bound and scattered state wave functions calculated in Sec. 1.4.1 and 1.4.2, the integrand of the radial integral may be constructed. The radial integrand describes where, in radius, the direct capture actually occurs and is shown along with the bound and scattered state wave functions in Fig. 1.7. It is clear that the proton is captured outside the nuclear radius and, for this reason, the process of direct capture has also been called "extranuclear capture" [6].

For a given level in the final nucleus and a given bombarding energy, the calculation of the contribution to the cross section for capture into that state will require summing over the contributions from all possible ℓ_i and ℓ_f combinations. Also, the experimentally measured cross section will differ from the calculated cross section by a factor called the spectroscopic factor, $C^2S(\ell_f)$, which is discussed in detail in App. A.1. The spectroscopic factors are often experimentally measured and can be found

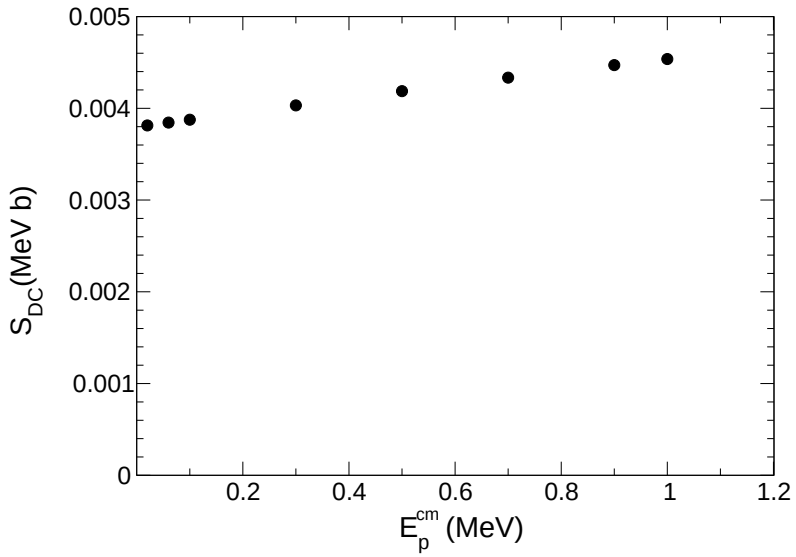

Figure 1.8: Expected experimental S-factor for the direct capture component of ^{17}O(p,γ)^{18}F. These are calculated using the same spectroscopic factors as Ref. [7]

in the literature. The experimental cross section will be found by [5, 6]

$$\sigma_{exp} = \sum_{\ell_i,\ell_f} C^2 S(\ell_f) \sigma_{calc}. \tag{1.31}$$

The total direct capture cross section for a given energy will then come from the sum of the contribution of each level in the final nucleus. Calculations will then be performed for a range of bombarding energies, resulting in an expected experimental cross section curve. From the cross section, the astrophysical S-factor is easily calculated using Eq. 1.2. Figure 1.8 represents the expected experimental S-factor for the ^{17}O(p,γ)^{18}F reaction. Chapter 4 will be entirely dedicated to the measurement of this direct capture curve below E_p^{cm} = 500 keV.

1.5 Thermonuclear Reaction Rate Calculations

A novel method has been developed using Monte Carlo techniques for evaluating thermonuclear reaction rates. Longland et al. [8] argue that current literature reaction rates, generally provided as a

recommended rate along with a minimum and maximum rate, have no statistical meaning owing to the lack of an associated probability distribution. The new Monte Carlo method calculates reaction rates and uncertainties using appropriate probability density functions for each input parameter. While resonance energies are Gaussian distributed, resonance strengths, cross sections and partial widths constitute a product of positive quantities including: measured yields, stopping powers, integrated charge, etc. According to the central limit theorem, such a product of quantities will be described by a lognormal probability density function, which can be written as [8]

$$f(x) = \frac{1}{\sqrt{2\pi}} \frac{1}{\sigma x} exp\left(\frac{-\left(ln(x) - \mu\right)^2}{2\sigma^2} \right), \tag{1.32}$$

where μ and σ are the mean and standard deviation of the Gaussian distribution of ln(x). Literature upper limit values of spectroscopic factors are properly described by Porter-Thomas density functions and this is described in detail in App. A.1. Interference between resonances is also taken into account in the rate calculations and a binary distribution is used when the sign of the interference is unknown (see Sec. 5.1.4).

Each input parameter is sampled according to its respective probability density function and the reaction rate is calculated. This procedure is repeated many times ($\approx$ 5000) by a Monte Carlo code written by Richard Longland, called **RatesMC**. The sampled rate distribution is calculated at each desired temperature and the low, median and high rates, corresponding to the 16, 50 and 84 percentiles of the cumulative distribution, are reported. The sampled rates are generally well described by a lognormal distribution and the associated μ and σ of this lognormal distribution are also presented. These parameters will allow for reconstruction of the sampled rate distribution. The sampling procedure and code operation are described in detail in Ref. [8]. The sampled Monte Carlo rates are matched to statistical model rates at high temperatures using a new procedure which is described in detail in Sec. 2.6.

2 The Effective Thermonuclear Energy Region

2.1 Exploration of the Gamow Peak in Narrow Resonance Realms

As discussed in Chap. 1, the calculation of the total reaction rate, for specific reactions, can be vastly simplified if the reactions proceed through narrow, isolated resonances. If this is the case, one can perform an incoherent sum over the contribution of each known resonance, where the only necessary inputs for the reaction rate calculation are the energy and corresponding strength of each resonance. An interesting question arises: since the reaction rates are calculated by summing over the contributions of each resonance to the total reaction rate, which resonances are the most important to the specific reaction rate of interest? The resonances of importance will differ from one stellar environment to another, since the stellar temperatures are different and the contribution from a single narrow resonance to the total reaction rate is a function of temperature. It would be extremely inefficient to measure each resonance, considering the time and resources necessary for this task and the fact that, often, only a few of the known resonances contribute significantly to the total reaction rate at a given temperature. This makes it crucial to find a procedure for determining which resonances, for a specific reaction and temperature, will make up the dominant contribution to the total reaction rate of interest.

The Gamow Peak was introduced in Chap. 1 as such a tool. Though the Gamow peak concept is strictly defined for nonresonant reactions, it may still be useful when considering reactions that proceed through narrow, isolated resonances. Recall that the Gamow peak arose after separating out the major energy dependencies of the cross section for a thermonuclear reaction to define the astrophysical S-factor. According to Eq. 1.3, the reaction rate involves an integral over the product of the Gamow Peak and the astrophysical S-factor. Since a narrow resonance is simply a spike in the S-factor and the product of the Gamow peak and the S-factor make up the integrand of the reaction

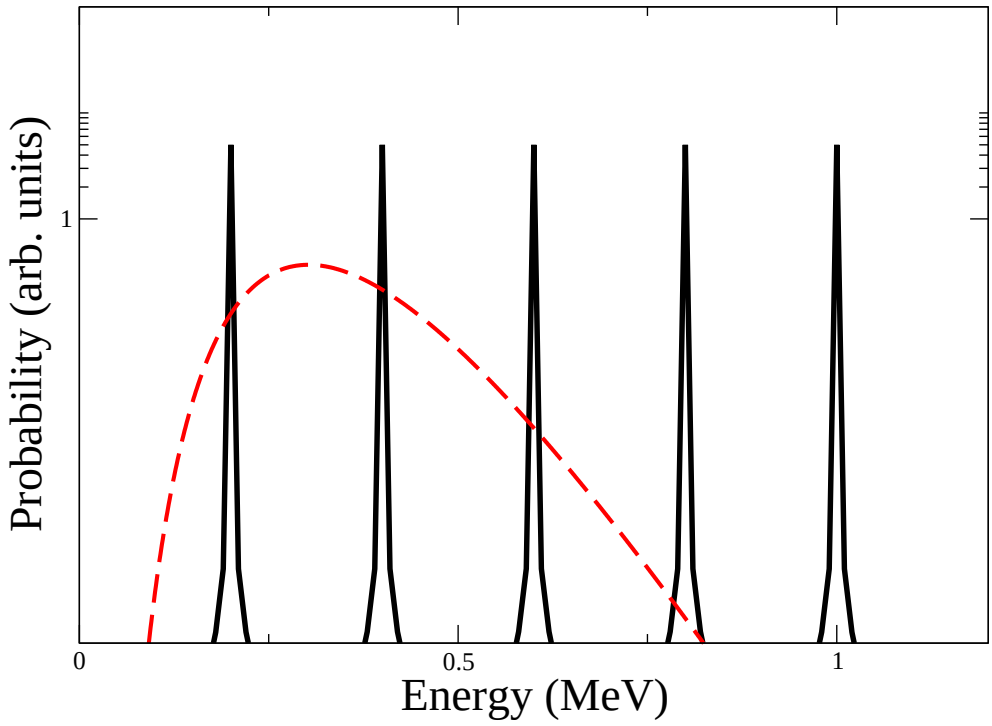

Figure 2.1: Schematic narrow resonances (black lines) overlaid by a sample Gamow peak (red dashed line).

rate contribution for a given resonance, one might expect the Gamow peak to simply select out the resonances which are most important to the reaction rate calculation. This argument hinges on the previous assumption that the nonresonant contribution to the S-factor is essentially constant compared to the energy dependence of the rest of the cross section and that the Gamow peak will span a region of resonances whose individual contributions to the total reaction rate will make the contributions from nonresonant processes comparatively insignificant.

Figure 2.1 illustrates the role which the Gamow peak plays in selecting the most important resonances with a simplified version of an S-factor consisting of five narrow resonances and a typical Gamow peak. Those resonances, which lie within the Gamow peak, should comprise the main contribution to the total reaction rate. The concept of the Gamow peak has been widely used in the

literature as a method for determining the most significant resonances for a specific reaction rate calculation [9]. The basis for this can be explained using an example of a (p,γ) reaction. Equation 1.20 describes the contribution to the reaction rate from a single narrow resonance as proportional to the resonance strength, $\omega\gamma$, where the resonance strength was defined as:

$$\omega\gamma = \omega\frac{\Gamma_a\Gamma_\gamma}{\Gamma_a + \Gamma_\gamma}. \tag{2.1}$$

As a result of the Coulomb barrier, the particle partial width, Γ_a, can vary by many orders of magnitude. At low energies, Γ_a may be insignificant compared to the γ-ray partial width, Γ_γ, which is far less energy dependent and usually on the order of meV - eV. In the case where $\Gamma_a \ll \Gamma_\gamma$ the total width, Γ, is dominated by the γ-ray partial width. This results in: $\omega\gamma \propto \Gamma_a$. The major energy dependence of the particle partial width will come from the penetration factor (see Eq. 1.25) which is proportional to the Gamow factor, $e^{-2\pi\eta}$. Note that the Gamow factor does not contain the entire energy dependence of Γ_a, but it does contain the major part of the energy dependence. At energies well below the Coulomb barrier, the particle partial width is not significantly affected by the value of the orbital angular momentum which means, for the relative contribution of a specific narrow resonance, the reaction rate becomes

$$< \sigma v >_i \propto e^{-2\pi\eta - \frac{E}{kT}}. \tag{2.2}$$

Recall from Eq. 1.4 that the right hand side is the Gamow peak. This suggests that the Gamow peak offers a useful tool for identifying the narrow resonances that contribute significantly to the total reaction rate at these stellar temperatures. Furthermore, the Gamow peak, which is a well-behaved function of temperature, is widely accepted in the literature and provides a straightforward description of the resonances of significance.

To test the validity of the Gamow peak for describing the true energy range of thermonuclear burning, the fractional contributions to the total reaction rate for each individual resonance must be calculated. For a given reaction and temperature, a plot is made of the fractional contributions to the total reaction rate, $\frac{<\sigma\nu>_i}{<\sigma\nu>_{total}}$, versus resonance energy for each individual resonance. The Gamow peak, defined for that reaction and temperature, is then overlaid on this plot. If the Gamow peak is a good description of the effective region of thermonuclear burning, the most significantly contributing

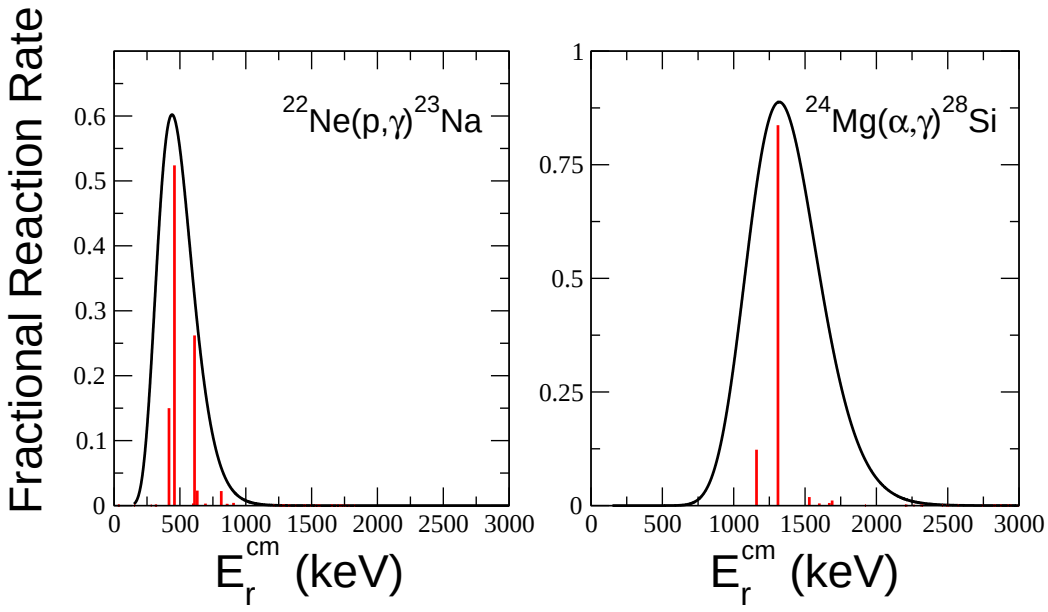

Figure 2.2: The fractional contributions to the total reaction rate for individual resonances in ^{22}Ne(p,γ)^{23}Na at T = 0.7 GK (left panel) and ^{24}Mg(a,γ)^{28}Si at T = 0.8 GK (right panel) are shown in red. The corresponding Gamow peak (black curve) is also included. Resonance strengths adopted from Refs. [10, 11]

resonances will fall within the energy range spanned by $E_0 \pm \frac{1}{2}\Delta$ on this plot.

Figure 2.2 shows the Gamow peak and the fractional contributions to the reaction rate of individual resonances in ^{22}Ne(p,γ)^{23}Na and ^{24}Mg(α, γ)^{28}Si at stellar temperatures of 0.7 GK and 0.8 GK, respectively. It is important to reiterate the fact that the Gamow peak is only strictly defined for nonresonant reactions. It is apparent, however, from Fig. 2.2 that the Gamow peak concept may play a crucial role in narrow resonant thermonuclear reactions under the proper conditions, since it is clearly a good description of the energy range of thermonuclear burning in these examples. The remainder of Chap. 2 focuses on identification of conditions in which the Gamow peak concept is a good description of the thermonuclear burning region as well as the limitations of this approximation.

2.2 Fractional Reaction Rate Contributions

As discussed in Sec. 2.1, the Gamow Peak concept is a widely used tool for the determination of the resonances that will contribute most significantly to the total reaction rate for a charged particle reaction at a given temperature. In this section, the validity of the Gamow peak approximation will be explored through the analysis of ten (p,γ) reactions including the target nuclei: ^{21,22}Ne, ^{23}Na, ^{25,26}Mg, ^{27}Al, ^{29,30}Si, ^{31}P and ^{35}Cl and three (a,γ) reactions including the target nuclei: ^{20}Ne, ^{24}Mg and ^{28}Si. These nuclei constituted the available literature data at the time of this work. It is important to have measured all of the resonances in each analyzed energy interval to ensure that missing resonances do not affect the observed trends. These resonance strengths are available in Refs. [10, 11]. A quantitative comparison of these target nuclei will be discussed in the following sections.

Figure 2.3 continues the analysis of the fractional contribution to the reaction rate from individual resonances from section 2.1, exploring a wider range of temperatures. Something very interesting begins to emerge. From Eq. 2.2 it is clear that the contribution to the total rate for a specific resonance is highly energy dependent, owing to the dependence of the particle partial width on the Coulomb barrier. The distribution of resonances contributing to the total rate should shift in energy when there is a change in the temperature. Thus, as the temperature rises, the distribution of resonance contributions is expected to shift to higher energy as seen in Fig. 2.3. Likewise, the Gamow peak also shifts to higher energy as the temperature increases and if the Gamow peak is a valid description of the significantly contributing resonances, this should mirror the shift seen in the distribution of resonances. These six plots are representative of the effects seen for each of the targets studied.

There are three main characteristics of Fig. 2.3 which should be noted. The first is that at lower temperatures (T $\sim 0.5 - 0.7$ GK) the approximation of the Gamow peak as the description of the thermonuclear burning region appears to be accurate. The second issue is that at lower temperatures a relatively small number of resonances contribute significantly to the total reaction rate, as is clearly displayed in Fig. 2.3. As temperature increases, more resonances become important and this has two effects. First, contributions from only a few resonances at lower temperatures results in scatter in the locations of the significantly contributing resonances. Thus, the bulk of the reaction rate contribution may not be found right at the center of the Gamow peak but should still be within the previously

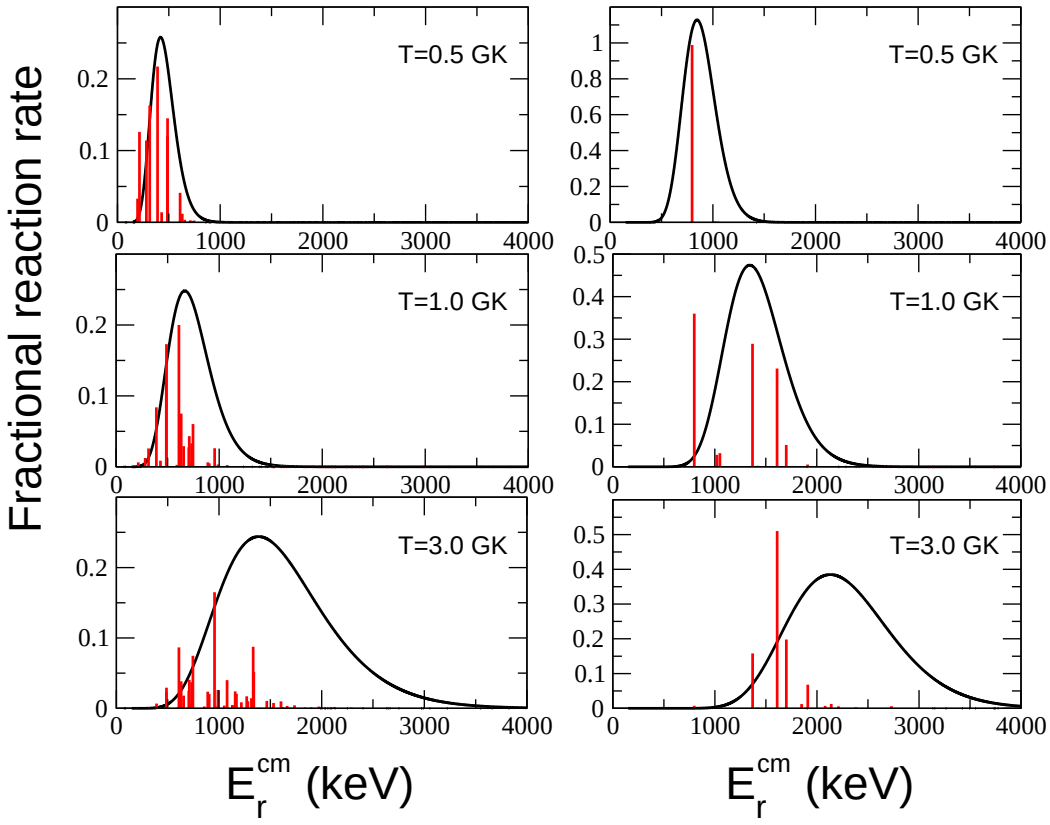

Figure 2.3: Fractional reaction rate contribution for individual resonances compared to the Gamow peak for the ^{27}Al(p,γ)^{28}Si (left column) and ^{20}Ne(α,γ)^{24}Mg (right column) reactions at stellar temperatures of T = 0.5, 1.0 and 3.0 GK. Resonance strengths adopted from Refs. [10, 11]

derived region of $E_0 \pm \frac{\Delta}{2}$. The specific position of these resonances is determined by the structure of the compound nucleus. This will result in variations in the energy position of the main contribution to the rate from one target to the next and scatter in the relative position of this main contribution to E_0. One advantage of the fact that only a few resonances dominate at low temperatures is that this narrows down the experimentally significant range for which measurements need to be improved in order to improve the reaction rate.

The third characteristic seen in Fig. 2.3 is that at high temperatures the energy region of thermonuclear burning is no longer described by the Gamow peak. This occurs once the stellar temperature reaches a few GK. It is clear from these six plots that the true energy burning window, at these higher temperatures, lies in a region below the Gamow peak. This suggests that there are limitations to the Gamow peak approximation of the energy range of interest and that care must be taken when employing this approximation. There are three main questions to be considered here:

(i) When is the Gamow peak description of the effective thermonuclear burning window applicable and when and why does it break down?

(ii) At high temperatures, why is the effective thermonuclear burning window located at lower energies compared to the Gamow peak?

(iii) Is there a consistency from one reaction to another in the position of the effective thermonuclear burning region at these higher temperatures?

2.3 The Effective Thermonuclear Energy Region

Here a new definition for the effective stellar burning window is introduced and it will be shown that it is more reliable than the Gamow peak concept. For this purpose, it is necessary to define a few new variables. First, E' is defined as the median value of the distribution of fractional reaction rate contributions. The median is calculated by computing the cumulative fractional resonance contribution function. This function is then interpolated and the resonance energy corresponding to any desired percentile can then be found. A percentile of 50% is chosen for the median, selecting an effective energy which should describe the actual location of the thermonuclear burning region. The

Gamow Peak	Effective Thermonuclear Energy Region (ETER)
$E_0 \pm \frac{\Delta}{2}$	E_{lower} to E_{upper}
$E_0 = 0.1220 \left(Z_p^2 Z_t^2 \frac{m_p m_t}{m_p + m_t} T_9^2 \right)^{\frac{1}{3}}$	E': median of cumulative distribution
$\Delta E_0 = 0..2368 \left(Z_p^2 Z_t^2 \frac{m_p m_t}{m_p + m_t} T_9^5 \right)^{\frac{1}{6}}$	ΔE': 8^{th}-92^{nd} percentiles of cumulative distribution

Table 2.1: Definitions for the two energy regions; the Gamow peak (left column) and the newly introduced Effective Thermonuclear Energy Region (right column).

width of the effective energy range is defined in analogy to the calculation of Δ, the width of the Gamow Peak. The width of the effective energy burning window, ΔE', will then be described as the energy range covered by the 8^{th} - 92^{nd} percentiles of the cumulative reaction rate contribution. By analogy with the Gamow peak, this range contributes 84% to the total reaction rate. The energy range $E' \pm \frac{1}{2}\Delta E'$ is defined as the Effective Thermonuclear Energy Region (ETER).

Table 2.1 displays the properties of the Gamow peak and the analogous quantities for the ETER. It is important to note that there is a fundamental difference between these two descriptions of the relevant thermonuclear burning regions. The Gamow peak is an approximation that is meant to predict the energy range of resonances that will contribute to the total reaction rate. The ETER, however, is a precise description of the resonances that are contributing to the total reaction rate. The Gamow peak is a very attractive tool because it is simple to calculate. In contrast, calculation of the ETER is far more complex because it requires all of the resonance strengths and energies. The ETER will be a very useful concept for testing the validity and limitations of the Gamow peak description of narrow resonant thermonuclear reactions but at this point it is not predictive. In Sec. 2.5 the ETER for each of the targets studied will be presented and compared to the Gamow peak description. From this comparison it will be possible to determine some general trends for such reactions. The ETER will be a more useful tool if general statements about its behavior can be made.

Figure 2.4 illustrates the situation for ^{23}Na(p,γ)^{24}Mg at a stellar temperature of 2.5 GK. The positions of the ETER and the Gamow peak will vary with reaction and temperature, but Figure 2.4 shows the general behavior, which clearly illustrates that the Gamow peak is not a good description of the ETER in ^{23}Na(p,γ)^{24}Mg at T = 2.5 GK. A detailed comparison of all the target nuclei from section 2.1 is presented and analyzed in Sec. 2.5.

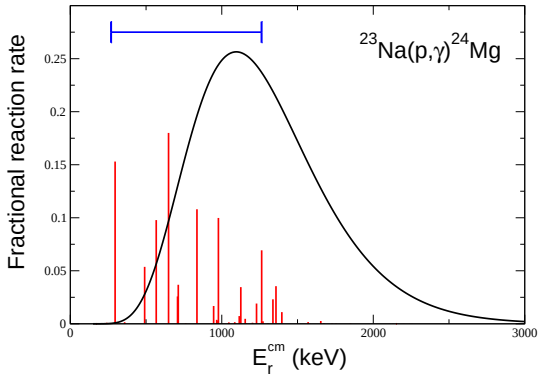

Figure 2.4: Relative reaction rate contributions from individual resonances in ^{23}Na(p,γ)^{24}Mg at T = 2.5 GK (red lines) along with the Gamow peak (black line). The newly defined Effective Thermonuclear Energy Region (ETER) is denoted by a blue bar. Resonance strengths adopted from Refs. [10, 11].

We originally considered an ETER that covered 68% of the total reaction rate, as compared to the present 84% coverage. However, the same qualitative trends emerge. The early tests compared a coverage width of 68% and two different definitions for its placement. The first definition was a 68% coverage range which is centered around E'. The second definition was the smallest 68% coverage range which also includes E'. These two definitions for the width of the ETER are compared in Fig. 2.5 for the ^{30}Si(p,γ)^{31}P and the ^{22}Ne(p,γ)^{23}Na reactions. There is not a large discrepancy in the resulting ETER for the two coverage definitions in either of the two reactions. The energy ranges described by the two definitions of the ETER are compared for three separate stellar temperatures of T = 0.8, 4.0 and 7.0 GK in Fig. 2.6. These energy regions are plotted as a function of target mass number for each of the three temperatures. The result is that there is not a large discrepancy in the energy ranges described by either of the two coverage definitions for any of the ten reactions. This suggests that the choice of coverage definition is relatively unimportant and that the definition chosen for the current ETER will be consistent with any other reasonable 84% coverage definition.

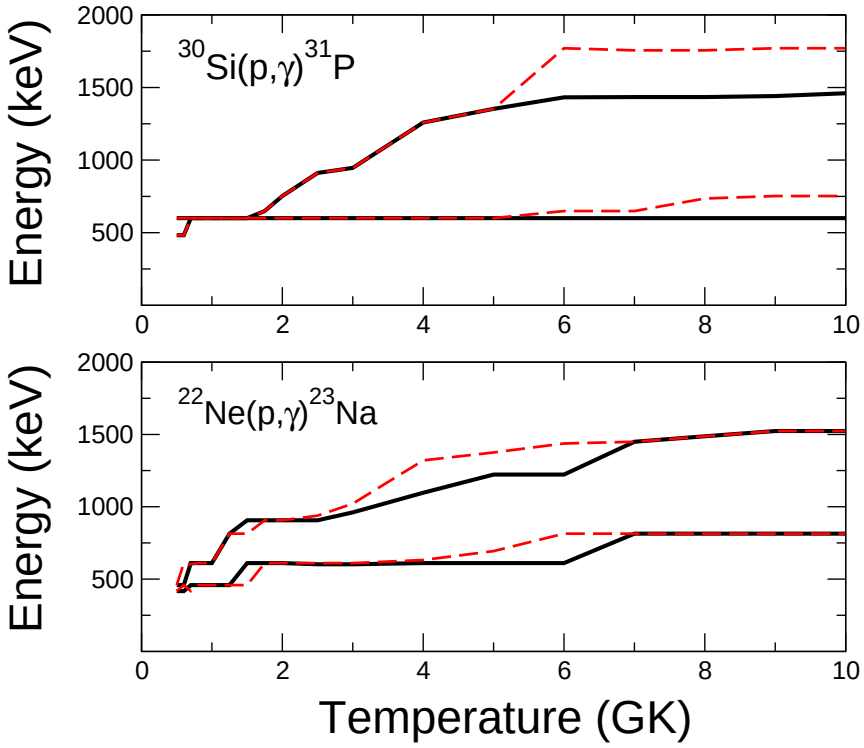

Figure 2.5: Comparison of the effective energy window resulting from the two different methods mentioned in the text for determining the 68% coverage range for the reaction rates of ^{30}Si(p,γ)^{31}P (top panel) and ^{22}Ne(p,γ)^{23}Na (bottom panel). The red dashed lines are the 68% coverage range centered around E' and the black lines are the smallest 68% coverage range that includes E'. Resonance strengths adopted from Refs. [10, 11]

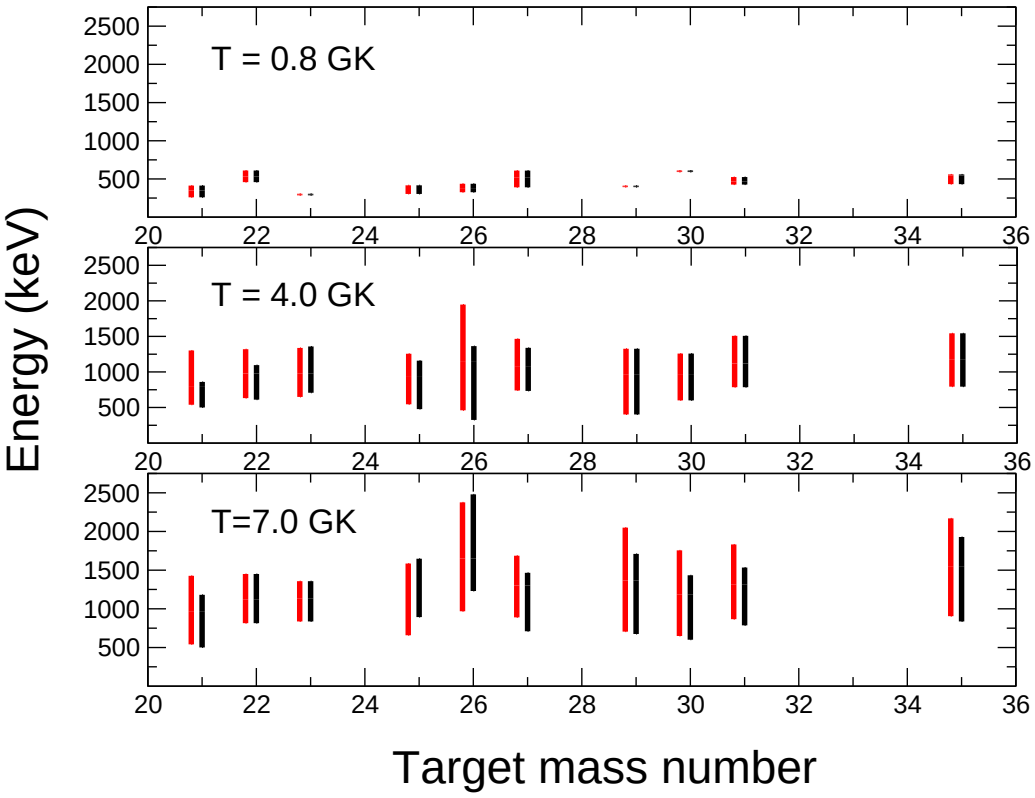

Figure 2.6: Comparison of the effective energy window resulting from a 68% coverage range centered around E' (red bars) and the smallest 68% coverage range including E' (black bars). The mass number of the target nucleus for each (p,γ) reaction is plotted on the horizontal axis. Resonance strengths adopted from Refs. [10, 11]

2.4 The Dependence of the Reaction Rate on Partial Widths

The goal of this section is to explain the trend illustrated by Fig. 2.3. For the purposes of the following presentation, it is assumed that only two decay channels are open for the reaction of interest: the γ-ray and particle channel. Recall that the Gamow-peak description of the true region of thermonuclear burning breaks down as the stellar temperature increases. As temperature increases the ETER is shifted to lower energy compared to the Gamow peak. This is seen in all of the reactions studied. It is clear that as the stellar temperature increases, there is a preference for contributions from lower energy resonances. The explanation for this surprising result can be easily understood when considering the role of the partial widths in Eqs. 1.20 and 2.1. The Gamow peak concept for narrow resonances originally arose from considering the energy dependence of the particle partial width, $\Gamma_a \propto e^{-2\pi\eta}$, when $\Gamma_a \ll \Gamma_\gamma$. The γ-ray partial width, however, is typically on the order of meV - eV and has a much weaker energy dependence than the particle partial width [1]:

$$\Gamma_\gamma \propto (E+Q)^{2L+1}. \tag{2.3}$$

If $\Gamma_\gamma \ll \Gamma_a$, the strength becomes

$$\omega\gamma \approx \omega\Gamma_\gamma. \tag{2.4}$$

and the reaction rate takes the form

$$< \sigma\nu >_i \propto e^{-(\frac{E_r}{kT})}\Gamma_\gamma. \tag{2.5}$$

Notice that this expression does not exhibit a Gamow peak. In this case, the major energy dependence is in the exponential term, which favors resonances with lower resonance energies.

This means that the Gamow peak will be a useful tool if all of the resonances that contribute significantly to the total reaction rate have $\Gamma_a \ll \Gamma_\gamma$, which usually pertains at low stellar temperatures. The average particle energy increases with increasing temperature and at some point resonances with $\Gamma_\gamma \ll \Gamma_a$ begin to contribute to the total reaction rate. These resonances were shown to favor contributions from lower energy resonances. This means that as the temperature is increased there is a

contribution from resonances with $\Gamma_a \ll \Gamma_\gamma$ and resonances with $\Gamma_\gamma \ll \Gamma_a$, resulting in an ETER which is shifted to lower energies compared to the Gamow peak.

Also, as the stellar temperature increases the ETER will shift to higher energy (as does the Gamow peak). This is because the resonances with $\Gamma_\gamma \ll \Gamma_a$ will have the largest contributions to the reaction rate from the same lowest energy resonances, regardless of temperature. These contributions will be combined with contributions from resonances with $\Gamma_a \ll \Gamma_\gamma$. These will follow the energy behavior of the Gamow peak, which increases smoothly with increasing temperature. The combination of these two effects results in an ETER which will increase in energy as the stellar temperature increases.

Continually increasing the stellar temperature leads to a distribution of thermonuclear particles which is shifted to higher energies and eventually an environment where resonances with $\Gamma_a \ll \Gamma_\gamma$ are no longer significantly contributing. Thus, at high enough stellar temperatures, it is expected that the effective energy burning window should eventually become constant as the temperature is raised since resonances with $\Gamma_\gamma \ll \Gamma_a$ have significant contributions from the same lower energy resonances.

For resonances which satisfy $\Gamma_\gamma \approx \Gamma_a$, not fitting either of the limiting cases discussed here, the resulting resonance strength is much more complicated and does not have a simple energy dependence. The number of resonances for which the particle and γ-ray partial widths will be of the same magnitude, however, will be very few since Γ_a varies by many orders of magnitude. This means that resonances with $\Gamma_\gamma \approx \Gamma_a$ should not contribute significantly, as a group, to the total reaction rate because they are so rare and can be disregarded for the current discussion.

2.5 Comparison of the Effective Thermonuclear Energy Range with the Gamow Peak

The purpose of this section is to compare results for the calculation of the ETER for ten (p,γ) reactions to the energy range predicted by the Gamow peak. First, it is interesting to consider a specific reaction and compare the behavior of the ETER as a function of temperature with that of the Gamow peak. Consider Fig. 2.7 showing the ETER and the Gamow peak as a function of temperature for the ^{35}Cl(p,γ)^{36}Ar reaction. The red lines correspond to the upper and lower bounds of the ETER and the black lines are the upper and lower bounds of the Gamow peak. There a couple very interesting

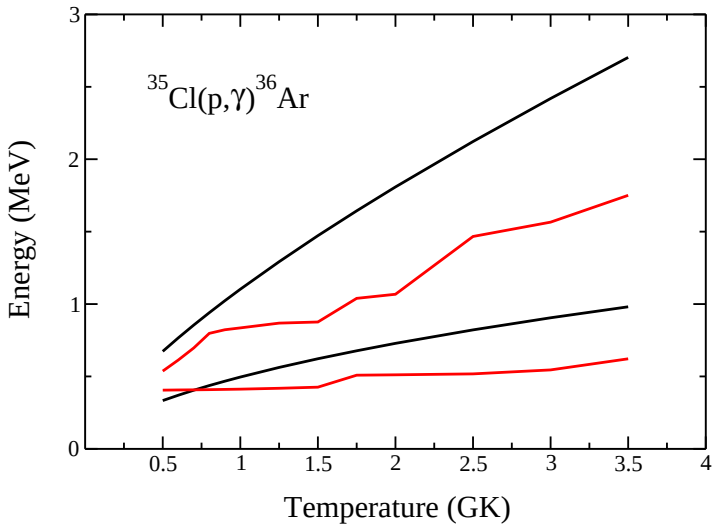

Figure 2.7: Gamow peak (black lines) and ETER (red lines) for the ^{35}Cl(p,γ)^{36}Ar reaction. Resonance strengths adopted from Refs. [10, 11]

features to notice here.

The first feature is that, at the lowest temperatures shown, the ETER is completely within the Gamow peak. This is consistent with the previous discussion since at lower temperatures the vast majority of contributing resonances are those which reside in the $\Gamma_a \ll \Gamma_\gamma$ realm and should be described well by the Gamow peak. The narrowness of the effective energy window at these lowest temperatures can easily be explained by the dominance of a few low energy resonances at these lower temperatures. The stellar temperature is not high enough to populate the higher-lying resonances, resulting in a very narrow ETER.

Another important feature of Fig. 2.7 is that the differences between the Gamow peak description and the ETER grow increasingly larger as stellar temperature increases. This is expected, since, at the higher temperatures, the resonances which satisfy $\Gamma_a \gg \Gamma_\gamma$ are beginning to be populated, resulting in a preference for lower energy resonances that may actually be outside the Gamow peak at these higher temperatures. This is the reason that the ETER sits outside the lower limit of the Gamow peak as the temperature increases. It is also clear that the Gamow peak continues to shift to much higher energies as the temperature increases compared to the effective energy window, which is again explained by the preference for lower energy resonances at higher temperatures.

The last note of interest concerning Fig. 2.7 is that, starting at relatively low temperatures, the

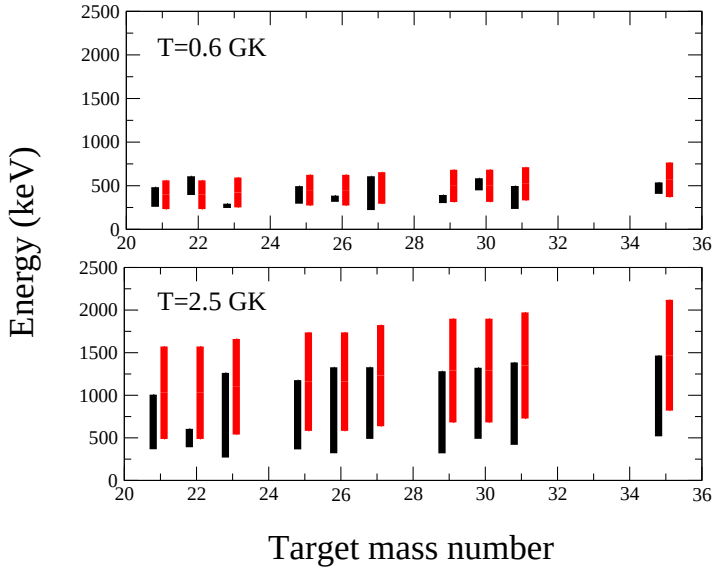

Figure 2.8: Gamow peak (red bars) and ETER (black bars) plotted versus target mass number for proton-capture reactions on ^{21,22}Ne,^{23}Na,^{25,26}Mg,^{27}Al,^{29,30}Si,^{31}P and ^{35}Cl at temperatures of T = 0.6 GK (top) and T = 2.5 (bottom). Resonance strengths adopted from Refs. [10, 11]

entire ETER is located below E_0. This is surprising because, if the Gamow peak is a valid description of the energy burning region, there should be scatter around the center of the Gamow peak, E_0. This is clearly not the case at a temperature as low as $T \approx 2$ GK. Therefore, at these temperatures it is improper to refer to the Gamow peak because it is no longer a valid description of the ETER in this thermonuclear environment.

Figure 2.8 compares the ETER with the Gamow peak for all of the ten target nuclei at both a low stellar temperature (T = 0.6 GK) and a relatively high temperature (T = 2.5 GK). First, the comparison of the ETER with the Gamow peak at T = 0.6 GK supports the fact that the Gamow peak is a good description of the effective thermonuclear burning region at low temperature. The ETER at T = 0.6 GK seems to be well within the Gamow peak for each of the ten reactions, suggesting that the reaction is proceeding through resonances which fulfill the $\Gamma_a \ll \Gamma_\gamma$ requirement that is the necessary condition for the application of the Gamow peak. There is also a good deal of scatter in the position of the ETER for the reactions plotted at low temperature, which can again be explained by the dominance of the contributions of only a few, very strong, resonances. The ETER, however, is still consistently within the energy range predicted by the Gamow peak.

At higher temperatures a very interesting behavior emerges. As was the case with the ^{35}Cl(p,γ)^{36}Ar reaction discussed earlier, it is clear that at high temperature the ETER consistently lies below E_0. The Gamow peak no longer agrees with any of the ten ETERs at 2.5 GK. Similarly to the case of ^{35}Cl(p,γ)^{36}Ar, the two descriptions of the energy burning window will only diverge even further as the stellar temperature is increased. The effective energy window is not only located below E_0, but is also much narrower than the Gamow peak.

The fact that more resonances will contribute to the total reaction rate at high temperature leads to an averaging of specific nuclear structure properties of individual levels. This should result in more consistency in the position of the ETER from one reaction to the next than was seen for the low temperature cases. Figure 2.8 shows that at T = 2.5 GK the effective energy window for each reaction is located at a similar position, which is near an energy of $E' \approx 0.8$ MeV. It is expected that the position of the ETER will remain nearly constant as the temperature increases since the newly contributing resonances give preference to those with lower resonance energies. Thus the added effects of higher energy resonances, as the temperature increases, will be small. This suggests that one may be able to predict the position of the effective energy burning window for other reactions that proceed through narrow, isolated resonances at higher temperatures.

2.6 Applications of the Effective Thermonuclear Energy Region

It has been shown that the blanket use of the Gamow peak for astrophysical applications is incorrect. Where, however, is the concept of the Gamow peak used for specific applications and calculations? One might ask if the use of the ETER will actually significantly change the results of these calculations.

One area where the Gamow peak is used for astrophysical applications is in the calculation of reaction rates at very high temperatures. These are temperatures at which very closely spaced energy levels in the compound nucleus begin to become important. This requires the use of statistical models for the calculation of reaction rates. These statistical models need to be matched to the experimentally measured values at the lower energies, where the resonances are still able to be resolved individually. The magnitude of the cross sections from statistical models is not always well known and the

experimental rates allow for a proper normalization procedure. It is interesting that the Gamow peak concept is used as a tool in these matching procedures at temperatures well above where the Gamow peak concept was shown to no longer describe the ETER. The use of the Gamow peak at these higher temperatures is not only incorrect, but may possibly invalidate the resulting reaction rate calculations.

The specific statistical model that will be discussed here is the Hauser-Feshbach model. Reference [12] contains a similar derivation of the Gamow peak contribution to the reaction rate as was presented in this chapter. Also discussed in Ref. [12] is the spacing of nuclear energy levels at higher energies, which correspond to higher stellar temperatures. Reference [12] states that the Hauser-Feshbach model is applicable if there exist ten levels in a compound nucleus which fall in the Gamow peak defined by that reaction at a given stellar temperature. So, the criterion for the applicability of the statistical model involves the Gamow-peak concept which may no longer exist at such temperatures. For this application, the ETER should instead be used to allow for a consistent description of the range of applicability of the statistical model in question, which does not make use of the Gamow peak at high temperatures.

Along with the previous example, the Gamow peak concept is also used in conjunction with the Hauser-Feshbach model as a tool for determining the proper matching temperature for transitioning from experimentally measured reaction rates to those calculated using a statistical model in Refs. [13, 14]. The Gamow peak is assumed to be the proper description of the effective burning window for a thermonuclear reaction. The experimentally determined rates are then used as long as the resolvable resonances fall within a region defined by the Gamow peak concept. That is, the experimental reaction rates will be used as long as the following condition is met [15]:

$$E_{\text{res}}^{\text{max}} \geq E_0 + n\Delta, \tag{2.6}$$

where n is a constant. For simplicity n = 1 is usually chosen but could in principle be different. As long as the resonance with the maximum experimentally measured energy, $E_{\text{res}}^{\text{max}}$, lies outside $\text{E}_0 + \Delta$, the experimentally determined reaction rates will be used. It is important to note that the above range is not strictly the Gamow peak, but uses the Gamow peak concept.

The temperature dependence of E_0 and Δ can now be inserted to Eq. 2.6 to find a matching

temperature, T_{match}, which solves the following equation:

$$E_{res}^{max} = cT_9^{\frac{2}{3}} + n\left(dT_9^{\frac{5}{6}}\right). \tag{2.7}$$

T_{match} is then the temperature at which the experimentally determined reaction rates are used to normalize the results calculated from the statistical model. The constants c and d are defined by Tab. 2.1. The reaction rate below T_{match} is found using the experimental results and the reaction rate above T_{match} is found using the statistical model which was normalized to the experimental rates at T_{match}. The Gamow peak concept provides a very simple prescription for matching the reaction rates, and for that reason is a very attractive result.

If, instead, the ETER is used, are there significant differences in the resulting reaction rates for higher temperatures? The experimentally determined rates will not be altered, since they are a simple sum over the known resonances, but the range over which they are used may be different. If a different definition for the effective energy range is used, this will lead to a new normalization factor for the statistical model, since the experimental and statistical rates are now normalized at a different T_{match} than the one found using the Gamow peak concept. The new equation for finding the proper matching temperature becomes:

$$E_{res}^{max} \geq E' + n\Delta E'. \tag{2.8}$$

This allows the matching condition to be set by the ETER. The problem with this procedure is that the matching temperature cannot be calculated analytically because the temperature dependence of E' and $\Delta E'$ is not known from one reaction to the next. This is one reason that the Gamow peak concept is much easier to use for this matching. The values for the matching temperature using the ETER for the calculation of T_{match} and those obtained using the Gamow peak concept are compared in Tab. 2.2.

It is clear, from Tab. 2.2, that the matching temperatures calculated using the Gamow peak extend well into the region where the Gamow peak no longer exists. This means that the temperature where the experimental reaction rates are matched to statistical models should no longer be calculated using the Gamow peak concept. Also, there is a vast difference in the matching temperatures found using the Gamow peak concept versus the ETER in most of the reactions shown. This is expected since, at

Reaction	E_{max}^{exp} (keV)	T_{match} (GK) via $E_0 \pm \Delta$	T_{match} (GK) via E'$\pm\Delta'$
^{20}Ne$(\alpha,\gamma)^{24}$Mg	5011	3.22	10.0
^{21}Ne(p,$\gamma)^{22}$Na	1937	2.23	8.96
^{22}Ne(p,$\gamma)^{23}$Na	1823	2.05	4.05
^{23}Na(p,$\gamma)^{24}$Mg	2256	2.56	10.0
^{23}Na(p,$\alpha)^{20}$Ne	2328	2.67	3.53
^{24}Mg(p,$\gamma)^{25}$Al	2311	2.49	9.56
^{24}Mg$(\alpha,\gamma)^{28}$Si	5240	2.97	10.0
^{25}Mg(p,$\gamma)^{26}$Al	1762	1.73	3.25
^{26}Mg(p,$\gamma)^{27}$Al	2867	3.32	4.31
^{27}Al(p,$\gamma)^{28}$Si	3819	4.60	10.0
^{27}Al(p,$\alpha)^{24}$Mg	2967	3.29	3.62
^{28}Si(p,$\gamma)^{29}$P	2991	3.16	10.0
^{29}Si(p,$\gamma)^{30}$P	3075	3.28	5.05
^{30}Si(p,$\gamma)^{31}$P	2929	3.07	5.18
^{31}P(p,$\gamma)^{32}$S	1963	1.72	2.98
^{31}P(p,$\alpha)^{28}$Si	1963	1.72	1.57
^{32}S(p,$\gamma)^{33}$Cl	2470	2.23	8.56
^{35}Cl(p,$\gamma)^{36}$Ar	2828	2.57	5.08
^{35}Cl(p,$\alpha)^{32}$S	2838	2.58	2.25
^{36}Ar(p,$\gamma)^{37}$K	2575	2.17	7.39
^{40}Ca(p,$\gamma)^{41}$Sc	1887	1.32	1.96

Table 2.2: Values of the matching temperatures are tabulated above. The specific reactions analyzed (column 1) are presented, along with the corresponding highest energy experimentally measured resonance (column 2) for that reaction. The measured resonance strength data are from Refs. [10, 11]. The Hauser-Feshbach calculations were evaluated using the Non-smoker code [12]. The resulting matching temperature using the Gamow peak description (column 3) and the ETER (column 4) are included.

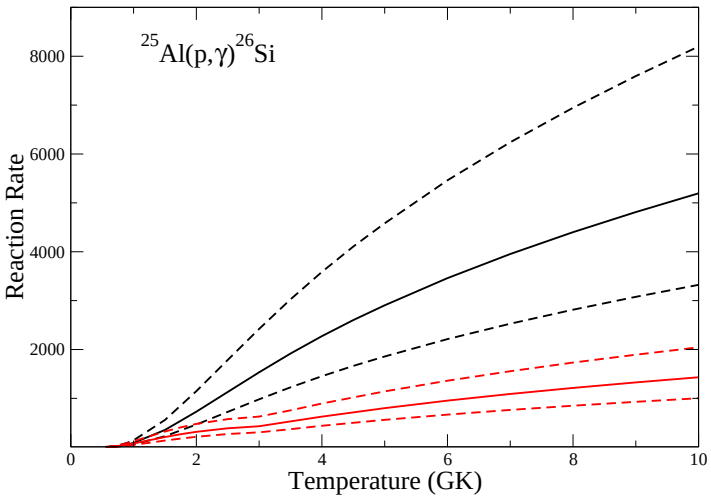

Figure 2.9: Reaction rates matched to Hauser-Feshbach calculations using the Gamow peak concept (black) and the ETER (red) for the reaction ^{25}Al(p,γ)^{26}Si. The measured resonance strength data are from Refs. [10, 11]. The Hauser-Feshbach calculations were obtained from the Non-smoker code[12].

these higher temperatures, it has been shown that the ETER is located significantly lower in energy than the Gamow peak. Thus, matching the edge of the ETER with the maximum resonance energy will produce a much higher temperature than that calculated using the edge of the Gamow peak.

Figure 2.9 illustrates the differences in the calculated values for the reaction rate, as a function of temperature, when the matching temperature is found using the Gamow peak compared to the result using the ETER. This demonstrates that there exists a large discrepancy in the final rates when using the ETER versus the Gamow peak concept. Since the final results for the reaction rates differ significantly using the ETER, it is obvious that the Gamow peak concept leads to an incorrect reaction rate and cannot be used in this case. Not all the reactions analyzed show as large a deviation as seen in figure 2.9, but they all differ noticeably and thus the ETER must be used when determining the matching temperature for reaction rate calculations. See also figure 2.10 for a similar comparison using the ^{29}Si(p,γ)^{30}P reaction.

The work described in this chapter has been published in Newton et al. [15] and Newton et al. [16] to which the reader is referred for details.

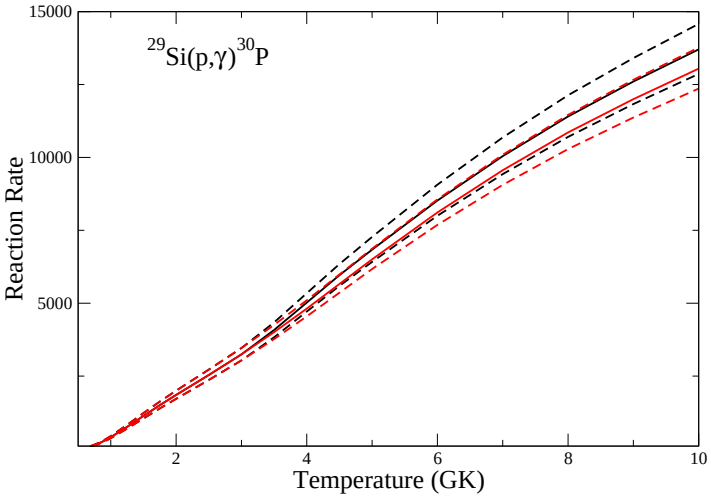

Figure 2.10: Reaction rates matched to Hauser-Feshbach calculations using the Gamow peak concept (black) and the ETER (red) for the reaction ^{29}Si(p,γ)^{30}P. The measured resonance strength data are from Refs. [10, 11]. The Hauser-Feshbach calculations were obtained from the Non-smoker code [12]

3 Measuring E_r^{lab} = 193 keV in ^{17}O(p,α)^{14}N

3.1 Introduction

Hydrogen burning of ^{17}O is important in several stellar environments including red giants, asymptotic giant branch stars, massive stars, and classical novae. Of specific interest to the current work is a resonance at E_r^{lab} = 193 keV in ^{17}O + p that was shown by Coc et al. to be of particular importance to classical novae [17]. This resonance was first observed in the (p,γ) channel by Fox et al. [18] in a measurement at LENA and was remeasured independently by Fox et al. [7]. These measurements reported a resonance energy of $E_r^{lab} = 193.2 \pm 0.9$ keV and a resonance strength of $\omega\gamma_{p\gamma}$ = (1.2 $\pm$ 0.2)$\times 10^{-6}$ eV. The corresponding resonance strength in the α-channel was later measured by Chafa et al. [19] and reported to be $\omega\gamma_{p\alpha}$ = (1.6 $\pm$ 0.2)$\times 10^{-3}$ eV. In this experiment, the (p,γ) strength was also measured using an activation method with the same targets used for the (p,α) measurement. This initially resulted in a resonance strength of $\omega\gamma_{p\gamma}$ = (3.4 $\pm$ 0.6)$\times 10^{-6}$ eV [19] and was subsequently revised by Chafa et al. to $\omega\gamma_{p\gamma}$ = (2.2 $\pm$ 0.4)$\times 10^{-6}$ eV [20]. This value differs significantly from the previously measured value of Fox et al. This discrepancy may significantly affect the calculation of the total reaction rate, ultimately affecting the nucleosynthesis of specific isotopes in classical novae, as explained in Chap. 1.

The activation method performed by Chafa et al. [21] led to a value for the (p,γ) strength which was relative to that of the (p,α) strength, while Fox et al. measured the strength of this resonance directly by detecting the prompt gamma rays emitted by the target. In the current work, the E_r^{lab} = 193 keV resonance in ^{17}O(p,α)^{14}N is measured to both verify the previous result of Ref. [21] and elucidate the source of the discrepancies in reported (p,γ) resonance strengths. This measurement was performed relative to the E_r^{lab} = 151 keV resonance in ^{18}O(p,α)^{15}N which has a substantial, well known strength of $\omega\gamma$ = 0.167 $\pm$ 0.012 eV [1] and is the same reference resonance strength used by

Chafa et al.

3.2 Experimental Setup

The experimental equipment used for the measurement of the strength of the resonance at E_r^{lab} = 193 keV in ^{17}O(p,α)^{14}N was similar to that of Chafa et al. [21] and used a proton beam from the LENA 1 MV JN Van de Graaff accelerator in the energy range of 140 - 210 keV. This spanned the energy range necessary to measure the reference resonance located at $E_r^{lab} = 151$ keV in ^{18}O(p,α)^{15}N and the new $E_r^{lab} = 193$ keV resonance in ^{17}O(p,α)^{14}N. The beam energy was calibrated using this reference resonance and a precise resonance energy of E_r^{cm} = (150.82 $\pm$ 0.09) keV [22]. The beam passed through a copper pipe, cooled with liquid nitrogen, that ended in an aperture biased to -300 V to suppress the emission of secondary electrons from the target as well as to prevent electrons produced by the beam from striking apertures upstream of the target. The suppressor was positioned in close geometry to the target. The experimental setup also consisted of two oxygen enriched targets housed within a target chamber and a surface barrier silicon detector. These are discussed in detail in the following sections. The targets were directly cooled using chilled water that ran behind the target backings.

3.2.1 The 45° Target Chamber

Figure 3.1 illustrates the "45° target chamber" configuration in which the target is mounted at a 45° angle with respect to the beam direction. This allows for a large angular acceptance for detection of the outgoing α-particles, since the forward angles are not blocked by the shadow of the target. There are two detector ports available, corresponding to detection angles of 135° and 90° with respect to the beam direction and the center of the target. The target chamber served as a Faraday cup for beam integration. It was necessary to redesign the beam-line to allow the copper cold trap to be as close as possible to the target, while not blocking the view of the detector. Though this target chamber allows for measurements at 135° and 90°, only one angular position was utilized at a time and the other port was used to view the scintillation produced by the beam on target (it was necessary to debias the working detector while looking through the viewer window). The data taken at 90° were

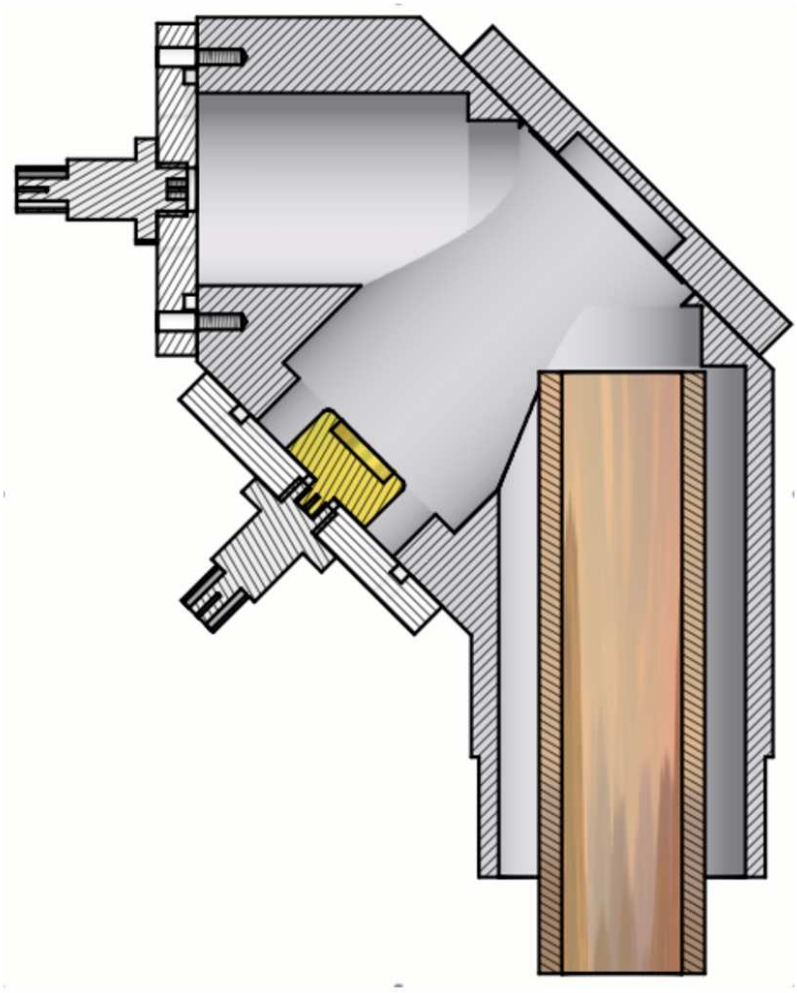

Figure 3.1: An illustration of the 45° target chamber used for measurement of E_r^{lab} = 193 keV in $^{17}O(p,\alpha)^{14}N$. Drawing compliments of Johnny Cesaratto

significantly affected by the sensitivity of the detector efficiency to the beam position. It was found that the measurements were taken with the beam slightly off center of the target. For this reason, the data taken from the 135° port were much more reliable and will be used for determination of the resonance strength of interest. The actual detection angle was found to be 133° as a result of the misalignment of the beam on target. Data from only one angular position will not allow for measurement of the angular distribution of the emitted α-particles, but is sufficient for measurement of the resonance strength since the angular distribution expected for the $E_r^{lab} = 193$ keV resonance in ^{17}O(p,α)^{14}N was measured by Chafa et al. [21] and will be used in the final analysis of the resonance strength.

3.2.2 The Silicon Surface Barrier Detector

The reaction α-particles were detected using a 150 mm^2 silicon surface barrier detector. The detector was biased to 40 V for the best resolution and was mounted at a distance of 7.5 cm from the target at an angle of 135° from the beam-line to the center of target axis. The signals from the detector were amplified and collected using a multichannel analyzer (MCA). A foil was placed in front of the detector to shield it from the vast number of elastically scattered protons coming from the target, which can quickly damage the detector. The foil (described in Sec. 3.2.3) determines the maximum energy at which the measurement may be performed. Continuous monitoring of the dead time of the detector is critical for ensuring that protons are not leaking through the foil and flooding the detector. The dead time was measured using a precision pulse generator.

For a silicon detector the intrinsic efficiency should be unity, making the detection efficiency equal to the geometric efficiency. The measured efficiency was evaluated using a ^{241}Am source and the geometric efficiency was then calculated using the following equation from Ref. [1]

$$\eta_{peak} = \frac{1}{2}\left(1 - \frac{d}{\sqrt{d^2 + r^2}}\right), \tag{3.1}$$

where d and r represent the distance from detector to the target and the radius of the detector, respectively. For this setup the distance from detector to target was 7.53 cm and the radius of the detector was 0.69 cm. This gives a detection efficiency of η = 0.0021. The activity of the ^{241}Am source was

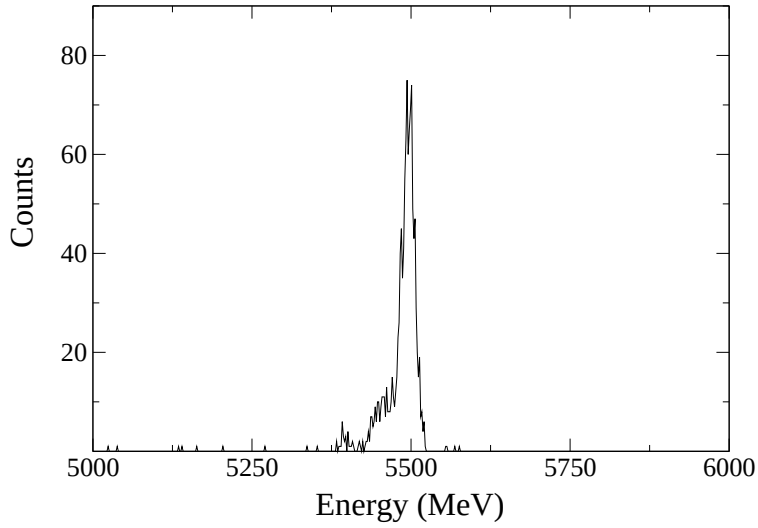

Figure 3.2: Measured MCA α-particle spectrum of a ^{241}Am source taken with the 150 mm^2 silicon detector used throughout this experiment. The displayed peak has a full width half max of $\approx$ 23 keV.

489.8 Bq. A representative MCA spectrum in which the ^{241}Am source is placed at the position of the target is presented in Fig. 3.2. The detector efficiency for measuring the α-particles from this source was found to be η = 0.00201 $\pm$ 0.0006. Since this measured efficiency agrees with the calculated geometric efficiency, the geometric efficiency η = 0.0021 was used as the detection efficiency of the Si detector.

The actual geometric detection efficiency was not critical since we were performing a relative strength measurement, making the ratio of detection efficiencies for the two strengths the quantity of interest. The geometric efficiency canceled out in this ratio, leaving only the ratio of the lab to center of mass conversion factors, $\frac{d\Omega^{lab}}{d\Omega^{cm}}$. This factor is energy dependent and was different for the two resonance energies, as discussed in detail in section 3.5.5.

3.2.3 The Thin Mylar Foil

The beam currents and energies required for this experiment made it necessary to place a foil in front of the detector to stop the elastically scattered protons incident on the detector, while allowing the α-particles of interest to pass through and be detected. Selection of the appropriate foil thick-

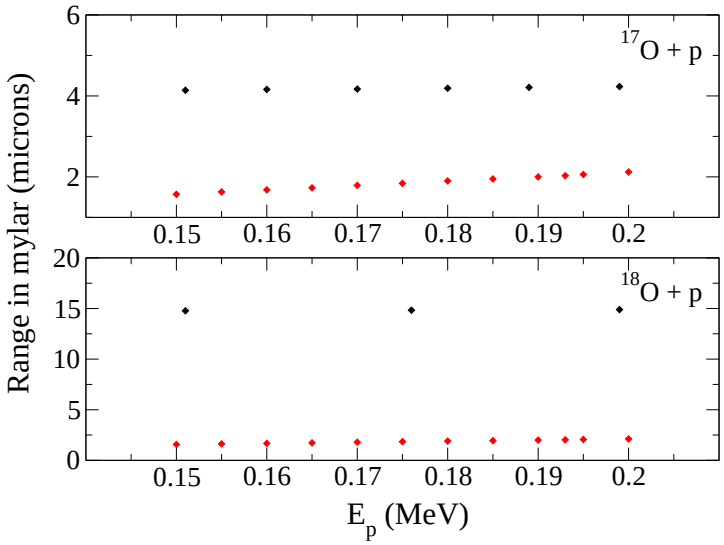

Figure 3.3: Range in mylar of protons (red points) and α-particles (black points) from the reactions ^{17}O(p,α)^{14}N (top panel) and ^{18}O(p,α)^{15}N (bottom panel) at a detection angle of 135°. The stopping power calculations were performed using SRIM2003 [23].

ness required kinematic calculations of the energy of the elastically scattered protons and α-particles incident on the detector as a function of the incoming beam energy.

There was a trade-off when choosing the thickness of the mylar foil. If the foil was too thick, the elastically scattered protons would be stopped, but the α-particles would lose too much energy to be distinguished from electronic noise. If the foil was too thin, protons could leak through and damage the detector. Fig. 3.3 shows the range in mylar for the elastically scattered protons and emitted α-particles for both the ^{17}O(p,α)^{14}N and ^{18}O(p,α)^{15}N reactions. The Q-value of the ^{18}O(p,α)^{15}N reaction is larger and results in a better separation between the range of protons and α-particles in mylar. Thus the foil thickness was constrained by the ^{17}O(p,α)^{14}N reaction kinematics. A foil thickness of 2.0 μm was chosen which will allow for measurements with bombarding energies up to $\approx$ 190-200 keV. The actual experimental limit depended on the uniformity of the mylar foil from the distributor and was determined by the measured α-particle spectra. This is discussed in detail in Sec. 3.3.

3.2.4 The Enriched ^{17}O and ^{18}O Anodized Targets

The targets used for this experiment were prepared by anodization of 0.5 mm thick, etched tantalum backings with ^{17}O or ^{18}O enriched water. The procedure for anodization is described in App. A.2. The targets were prepared by Chris Fox and are the same targets used in the previous study of the E_r^{lab} = 193 keV resonance in ^{17}O(p,γ)^{18}F [18, 7]. The supplier quoted enrichments of 90.7% and 97.5% for the ^{17}O and ^{18}O water, respectively. This process of anodizing oxygen onto tantalum has also been found to produce a well know stoichiometry of Ta_2O_5 and the anodizing voltage precisely determines target thickness [24]. The thickness of both targets was found to be $\approx$ 34 keV at their respective bombarding energies. The thickness of the target is determined from a plot of the thick-target yield curve (see Sec. 3.4). It should be noted that a major difference between the current measurement and that of Chafa et al. [19, 21] is the choice of targets. Chafa et al. employed targets made by implanting oxygen into tantalum.

An advantage to using anodized targets is that they are very stable. The beam currents used in this experiment were limited by the sensitivity of the detector to elastically scattered protons that passed through pinholes and nonuniformities in the foil fronting the detector and not by the intensity that the targets could withstand. Therefore, the beam currents used in this experiment, $\approx$ 20-80 μA, were well below the currents used on these same targets in the measurements of Refs. [7, 18]. Target thickness was measured, periodically, over the course of the experiment and no degradation was observed in either target. The thickness of the ^{17}O enriched target was evaluated using the trace amount of ^{18}O in that target, which enabled measurement of the 151 keV resonance in ^{18}O(p,α)^{15}N.

3.3 Fitting the Measured α-particle Peaks

Determination of yield was necessary for analyzing the measured pulse-height spectra. A representative on and off-resonance spectrum for the E_r^{lab} = 193 keV resonance in ^{17}O(p,α)^{14}N is provided in Fig. 3.4. There is a good separation between the α-particle peak and the low energy background. The position of the peak corresponds to the energy of the α-particles emitted from the target, which for this resonance is $E_\alpha \approx$ 1.0 MeV before the mylar foil and $E_\alpha \approx$ 0.4 MeV after passing through the foil. The low-energy background peak consists of contributions from electronic noise in the detector

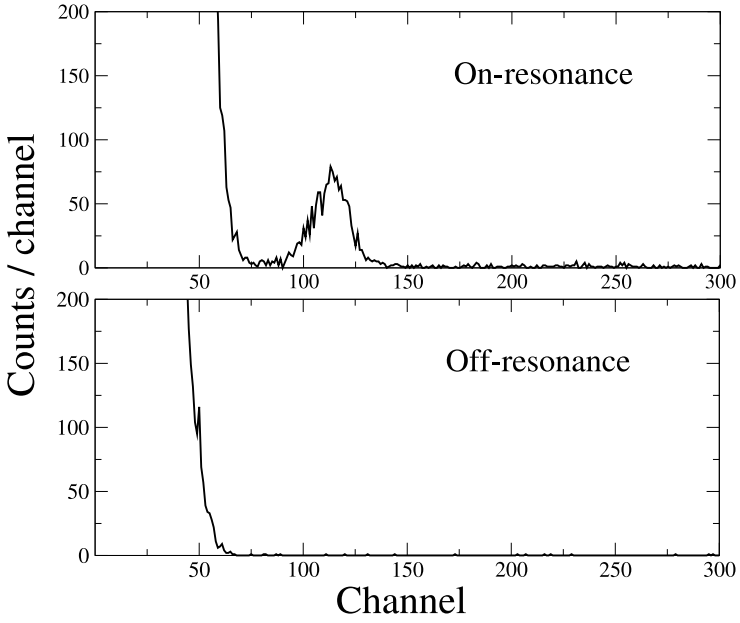

Figure 3.4: Measured spectra in ^{17}O(p,α)^{14}N. The top panel is taken on-resonance at E_p^{lab} = 195 keV and the bottom panel is off-resonance, taken at E_p^{lab} = 192 keV.

and associated electronics and contributions from protons that penetrated the mylar foil. As the proton bombarding energy increases, the low energy noise should move to higher energy since more protons will leak through the foil. Additionally, the α-particle peak should shift to slightly lower energy since the reaction will occur deeper in the target and the emitted α-particle must first escape the target, losing energy in the process. This results in a poorer separation between the two peaks. For a target of $\approx$ 34 keV width, the entire thickness of the target cannot be observed with the ^{17}O(p,α)^{14}N reaction because the α-particle peak should be totally consumed by the increasing low energy noise peak well before the entire thickness of the target could be probed. This is illustrated in Fig. 3.5, where at a bombarding energy of E_p^{lab} = 204 keV there was no longer a clearly separated α-particle peak.

The measured spectra were fit to a function which is the sum of two Gaussians given by,

$$h(x) = a \exp\left[-\left(\frac{x-b}{c}\right)^2\right] + d \exp\left[-\left(\frac{x-f}{g}\right)^2\right]. \tag{3.2}$$

The first Gaussian was selected to fit the tail of the low energy background and the second Gaussian to fit the α-particle peak. The measured spectra were separated into high, middle and low energy

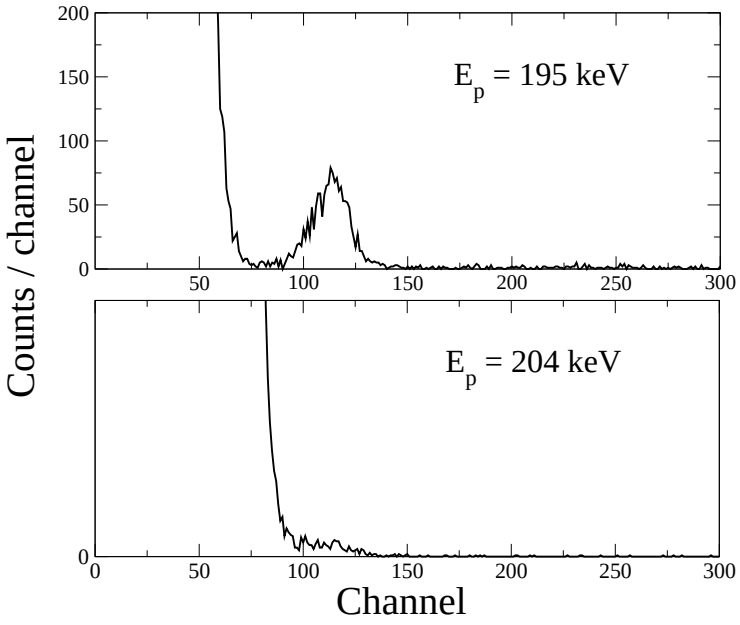

Figure 3.5: Comparison of measured spectra in ^{17}O(p,α)^{14}N measured at E_p^{lab}=195 keV (top panel) and E_p^{lab} = 204 keV (bottom panel). The difference in the α-particle peak heights is the result of variations in accumulated charges on the target for the two runs and poorer resolution at the higher bombarding energy.

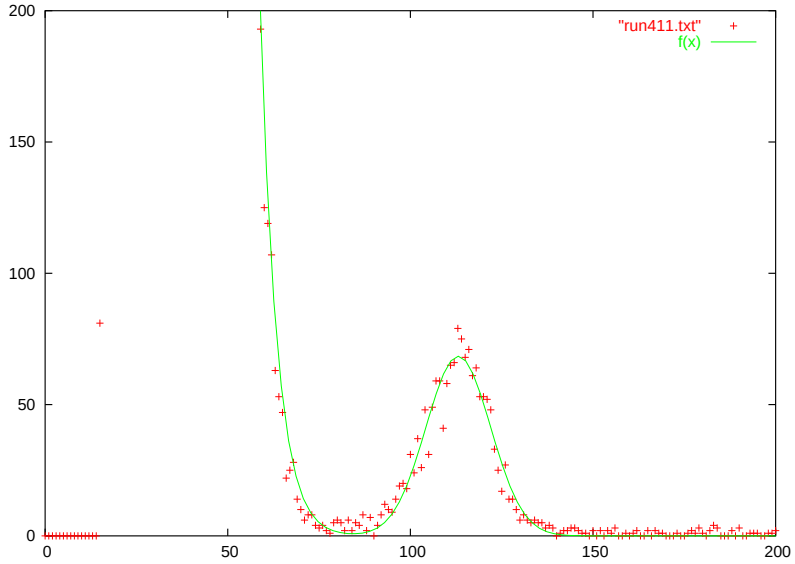

Figure 3.6: Fitted spectrum in ^{17}O(p,α)^{14}N using two Gaussians to describe the function.

groups. A well separated peak was chosen from each group to fix the width of the α-particle peak. This peak width was held constant for the fitting of the other spectra in that group. Recall that as the bombarding energy increases, the position in the target where the reaction is occurring will be deeper. Therefore, there will be more energy straggling at higher energies because the α-particle must escape the target prior to detection. The fixed width for each of the three groups increased as the bombarding energy increased. This width was very important to the determination of the number of counts in a given α-particle peak, N. For the peak described by Eq. 3.2, N is given by

$$N = dg\sqrt{\pi}. \tag{3.3}$$

Since the width of the peak, g, was chosen to be a constant, the uncertainty in the number of counts in the α-particle peak took on a very simple form,

$$\sigma_N = \sigma_d g\sqrt{\pi}. \tag{3.4}$$

Figure 3.6 is an example of the fit used for a specific run. This α-particle peak was found to have a width of 12.5 channels and a maximum of 68.9 $\pm$ 2.0 counts. This spectrum was used to set the width

run	d	g	N	E_{beam} (keV)
406	5.64076 ± 0.5021	12.5	125 ± 11	193
407	12.2888 ± 0.9229	12.5	272 ± 20	195
408	12.924 ± 0.8721	12.5	286 ± 19	196
409	10.1806 ± 0.7452	12.5	226 ± 17	194
410	9.79342 ± 0.6913	12.5	217 ± 15	197
411	68.8999 ± 2.013	12.5	1526 ± 45	195
412	45.2364 ± 1.15	12.5	1002 ± 25	196
413	16.9117 ± 0.994	15.5	465 ± 27	198
414	16.4488 ± 0.7999	15.5	452 ± 22	199
415	19.6223 ± 0.8965	15.5	539 ± 25	200
416	16.5297 ± 0.6411	20.5	601 ± 23	201
417	27.2875 ± 0.8534	20.5	991 ± 31	202
418	11.5922 ± 0.7242	20.5	421 ± 26	203
419	10.569 ± 0.8316	20.5	385 ± 30	204
421	11.8897 ± 0.7885	20.5	432 ± 29	201

Table 3.1: Values for height (d) width (g) and number of counts (N) in each of the α-particle peaks from the runs for ^{17}O(p,α)^{14}N. The parameters d and g are defined by Eq. 3.2. The runs used for setting the various widths of the peaks were 411, 413, and 416 and it is clear that the set width of the peaks increases as our bombarding energy increases.

of the peaks in the first group because it contained the most counts and was still well separated from the low energy background. At an energy of E_p^{lab} = 205 keV the separation was so poor that it was no longer possible to fit the α-particle peak to a reasonable uncertainty. For this reason, the highest bombarding energy used for analysis was E_p^{lab} = 204 keV. This did not probe the entire thickness of our target, but it will be shown in Sec. 3.4 that this range was sufficient for the measurement of the 193 keV resonance strength.

The fitted α-particle peak heights, widths and the associated number of total counts for the ^{17}O(p,α)^{14}N spectra are presented in Tab. 3.1. Fits to the measured spectra from the E_r^{lab} = 151 keV resonance in ^{18}O(p,α)^{15}N were not necessary since the energies of the α-particles emitted from the target were $E_\alpha \approx 3.2$ MeV before the mylar foil and $E_\alpha \approx 2.8$ MeV after passing through the foil. This led to a well separated α-particle peak which is shown in Fig. 3.7 for the E_r^{lab} = 151 keV resonance in ^{18}O(p,α)^{15}N at a bombarding energy of E_p^{lab} = 158 keV.

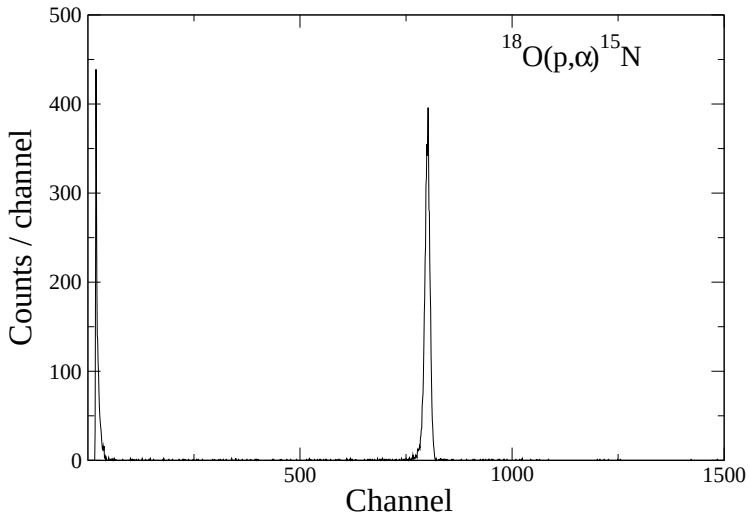

Figure 3.7: Measured spectrum in ^{18}O(p,α)^{15}N at E_p^{lab} = 158 keV. The α-particle peak is well separated from the low energy background. This bombarding energy is positioned on top of the yield curve.

3.4 Resonance Excitation Functions for the ^{17}O and ^{18}O Targets

Having determined the counts in the α-particle peak for each spectrum for the E_r^{lab} = 193 keV resonance in ^{17}O(p,α)^{14}N and the E_r^{lab} = 151 keV resonance in ^{18}O(p,α)^{15}N, the associated excitation functions were constructed and are shown in Fig. 3.8. See Ref. [1] for and in-depth discussion of excitation functions. For these two excitation functions, the relative yield represents counts detected per μC of beam on target.

A fit to both excitation functions was performed to determine the maximum of the yield curve, which is necessary to calculate the resonance strength from a thick target. This fit was performed using a code written by Richard Longland, which takes the function for a thick target yield curve and fits the parameters to the given data, accounting for statistical errors of the individual points. Using this fit, the following maximum yields were found:

$$^{17}O(p,\alpha)^{14}N: \quad Y_{max} = 0.01084 \pm 0.00012$$

$$^{18}O(p,\alpha)^{15}N: \quad Y_{max} = 1.4037 \pm 0.0059$$

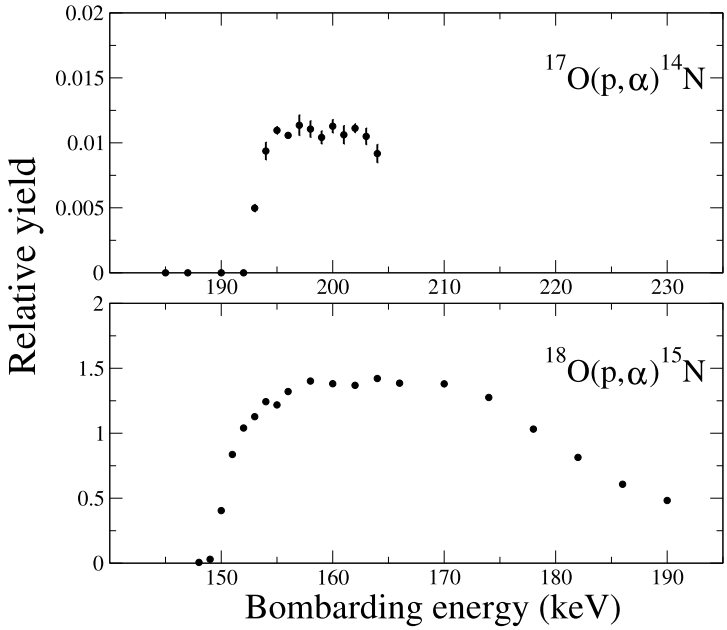

Figure 3.8: Measured excitation functions for the E_r^{lab} = 193 keV resonance in ^{17}O(p,α)^{14}N (top panel) and the E_r^{lab} = 151 keV resonance in ^{18}O(p,α)^{15}N (bottom panel).

The uncertainties listed for the maximum yields are purely statistical. The uncertainty in the integrated charge (BCI) will be accounted for when the calculations of the resonance strengths are carried out explicitly (see section 3.5.3).

It was also possible to determine target widths from the yield curve plots. An ^{18}O target thickness of 34 keV was measured over the bombarding energy range used for the measurement of the E_r^{lab} = 151 keV resonance in ^{18}O(p,α)^{15}N. The ^{17}O yield curve was unable to be used for the determination of target thickness, since the entire thickness of that target could not be probed with the current setup at E_r^{lab} = 193 keV. Recall, that the trace amounts of ^{18}O in the enriched ^{17}O target were used to measure a thickness corresponding to 34 keV for this target at E_r^{lab} = 193 keV.

3.5 Measurement of Relative Resonance Strength

The strength of a resonance may be found experimentally using the following equation [1]:

$$\omega\gamma = \frac{2}{\lambda^2}\epsilon_{eff}\frac{N_\alpha}{N_p BW\eta} \tag{3.5}$$

where λ is the de Broglie wavelength; N_p is the number of incident protons; N_α is the number of resonant α-particles measured on the plateau of the yield curve; W is the angular distribution of outgoing α-particles; B is the branching ratio; ϵ_{eff} is the effective stopping power of the target and η is the detector efficiency. Recall that the resonance strength arises from integrating the Breit-Wigner form of the resonance cross section to find the reaction rate in Eq. 1.19.

Many of the uncertainties that contribute to the direct measurement of a resonance strength are significantly reduced when a relative measurement is made. This experiment employed the same reference resonance that was used in Refs. [19, 21]. Labeling the components of Eq. 3.5 with the resonance energies of the two resonances measured, E_r^{lab} = 151 keV and E_r^{lab} = 193 keV results in:

$$\omega\gamma(151) = \frac{2}{\lambda^2(151)}\epsilon_{eff}(151)\frac{N_\alpha(151)}{N_p(151)B(151)W(151)\eta(151)} \tag{3.6}$$

and

$$\omega\gamma(193) = \frac{2}{\lambda^2(193)}\epsilon_{eff}(193)\frac{N_\alpha(193)}{N_p(193)B(193)W(193)\eta(193)}. \tag{3.7}$$

Taking the ratio of Eqs. 3.6 and 3.7 and solving for $\omega\gamma(193)$ results in the following for the strength of the E_r^{lab} = 193 keV resonance in ^{17}O(p,α)^{14}N:

$$\omega\gamma(193) = \omega\gamma(151)\frac{\lambda^2(151)}{\lambda^2(193)}\frac{\epsilon_{eff}(193)}{\epsilon_{eff}(151)}\frac{N_\alpha(193)}{N_\alpha(151)}\frac{N_p(151)}{N_p(193)}\frac{B(151)}{B(193)}\frac{W(151)}{W(193)}\frac{\eta(151)}{\eta(193)}. \tag{3.8}$$

A detailed discussion of each term and ratio from Eq. 3.8 follows.

3.5.1 The Ratio of de Broglie Wavelegths

The ratio of squares of the de Broglie wavelengths is a straightforward calculation and the uncertainties are small due to the precisely known atomic masses and resonance energies involved. The square of the de Broglie wavelength for a given resonance energy is given numerically by [1]:

$$\lambda_r^2 = 2\left(\frac{m_p + m_t}{m_t}\right)^2 \frac{4.125 \times 10^{-18}}{m_p E_r^{lab}} \text{ cm}^2, \tag{3.9}$$

where m_p and m_t represent the atomic mass of the projectile and target, respectively, and E_r^{lab} is the laboratory resonance energy in eV. Using Eq. 3.9, the ratio of the square of de Broglie wavelengths for the resonances at $E_r^{lab} = 193$ keV in ^{17}O(p,α)^{14}N and $E_r^{lab} = 151$ keV in ^{18}O(p,α)^{15}N can be derived, resulting in:

$$\frac{\lambda_r^2(151)}{\lambda_r^2(193)} = \left(\frac{(m_p + m_{^{18}O})\, m_{^{17}O}}{m_{^{18}O}\,(m_p + m_{^{17}O})}\right)^2 \frac{E_r^{lab}(193)}{E_r^{lab}(151)}. \tag{3.10}$$

The masses in Eq. 3.10 are well know and the values for $E_r^{lab}(193)$ and $E_r^{lab}(151)$ are taken from reference [7]. The values are as follows:

$$\begin{aligned} m_p &= 1.007825 \text{ amu;} \\ m_{^{17}O} &= 16.999131703 \text{ amu;} \\ m_{^{18}O} &= 17.999161 \text{ amu;} \\ E_r^{lab}(193) &= 193.2 \pm 0.9 \text{ keV and} \\ E_r^{lab}(151) &= 150.82 \pm 0.09 \text{ keV} \end{aligned}$$

Inserting these values into Eq. 3.10 gives,

$$\frac{\lambda_r^2(151)}{\lambda_r^2(193)} = 1.2730 \pm 0.0060 \tag{3.11}$$

Extra significant figures are kept, throughout, until the final strength is calculated to avoid rounding errors.

3.5.2 The Ratio of Effective Stopping Powers

Often, one of the major sources of uncertainty in any measurement involving thick targets will be the experimental stopping powers. There is not a consistent procedure in the literature for assigning an uncertainty to these stopping power values. For the purposes of the following calculations, the values for the stopping powers (in laboratory units) will be taken from SRIM [23] with an associated uncertainty of 5%, which is a typical uncertainty used in the literature. The effective stopping power

for the ^{17}O target of protons can be expressed as [7],

$$\epsilon_{eff}^{cm}(^{17}O) = \frac{m_{17}}{m_{17}+m_p}\left(\epsilon(^{17}O) + \frac{N(^{16}O)}{N(^{17}O)}\epsilon(^{16}O) + \frac{N(^{18}O)}{N(^{17}O)}\epsilon(^{18}O) + \frac{N(Ta)}{N(^{17}O)}\epsilon(Ta)\right), \quad (3.12)$$

where ϵ denotes the stopping power of the specific isotope and N is the number density of that nucleus. Since the experimental elemental stopping powers will be assigned errors of 5%, the variations in the stopping power between isotopes will be insignificant. This means the stopping powers for each isotope can be replaced with the SRIM results for the given element. That is, $\epsilon(^{16}O) \approx \epsilon(^{17}O) \approx \epsilon(^{18}O) \approx \epsilon(O)$. This approximation will simplify the form of the effective stopping power for protons of the ^{17}O target, giving:

$$\epsilon_{eff}^{cm}(^{17}O) = \frac{m_{17}}{m_{17}+m_p}\left(\frac{N(O)}{N(^{17}O)}\epsilon(O) + \frac{N(Ta)}{N(^{17}O)}\epsilon(Ta)\right), \quad (3.13)$$

where $N(O) = N(^{16}O) + N(^{17}O) + N(^{18}O)$ is the number density of all oxygen isotopes. Similarly to Eq. 3.13 the effective stopping power for protons of the ^{18}O target will be,

$$\epsilon_{eff}^{cm}(^{18}O) = \frac{m_{18}}{m_{18}+m_p}\left(\frac{N(O)}{N(^{18}O)}\epsilon(O) + \frac{N(Ta)}{N(^{18}O)}\epsilon(Ta)\right). \quad (3.14)$$

The ^{17}O target was anodized using 90.7% enriched ^{17}O water and the ^{18}O target was anodized using 97.5% enriched ^{18}O water. The calculation of the effective stopping power for the enriched ^{17}O target requires the following values:

$$\begin{aligned}
m_p &= 1.007825 \text{ amu;} \\
m_{^{17}O} &= 16.999131703 \text{ amu;} \\
\frac{N(O)}{N(^{17}O)} &= 1.1025 \pm .0221; \\
\frac{N(Ta)}{N(^{17}O)} &= 0.4410 \pm 0.0088; \\
\epsilon(O)_{193keV} &= (13.54 \pm 0.68) \times 10^{-15}\frac{eVcm^2}{atom} \text{ and} \\
\epsilon(Ta)_{193keV} &= (34.57 \pm 1.73) \times 10^{-15}\frac{eVcm^2}{atom.}
\end{aligned}$$

The ratios of number densities listed above come from the atomic abundances given by the distributor of the 90.7% enriched ^{17}O water and the well known stoichiometry of anodized oxygen on tantalum of Ta_2O_5. The associated uncertainties result from assuming a 5% uncertainty on the experimental stopping power values and 2% uncertainty on the ratios of the number densities in the target. Inserting these values into Eq. 3.13 gives,

$$\begin{aligned} \epsilon_{eff}^{cm}(^{17}O) &= 0.94403\left[1.1025\left(13.54\times10^{-15}\right)+0.44101\left(34.57\times10^{-15}\right)\right]\frac{eVcm^2}{atom} \\ \epsilon_{eff}^{cm}(^{17}O) &= (28.48\pm1.08)\times10^{-15}\frac{eVcm^2}{atom}. \end{aligned} \tag{3.15}$$

The same procedure was used to calculate the effective stopping power of the ^{18}O target. Since this target was anodized with highly enriched ^{18}O water, different values for the ratio of isotopic number densities in the target are expected. Also, $\epsilon\,(O)$ and $\epsilon\,(Ta)$ vary for this calculation since the resonance energy is different and the stopping powers are functions of incident proton energy. The following values were used for the calculation of the effective stopping power of the ^{18}O target made with the 97.5% enriched ^{18}O water:

$$\begin{aligned} m_p &= 1.007825 \text{ amu}; \\ m_{^{18}O} &= 17.999161 \text{ amu}; \\ \frac{N(O)}{N(^{18}O)} &= 1.0256\pm0.0205; \\ \frac{N(Ta)}{N(^{18}O)} &= 0.4103\pm0.0082; \end{aligned}$$

$$\begin{aligned} \epsilon(O)_{151keV} &= (14.77\pm0.74)\times10^{-15}\frac{eVcm^2}{atom} \text{ and} \\ \epsilon(Ta)_{151keV} &= (35.44\pm1.77)\times10^{-15}\frac{eVcm^2}{atom}. \end{aligned}$$

The stopping power values were derived from the SRIM [23] and ratios were calculated using both the isotopic abundances quoted by the supplier of the ^{18}O water and the stoichiometry of the

anodized target. The result for the effective stopping power of the ^{18}O target is

$$\epsilon_{eff}^{^{18}O} = (28.12 \pm 1.07) \times 10^{-15} \frac{eVcm^2}{atom}. \tag{3.16}$$

The ratio of Eqs. 3.15 and 3.16 gives the final ratio of effective stopping powers,

$$\begin{aligned} \frac{\epsilon_{eff}^{^{17}O}}{\epsilon_{eff}^{^{18}O}} &= \frac{28.48 \times 10^{-15}}{28.12 \times 10^{-15}} \\ \frac{\epsilon_{eff}^{^{17}O}}{\epsilon_{eff}^{^{18}O}} &= 1.013 \pm 0.054. \end{aligned} \tag{3.17}$$

3.5.3 The Relative Reaction Yields

The calculation of the quantity $\frac{N_{193}^{\alpha}}{N_{151}^{\alpha}} \frac{N_{151}^{p}}{N_{193}^{p}}$ makes use of the fits to the yield curves that were presented in Sec. 3.4. Recall that the fit to the plateau of the yield curve actually gives the ratio $\frac{N^{\alpha}}{BCI}$. The factor for Coulombs per pulse on the integrator used for the BCI counting can then be used to find the value of $\frac{N^{\alpha}}{N^{p}}$ from the fit to the plateau of the yield curve, provided the Coulombs per pulse setting is the same for the measurement of both the E_r^{lab} = 193 keV resonance in ^{17}O(p,α)^{14}N and the E_r^{lab} = 151 keV resonance in ^{18}O(p,α)^{15}N. If this is the case, calculation of the number of protons is unnecessary. The BCI value will suffice since this factor cancels in the multiplication of the two ratios,

$$N_{193}^{p} = BCI_{193} \times \frac{Coulombs}{pulse} factor \times \left(\frac{1 proton}{1.602 \times 10^{-19} Coulombs} \right).$$

Thus, the ratio of protons is given by the ratio of BCI values:

$$\frac{N_{151}^{p}}{N_{193}^{p}} = \frac{BCI_{151}^{p}}{BCI_{193}^{p}}. \tag{3.18}$$

This simplifies the current calculation significantly, since the fits to the measured yield curves have already been performed and evaluated.

$$\begin{aligned} ^{17}O &: \frac{N_{193}^{\alpha}}{BCI_{193}} = 0.010843 \pm 0.0001209 \\ ^{18}O &: \frac{N_{151}^{\alpha}}{BCI_{151}} = 1.4037 \pm 0.0059 \end{aligned}$$

In addition to statistical uncertainties, we assign a 5% uncertainty to the ratio of the current integration, $\frac{BCI_{151}}{BCI_{193}}$. This 5% is added in quadrature with the statistical uncertainty on the statistical fit to yield:

$$\left(\frac{N^{\alpha}_{193}}{N^{\alpha}_{151}}\right)\left(\frac{N^{p}_{151}}{N^{p}_{193}}\right) = 0.00772 \pm 0.00040 \tag{3.19}$$

3.5.4 The Angular Distribution Functions

For the resonance at E_r^{lab} = 151 keV in ^{18}O(p,α)^{15}N, there is an isotropic distribution of outgoing α-particles because the spin of this resonance is J = 1/2. This corresponds to W(θ) = 1, where W(θ) is the angular distribution of outgoing α-particles. The ^{17}O(p,α)^{14}N reaction is not isotropic because of the spins and parities involved, therefore the angle of α-particle detection becomes important. Recall that the current measurement was performed at a single angle, preventing extraction of angular distribution information. Thus, the angular distribution function found by Chafa et al. [19] was used. Their data were fit to a Legendre polynomial, resulting in an angular distribution of

$$W(\theta) = 1 + (0.16 \pm 0.03)P_2(cos\theta), \tag{3.20}$$

where θ is the center of mass angle with respect to the beam direction. There is a small correction coming from the fact that there is an angular acceptance of our detector. This correction is called the attenuation factor and is denoted by Q. This attenuation factor must be included when determining the coefficients of an experimental angular distribution. The angular distribution function will now have the following form [1]:

$$W(\theta) = 1 + (0.16 \pm 0.03)QP_2(cos\theta), \tag{3.21}$$

where

$$Q = \frac{\int_0^{\beta_{max}} P_2(\cos(\beta))\eta(\beta, E)\sin(\beta)d\beta}{\int_0^{\beta_{max}} \eta(\beta, E)\sin(\beta)d\beta}. \tag{3.22}$$

The angle between the detector symmetry axis and the direction of an emitted α-particle is denoted by β [1]. The maximum value of this angle for our running geometry is β_{max} = 5.25°, resulting in an integral with the limits $\int_0^{\beta^{max}=5.25^{\circ}}$. It was shown in Sec. 3.2.2 that the detector has an intrinsic

efficiency of unity, or $\eta(\beta, E) = 1$, which simplifies Eq. 3.22 to give:

$$\begin{aligned} Q &= \frac{\int_0^{5.25} P_2(\cos(\beta))\sin(\beta)d\beta}{\int_0^{5.25}\sin(\beta)d\beta} \\ &= \frac{\int_0^{5.25} \frac{1}{2}[3(\cos\beta)^2\sin\beta - \sin\beta]d\beta}{\int_0^{5.25}\sin(\beta)d\beta} \\ &= \frac{-\frac{1}{2}[(\cos\beta)^3 - \cos\beta]_0^{5.25}}{-[\cos(\beta)]_0^{5.25}} \\ &= 0.9937 \end{aligned} \tag{3.23}$$

Now that the attenuation factor has been calculated, it is possible to find W(θ) for the ^{17}O(p,α)^{14}N measurement. Recall from Sec. 3.2.1 that the beam throughout this experiment was slightly off center. This was seen by looking at the beam on target through the target chamber window. It was estimated that the beam could be up to 0.64 cm off center (or 0.32$\pm$ 0.32 cm). Combined with the 45° angle of the target, this results in a final detection angle of θ_{cm} = 133.6°, which gives:

$$\begin{aligned} W(133.6) &= 1 + (0.16 \pm 0.03)(0.9937)P_2(\cos(133.6)) = 1.0339 \\ &\text{and} \\ \sigma_{W(\theta)} &= (0.03)(0.9937)P_2(\cos(133.6)) = 0.00636 \end{aligned}$$

Therefore, the angular distributions functions are W$^{17O}(\theta)$ = 1.0339 $\pm$ 0.0064 and W$^{18O}(\theta) = 1$.

3.5.5 Relative Detection Efficiencies

Since the reaction rate assumes the center of mass frame, the resonance strength should also be calculated in center of mass units. Thus the measured efficiency of the detector must be transformed to the center of mass frame, which requires a differential solid angle that can be calculated using a kinematics code. For this calculation, the code RKIN was used. The conversion from lab efficiency

θ_{lab}	$^{18}O(p,\alpha) : \left(\frac{d\Omega^{lab}}{d\Omega^{cm}}\right)$	$^{17}O(p,\alpha) : \left(\frac{d\Omega^{lab}}{d\Omega^{cm}}\right)$
130.2	1.0302	1.0649
132.6	1.0317	1.0681
135.0	1.0331	1.0712

Table 3.2: Lab to Center of mass conversion factors for the range of possible detection angles.

to center of mass efficiency is given by :

$$\eta^{cm} = \eta^{lab}\left(\frac{d\Omega^{cm}}{d\Omega^{lab}}\right), \tag{3.24}$$

where η^{cm} and η^{lab} are the detector efficiencies in the center of mass and lab systems, respectively. Since the intrinsic efficiency of these silicon detectors is 1, the lab efficiency is equal to the geometric efficiency. The geometric efficiency is independent of the energy of the incoming particle, which gives a simple relation for the ratio of detector efficiencies:

$$\frac{\eta^{151}}{\eta^{193}} = \frac{\eta^{geometric}\left(\frac{d\Omega^{cm}}{d\Omega^{lab}}\right)^{151}}{\eta^{geometric}\left(\frac{d\Omega^{cm}}{d\Omega^{lab}}\right)^{193}} = \frac{\left(\frac{d\Omega^{lab}}{d\Omega^{cm}}\right)^{193}}{\left(\frac{d\Omega^{lab}}{d\Omega^{cm}}\right)^{151}}, \tag{3.25}$$

where η^{151} and η^{193} refer to the α-particle detection efficiency at proton bombarding energies of E_r^{lab} = 151 and 193 keV, respectively and $\left(\frac{d\Omega^{cm}}{d\Omega^{lab}}\right)$ is a function of detection angle. Recall from Sec. 3.2.1 that there is some uncertainty in the incoming beam angle, resulting in a range of possible detector angles. The beam was off center by up to 0.64 cm corresponding to a lab angle of $132.6^\circ \pm 2.4^\circ$. Tab. 3.2 gives the lab to center of mass correction factors for this range of angles. Thus, the values for the lab to center of mass conversion factor become $\left(\frac{d\Omega^{lab}}{d\Omega^{cm}}\right)^{151} = 1.0317 \pm 0.0015$ and $\left(\frac{d\Omega^{lab}}{d\Omega^{cm}}\right)^{193} = 1.0681 \pm 0.0032$. The ratio of detector efficiencies for the measurements of the E_r^{lab} = 151 keV resonance in ^{18}O(p,α)^{15}N and the E_r^{lab} = 193 keV resonance in ^{17}O(p,α)^{14}N can now be calculated using Eq. 3.25. This gives,

$$\frac{\eta^{151}}{\eta^{193}} = 1.0353 \pm 0.0034. \tag{3.26}$$

3.5.6 The Strength of the E_r^{lab} = 193 keV Resonance in ^{17}O(p,α)^{14}N

Eq. 3.8 and the ratios calculated in Secs. 3.5.1 - 3.5.5 allow for calculation of the 193 keV resonance strength in $^{17}O(p,\alpha)^{14}N$ as shown below:

$$\begin{aligned}
\omega\gamma_{p\alpha}(151) &= (0.167 \pm 0.012)\ \text{eV};\\
\frac{\epsilon_{eff}^{193}}{\epsilon_{eff}^{151}} &= 1.013 \pm 0.054;\\
\frac{\eta_{151}}{\eta_{193}} &= 1.0353 \pm 0.0034;\\
\frac{N_\alpha(193)}{N_\alpha(151)}\frac{N_b(193)}{N_b(151)} &= 0.00772 \pm 0.00040;\\
\left(\frac{\lambda_{151}}{\lambda_{193}}\right)^2 &= 1.2730 \pm 0.0060 \text{ and}\\
W(193) &= 1.0339 \pm 0.0064.
\end{aligned}$$

Inserting these values into Eq. 3.8 gives,

$$\begin{aligned}
\omega\gamma_{p\alpha}(193) &= (0.167)(1.013)(1.2730)(0.00772)(1)(1.0353)\frac{1}{1.0339}\\
\omega\gamma_{p\alpha}(193) &= (1.66 \pm 0.17) \times 10^{-3}\ \text{eV}. \qquad (3.27)
\end{aligned}$$

This result is in agreement with the value from Chafa et al. [19, 21] and a subsequent measurement performed at ORNL [25] using a completely different technique.

3.6 Geant4 Simulations of Silicon Detector Response

In an effort to understand the shape of the α-particle peak seen in the MCA spectra for this experiment, Monte Carlo simulations were performed using a modeling code called Geant4 [26]. The first simulation was straightforward and involved the use of an isotropic distribution of 997 keV α-particles (the energy of the outgoing α-particles from the 193 keV resonance in ^{17}O(p,α)^{14}N) originating from the target position and passing through a mylar foil prior to reaching the detector. The first question was whether there would be any effect on the efficiency of the silicon detector based on the energy of the incoming α-particles and the straggling in the mylar foil. The experimental efficiency was

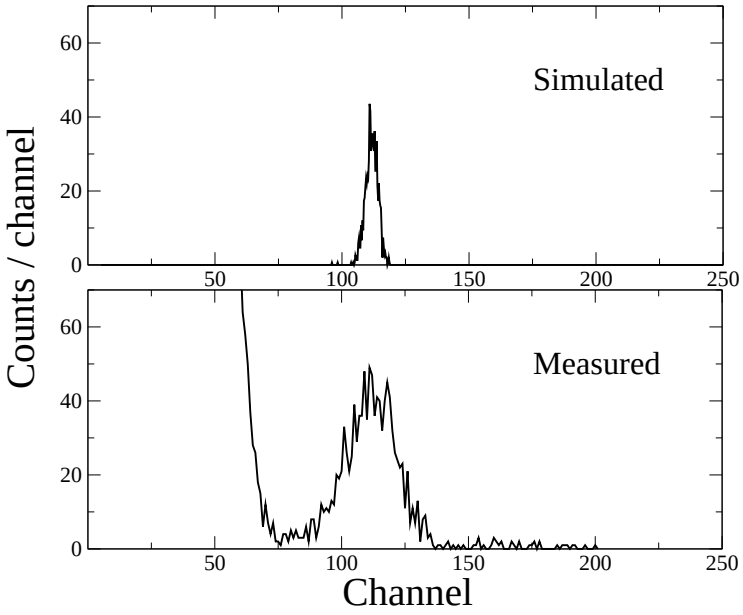

Figure 3.9: Simulated (top) and measured (bottom) α-particle spectrum for the E_r^{lab} = 193 keV resonance in ^{17}O(p,α)^{14}N.

measured using a ^{241}Am source which produces α-particles with an energy of $E_\alpha \approx 5.5$ MeV, while the energy of interest for the α-particles from the E_r^{lab} = 193 keV resonance in ^{17}O(p,α)^{14}N and the the E_r^{lab} = 151 keV resonance in ^{18}O(p,α)^{15}N are $E_\alpha \approx 1.0$ MeV and $E_\alpha \approx 3.2$ MeV respectively. A change in energy was found to affect the detection efficiency by less than 1%.

Figure 3.9 shows a measured spectrum and a simulated run using Geant4 with the assumption of a perfectly uniform 2.0 μm thick mylar foil positioned before the detector. The full width at half maximum of the simulated spectrum gives a resolution of 21 keV, while the width of the measured peak corresponds to a resolution of 87 keV. The simulated spectrum in Fig. 3.9 does not include the intrinsic resolution of the silicon detector measured to be $\approx$ 20 keV using the ^{241}Am source discussed previously.

Further simulations were performed in an effort to understand the discrepancy in resolution observed between the simulated and experimental data. The first consideration was that the detector had an angular acceptance of 5.2°. Calculating the difference in energy of the α-particles incident over this range of angles resulted in a difference of less than 10 keV. This was not sufficient to account for the 87 keV resolution seen in the measured spectrum. Apart from reaction kinematics, the only other

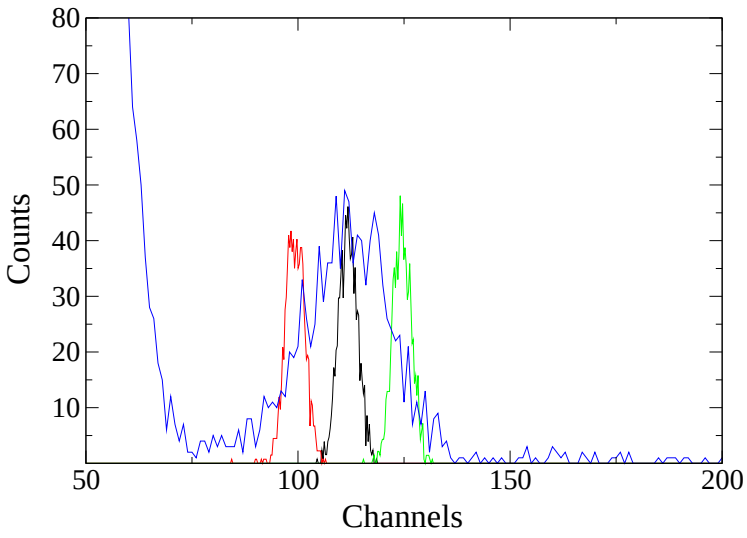

Figure 3.10: Simulated α-particle spectra for the 193 keV resonance in ^{17}O(p,α)^{14}N, for different thicknesses of the mylar foil placed in front of the silicon detector. The wide blue curve is the measured spectrum. The narrower green, black and red spectra correspond to simulations of 1.85, 2.00 and 2.15 μm thick mylar foils, respectively.

explanation for the loss of resolution is an inhomogeneity in the mylar foil used to cover the detector. The uncertainty in mylar foil thickness was measurable by simulating a series of foil thicknesses and matching the resulting spread to the energy width of the measured spectrum.

Figure 3.10 shows the results of the simulations for three different thicknesses of the mylar foil: 1.85, 2.00 and 2.15 μm. The wider underlying blue curve is the measured α-particle peak. The simulations demonstrate that the width of the measured α-particle spectrum may be explained by inhomogeneity of the mylar foil. The range of mylar thickness simulated, 2.00 $\pm$ 0.15 μm, is well within the tolerance quoted by the supplier. This suggests that the uniformity of foil used is extremely important for the measurement of very weak resonances. Simulations confirm that this is the main factor contributing to the resolution of the measured spectra.

The work described in this chapter has been published in Newton et al. [27] to which the reader is referred for further details.

4 Direct Capture in ^{17}O(p,γ)^{18}F

4.1 The Current Landscape

Recall that the peak temperature range of interest for classical novae is T = 0.1 - 0.4 GK. This corresponds to Gamow peaks with positions of E_0 = 103 - 261 keV. The three lowest lying resonances for this reaction are positioned at E_r^{lab} = 70, 193 and 519 keV. The resonance strengths have either been experimentally measured or calculated with experimental parameters. The 193 keV resonance lies in the center of the Gamow peak for classical novae. It is shown, however, in Ref. [7] that the direct capture process provides the dominant contribution to the total reaction rate at these temperatures. This is unusual, since a resonance inside the Gamow window is generally found to be the dominating contributor. Thus, it is crucial to determine the direct capture contribution to the total cross section if the overall reaction rate of ^{17}O(p,γ)^{18}F is to be accurately calculated at nova temperatures.

The only literature data for the direct capture contribution at these energies is shown in Fig. 4.1, which is a reproduction of Fig. 3 from Ref. [7]. The experimental data consist of four points measured by Rolfs [6] and one low-energy point from Chafa et al. [21]. It is argued by Fox et al. [7] and revisited by Chafa et al. [21] that inconsistencies exist with the data presented by Rolfs. The dotted line in Fig. 4.1 is the estimated direct capture S-factor contribution quoted by Rolfs. There are also two resonances located at E_r^{cm} = 557 and 677 keV whose combined contributions are included as the large-dashed curve. The low energy blue point at E_r^{cm} = 180 keV measured by Chafa et al. [21] is a total cross section measurement taken as an off-resonance run at the front edge of the E_r^{cm} = 183 keV resonance. This point is consistent with the direct capture curve of Rolfs. This is not surprising, however, since the blue point has error bars of $\approx$ 50%. Fox et al. [7] have argued that it is unclear if the Rolfs' data have been corrected for the existence of the E_r^{cm} = 557 and 677 keV resonances, since because of the tails of these resonances, he performed the majority of his cross section measurements

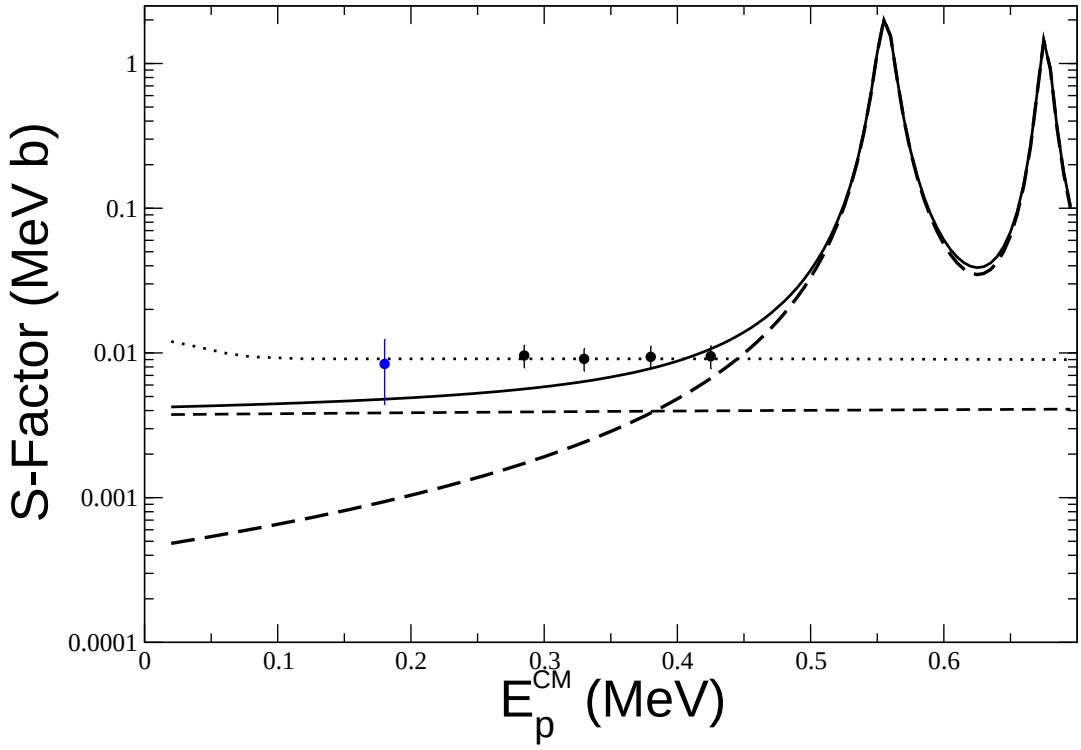

Figure 4.1: The current literature direct capture S-factor data. The black points are from reference [6] with their associated 18% uncertainty. The blue point is taken from reference [21]. The large-dashed curve is the contribution to the total S-factor from the broad resonances at E_r^{cm} = 557 and 677 keV. The small-dashed (flat) curve is the direct capture contribution calculated in reference [7]. The solid black curve is the sum of the small-dashed curve and the large-dashed curve.

at higher energies. Chafa et al. [21] also argue that Rolfs' data are assumed to be totally dominated by the direct capture process. Reference [7] suggests that the energy dependence of the direct capture curve presented by Rolfs is inconsistent with the presence of these resonances. In addition, the low energy upturn of the direct capture of Rolfs could not be reproduced by Fox et al. [7] using either a square-well or Woods-Saxon potential for the bound state wave function. In Fig. 11 from Ref. [6], the measured total cross section for the decay of E_x = 937 keV level to the ground state of ^{18}F is shown. Included in this plot is a solid line that is referred to as the prediction of the direct capture model. This curve goes right through the four lowest energy data points which are the same points included in Fig. 4.1. For these reasons, the direct capture S-factor curve from Ref. [6] was disregarded in Fox's calculation of an S-factor prediction. This calculation uses the literature values of experimentally measured spectroscopic factors. The formalism for such calculations is presented in Chap. 1 (see Eq. 1.31) and Ref. [7]. This calculation is not purely theoretical since it uses experimentally measured spectroscopic factors. The resulting direct capture contribution is included as the dashed line in Fig. 4.1 and amounts to a factor of $\approx$ 2.5 less than the direct capture contribution of Rolfs. Since there is a large discrepancy between these values and the S-factor contribution to the total reaction rate dominates near these nova energies, a new independent measurement of the nonresonant S-factor at $E_{cm} < 500$ keV is required.

4.2 Experimental Setup

Measurement of the total cross section of ^{17}O(p,γ)^{18}F was performed using the LENA 1 MV JN model Van de Graaff accelerator to supply proton beams of up to 120 μA on target. The proton energies ranged from 250 - 530 keV. The bombarding energy was calibrated using six resonances in three different reactions. These are provided in Tab. 4.1. The data for these resonance energies were fit to determine a calibration for the analyzing magnet, which regulates the terminal voltage of the accelerator and thus, the beam energy. A linear fit of $E = 6208B^2 - 1.65$ with a residual standard error of 0.45 keV was determined for the magnet calibration. In addition, six independent measurements of the 519 keV resonance in ^{17}O(p,γ)^{18}F were analyzed. These resulted in a standard deviation of 0.58 keV on the measured resonance energies. Statistical uncertainties on these points

Reaction	E_{res} (keV)
^{27}Al(p,γ)	
	326.97 $\pm$ 0.05
	405.44 $\pm$ 0.10
^{26}Mg(p,γ)	
	292.06 $\pm$ 0.09
	338.4 $\pm$ 0.1
	453.8 $\pm$ 0.1
^{18}O(p,γ)	
	150.82 $\pm$ 0.09

Table 4.1: Narrow resonances used to calibrate the analyzing magnet and determine the energy resolution of the model JN proton beam.

were $\approx$ 0.1 keV. Thus the final uncertainty in laboratory bombarding energy is found by summing the 0.45 keV calibration uncertainty in quadrature with the 0.1 keV statistical uncertainty. This gives a total uncertainty in bombarding energy of 0.46 keV. The measured beam widths associated with these measurements are presented in Tab. 4.2. Of note, the first measurements of the ^{17}O target resulted in small beam width values that increased as the accumulated charge on target was increased, finally reaching a value consistent with those measured for the ^{18}O targets. The measured stoichiometry of the target region did not vary over the experiment, however, which will be discussed in Sec. 4.2.3. A "zero degree" target chamber was used, which allowed for a very close geometry between the target and suppression electrode, since the chamber is simply a cap on the end of the beam line. The suppression electrode, described in Chap. 3, and the target chamber formed a Faraday cup for beam integration and a water chamber was located behind the target backing for cooling purposes.

4.2.1 The Detection System

No interference exists between the E_r^{lab} = 557 and 677 keV resonance contributions since they have different J^π values of 3^+ and 2^+, respectively. In addition, the resonances do not interfere with any of the main direct capture transitions because they have different initial orbital angular momenta. All major direct capture transitions have angular distributions of the form 1 + $a_2 P_2\,(cos\theta)$ and interference effects involving the major primary transitions will produce nonzero anisotropies proportional to $P_2\,(cos\theta)$ [28, 6]. A detection angle of 55° was selected, since $P_2\,(cos\theta)$ = 0 at θ = 55° and neither of

Data used for the analyzing magnet calibration			
Target	Reaction	E_{Lab}^{res} (keV)	Beam Width (keV)
^{26}Mg #5	^{26}Mg(p,γ)^{27}Al	292.1	2.5
^{26}Mg #5	^{26}Mg(p,γ)^{27}Al	338.4	2.5
^{26}Mg #5	^{26}Mg(p,γ)^{27}Al	453.8	2.5
^{27}Al #5	^{27}Al(p,γ)^{28}Si	327.0	2.8
^{27}Al #5	^{27}Al(p,γ)^{28}Si	405.4	3.1
^{18}O	^{18}O(p,γ)^{19}F	150.8	4.3
Data taken with oxygen targets			
Target	Reaction	E_{Lab}^{res} (keV)	Beam Width (keV)
^{18}O #2	^{18}O(p,γ)^{19}F	150.82	
Yield Curve 2			3.28 ± 0.31
Yield Curve 3			3.28 ± 0.27
^{17}O #JN2	^{17}O(p,γ)^{18}F	518.9	
Yield Curve 1			1.63 ± 0.15
Yield Curve 2			1.53 ± 0.03
Yield Curve 4			1.67 ± 0.11
Yield Curve 5			1.59 ± 0.11
Yield Curve 14			4.29 ± 0.20
Yield Curve 15			4.21 ± 0.14

Table 4.2: Measured beam spreads for several different targets and resonances analyzed with the JN accelerator.

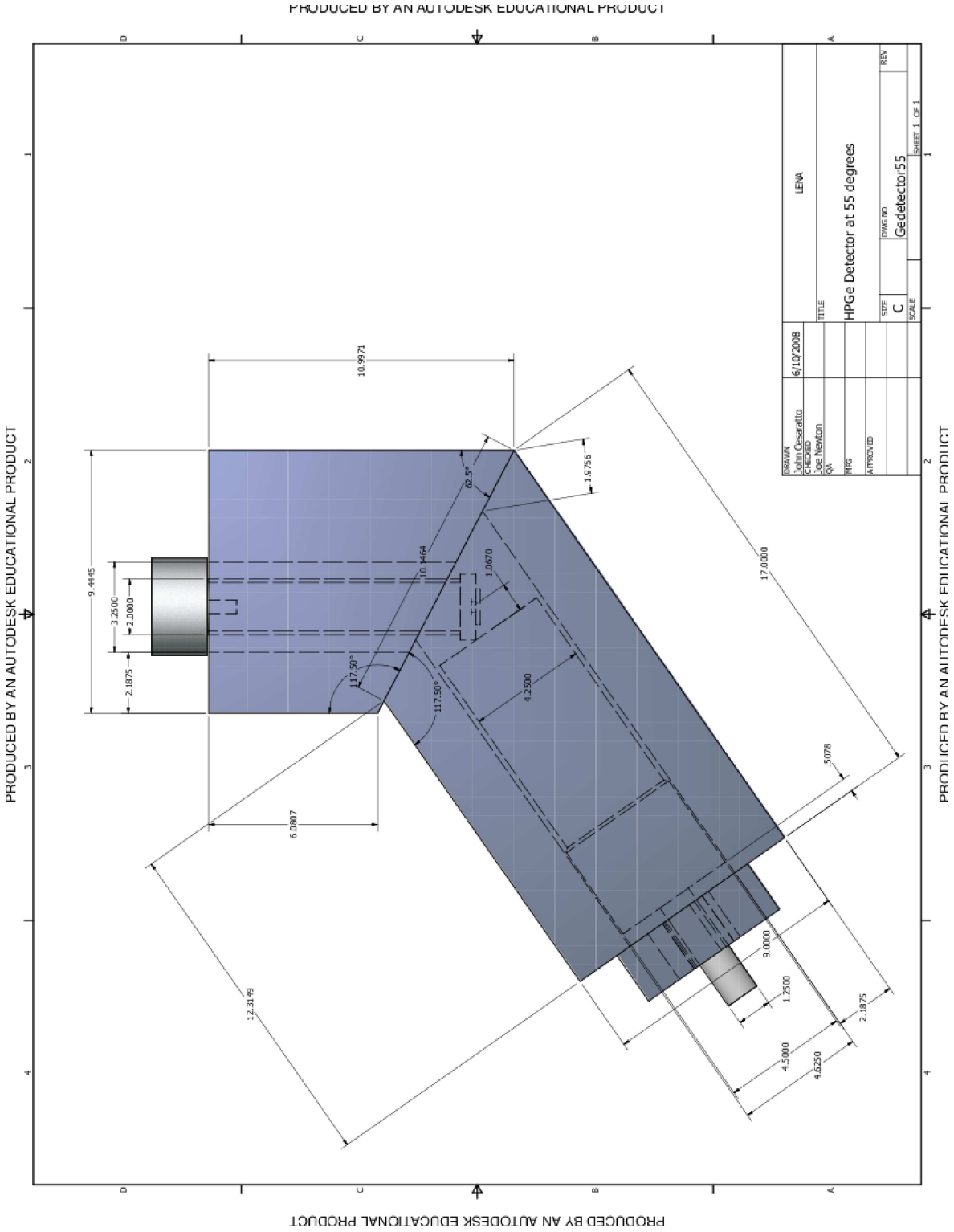

Figure 4.2: Shop drawing of the 5 cm lead shield and LENA HPGe detector in running geometry. The drawing is complements of Johnny Cesaratto.

these interference terms will affect this measurement at this detection angle. There may, however, be more complicated anisotropies produced by the weaker direct capture transitions. The fragmentation of these transitions, along with the close proximity of the detector to the target, should make these effects negligible. The LENA HPGe detector was placed at an angle of 55° and a distance of 3.6 cm from the center of the detector face to the center of the target. The count rates expected for this experiment allowed for a singles germanium measurement provided that the detector was covered with 5 cm of passive lead shielding. Figure 4.2 is a schematic of the lead shield designed for this project. The data were obtained using the acquisition system JAM. The electronics required only one energy signal and one timing gate. An unshielded detector background rate of 7863 $\frac{counts}{minute}$ between E_γ = 600 keV and 3 MeV was seen in the singles Ge spectrum. The detector background count rate was reduced to 165 $\frac{counts}{minute}$ when employing the lead shield, corresponding to a factor of 47.7 reduction in background.

4.2.2 Detector Efficiency

The γ-ray detection efficiency in the running geometry was measured using three radioactive sources and the ^{14}N(p,γ)^{15}O reaction, and was simulated using the Monte Carlo code Geant4 [26]. Two types of detection efficiencies were evaluated. Peak efficiency is the probability of detecting the full energy of a γ-ray emitted from a source. Total efficiency is the probability of detecting a nonzero energy of an emitted γ-ray. Combining the simulations and measurements, the peak and total efficiencies as a function of γ-ray energy were constructed. The sum-peak method for a ^{60}Co source described in Ref. [29] was employed. The advantage of this method is that the source activity cancels out of the final equations and the measurement precision is determined solely by counting statistics.

The peak efficiency of detecting the E_γ = 1173 keV γ ray, $\eta^p_{\gamma 1173}$, becomes

$$\eta^p_{\gamma 1173} = \frac{1}{W(\theta)} \sqrt{\frac{N_{\gamma 1173} N^2_{\gamma 2505}}{N_{total} N_{\gamma 1332} N_{\gamma 2505} + N_{\gamma 1173} N^2_{\gamma 1332}}}. \tag{4.1}$$

The number of counts in the E_γ = 1173 and 1332 keV full energy peaks of the ^{60}Co spectrum are given by $N_{\gamma 1173}$ and $N_{\gamma 1332}$, respectively. The number of counts in the full energy sum peak located at E_γ = 2505 keV is denoted by $N_{\gamma 2505}$ and the total number of room background subtracted counts

$N_{\gamma 1173}$	$N_{\gamma 1332}$	$N_{\gamma 2505}$	N_{total}	W(θ)
112374 ± 349	105990 ± 330	2124 ± 47	750690 ± 866	1.0494
$\eta^p_{\gamma 1173}$		$\eta^p_{\gamma 1332}$		η^t_{1332}
0.01744 ± 0.00031		0.01644 ± 0.00029		0.0829 ± 0.0012

Table 4.3: Measured efficiencies for E_γ = 1173 and 1332 keV lines from a ^{60}Co source.

due to the ^{60}Co source from E_γ = 0 - 2505 keV is denoted by N_{total}. The measured γ-ray spectra were extrapolated to zero pulse height for the determination of N_{total} to account for the low energy thresholds of the electronics. Similarly, for the E_γ = 1332 keV γ-ray the peak efficiency is

$$\eta^p_{\gamma 1332} = \frac{1}{W(\theta)} \sqrt{\frac{N_{\gamma 1332} N^2_{\gamma 2505}}{N_{total} N_{\gamma 1173} N_{\gamma 2505} + N_{\gamma 1332} N^2_{\gamma 1173}}}. \tag{4.2}$$

The average total efficiency due to both the E_γ = 1173 and 1332 keV lines is given by

$$\eta^t_{\gamma 1332} = \frac{1}{W(\theta)} - \frac{1}{W(\theta)} \sqrt{\frac{N_{\gamma 1173} N_{\gamma 1332}}{N_{total} N_{\gamma 2505} + N_{\gamma 1173} N_{\gamma 1332}}}. \tag{4.3}$$

The angular correlation coefficient, $W(\theta)$, is a function of the distance between the detector and target, the geometry of the HPGe crystal and the angular distribution of the radiation from the source [1, 29]. The angular correlation attenuation factor, described in Sec. 3.5.4, was calculated using a code written by Richard Longland that performs an analytical integration of the angular correlation between the two emitted γ-rays over the solid angle covered by the detector. Using Eqs. 4.1, 4.2 and 4.3, along with the measured count rates listed in Tab. 4.3, the peak and total efficiencies of an E_γ = 1173 and 1332 keV γ-ray were calculated. The results are presented in Tab. 4.3. These measured efficiencies were then used to normalize all other measured and simulated efficiencies.

The next step was to use ^{56}Co and ^{152}Eu sources to construct a relative efficiency curve. Since the ^{56}Co source was weak it could be placed in the target position with the HPGe detector in the normal running position. No pile-up was observed in the detector. This close geometry required the application of coincidence summing corrections to the data. Coincidence summing occurs when two or more γ-rays from the same decaying nucleus interact with the detector. This is more likely to occur at high γ-ray detection efficiencies. The effects of coincidence summing will depend on the

total and peak detection efficiencies and can be corrected for if the branching ratios of each decay are known. These corrections were performed using a C program, **sump.c**, written by Richard Longland, following the matrix formalism presented in Ref. [30]. The summing corrected data points were then fit by an R code and normalized to the measured ^{60}Co efficiencies. The ^{152}Eu source was very strong, which required positioning the detector at a distance of 30 cm from the source, to reduce the effects of pile up. Summing corrections were, therefore, negligible and the detection efficiencies were simply scaled to the normalized ^{56}Co data using the E_γ = 1112 and 1299 keV lines from ^{152}Eu. This produced a normalized efficiency curve for E_γ = 120 - 3600 keV.

The higher energy efficiencies were measured using the E_r^{lab} = 278 keV resonance in ^{14}N(p,γ)^{15}O. This reaction produces decays ranging in energy from E_γ = 763 - 7556 keV and spans the entire range of energies needed for measurement of the direct capture component in ^{17}O(p,γ)^{18}F at $E_p^{lab} \leq$ 500 keV. These data were summing corrected and normalized using the normalized ^{56}Co fit and the E_γ = 1380 and 2373 keV lines. The result is a data set of measured efficiencies ranging from E_γ = 120 keV - 7.56 MeV.

The running geometry was then simulated in Geant4 and the peak and total efficiencies were estimated. The resulting peak and total efficiencies were normalized to the measured E_γ = 1173 and 1332 keV efficiencies. Figure 4.3 displays the normalized Geant4 peak efficiency simulations, the measured efficiencies from ^{56}Co, ^{152}Eu and the ^{14}N(p,γ)^{15}O resonance data. The simulated efficiencies correspond well with the experimental data with the exception of efficiencies measured at $E_\gamma < 400$ keV. This suggests that either the material thicknesses modeled in Geant4 are incorrect, or the actual detector geometry is incorrectly modeled. The ^{152}Eu source data were collected at a greater distance from source to detector than the running geometry. The first test was then to adjust the detector position in the Geant4 simulation and compare the simulated and measured efficiencies at $E_\gamma < 400$ keV. Simulations for detector to target distances of 28 and 33 cm were normalized using the same method as the simulations of the running geometry. Figure 4.4 compares the results of these simulations to the measured efficiencies from ^{152}Eu. Simulating the detector at a greater distance from the source produces efficiencies that more closely correspond with the measured efficiencies than the simulations of the original running geometry. This suggests that the original discrepancy between the running geometry simulations and the measured efficiencies at $E_\gamma < 400$ keV can be explained by a large source to

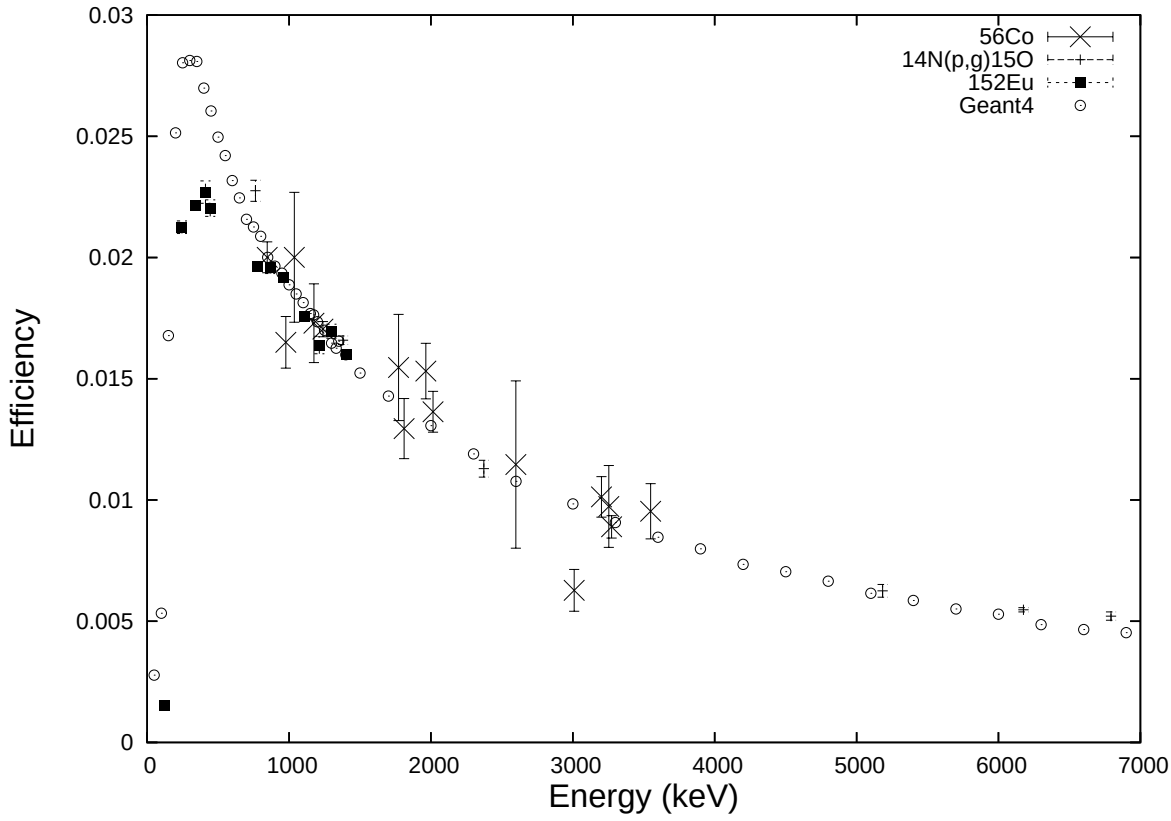

Figure 4.3: Peak efficiency measurements in the 55° detection geometry compared to a normalized Geant4 simulation.

detector distance for the ^{152}Eu data. Also, the major peak of interest in the ^{17}O(p,γ)^{18}F direct capture measurement will be the decay of the first excited state to the ground state (E$_\gamma$ = 937 keV). At this energy the measured and simulated efficiencies are in agreement.

4.2.3 Targets

The oxygen targets used for this experiment were made by anodization of etched tantalum backings with isotopically enriched water. This process is described in App. A.2. The ^{18}O target was anodized with water enriched to 97.5% in ^{18}O and is the same target used as the reference for the (p,α) resonance strength measurements described in Chap. 3. A representative yield curve of the 151 keV resonance in ^{18}O(p,γ)^{19}F is shown in Fig. 4.5. The coefficients listed were found by fitting the yield curve using an R code written by Richard Longland. At E$_p^{lab}$ = 151 keV the target thickness was

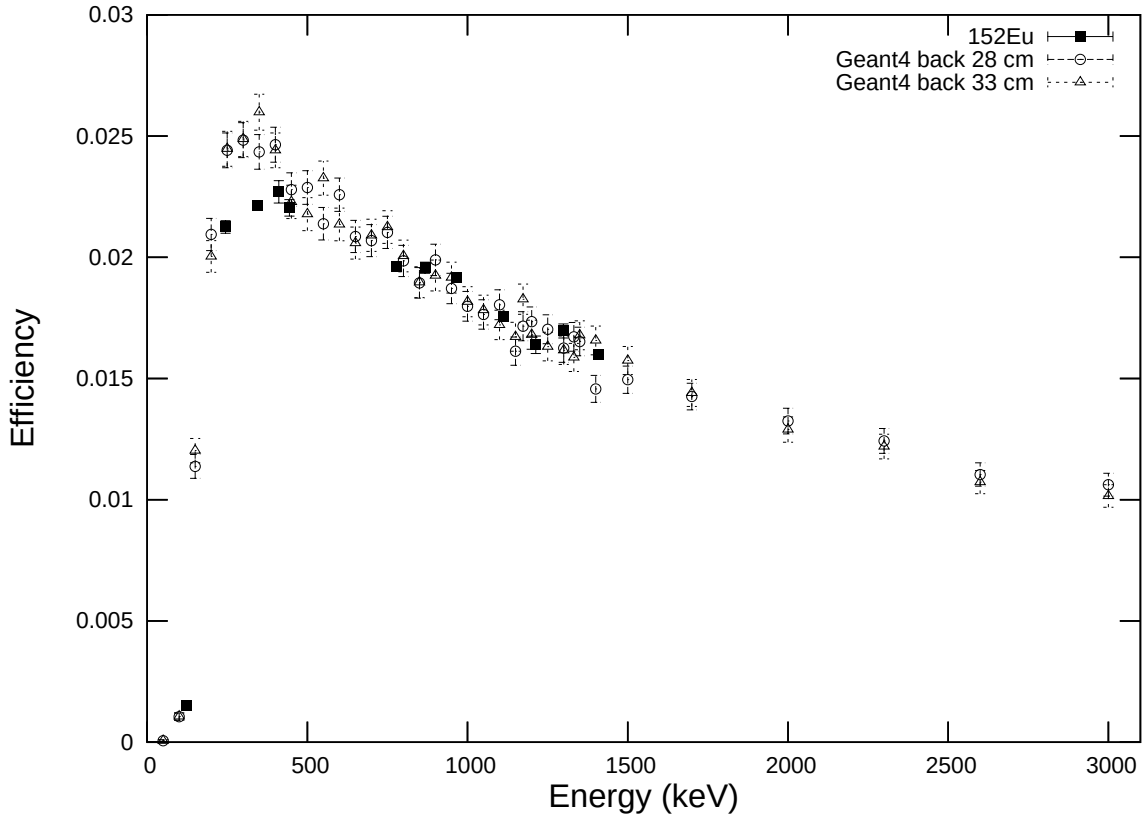

Figure 4.4: Comparison of simulated 55° detection geometry efficiency with that of a ^{152}Eu source. The two Geant4 curves represent detector to target distances of 28 and 33 cm.

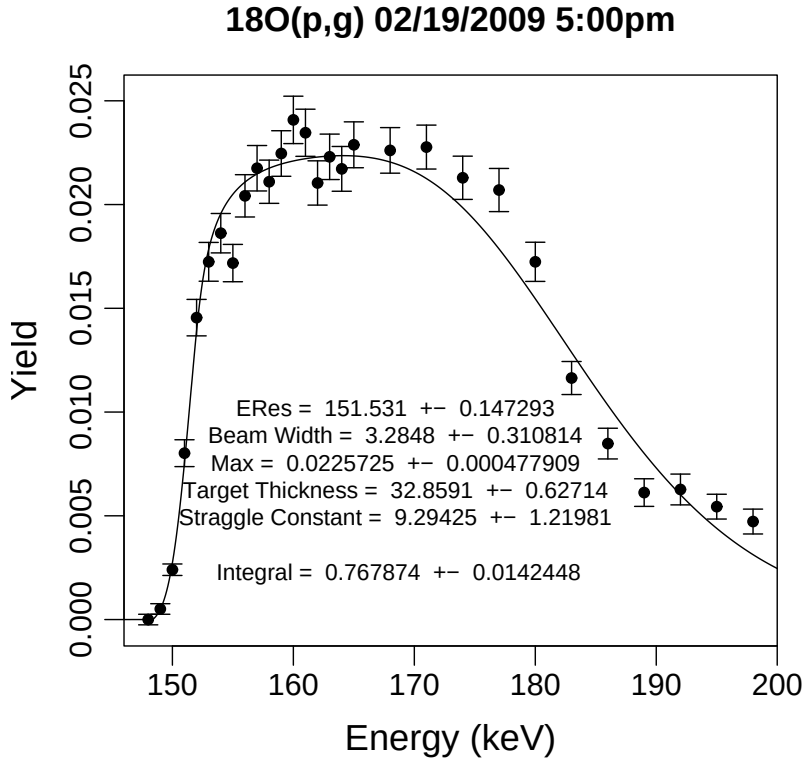

Figure 4.5: Sample yield curve of the E_r^{lab} = 151 keV resonance in ^{18}O(p,γ)^{19}F using the enriched ^{18}O target. Fit parameters were calculated using an R code written by Richard Longland.

33 keV. The reported literature value for this resonance strength, $\omega\gamma$ = (9.7 $\pm$ 0.5)$\times 10^{-4}$ eV [1], was reproduced after summing corrections, resulting in a value of $\omega\gamma$ = (9.3 $\pm$ 1.1)$\times 10^{-4}$ eV.

A new ^{17}O target was prepared for this experiment using water enriched to 91.2% in ^{17}O and an anodization voltage of 30 V. A representative yield curve of the E_p^{lab} = 519 keV resonance in ^{17}O(p,γ)^{18}F is provided in Fig. 4.6. Multiple yield curves were taken for this resonance and the target thickness was consistently found to be $\approx$ 4 - 5 keV at E_p^{lab} = 519 keV. Figure 4.7 shows the variation of target thickness over the accumulated charge on target for this experiment. The red points were not used when generating the linear fit to these data. These points varied significantly more than the black points and were collected with an unstable beam at E_p^{lab} = 519 keV. Calculation of the strength of the E_r^{lab} = 519 keV resonance, performed using the summing corrected data from an early yield curve, resulted in $\omega\gamma$ = 0.0137 $\pm$ 0.0022 eV, which is in agreement with the literature [7]. Results of these

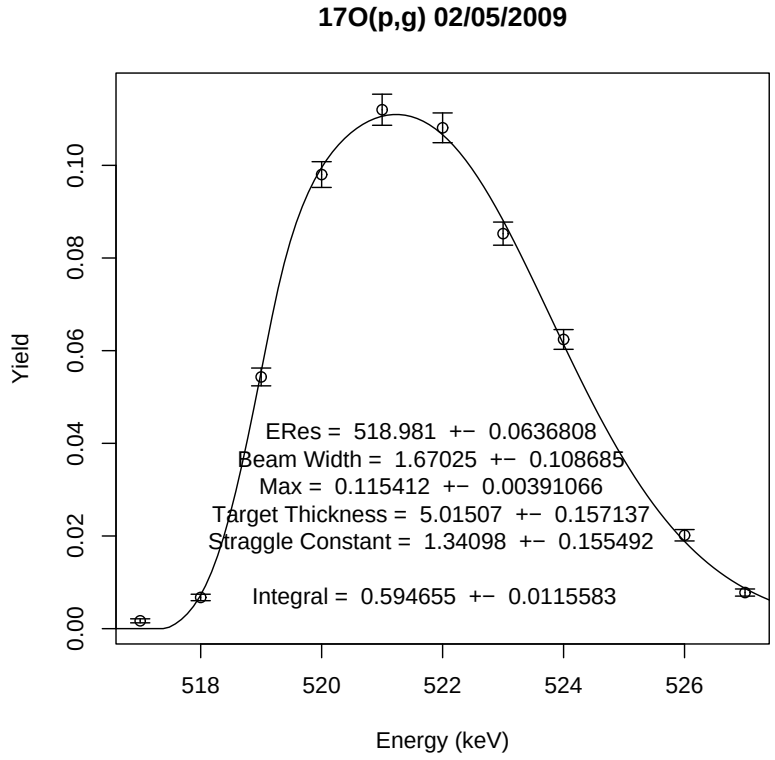

Figure 4.6: Sample yield curve of the E_r^{cm} = 519 keV resonance in ^{17}O(p,γ)^{18}F using the enriched ^{17}O target. Fit parameters were calculated using an R code written by Richard Longland.

target tests also revealed a constant target stoichiometry. Thus it was determined to be a stable target and for the remainder of this chapter will be the ^{17}O target of reference.

4.3 Data Analysis and Results

4.3.1 Measured HPGe γ-Ray Spectra

Data were collected at six different bombarding energies. The accumulated charge and run times are presented in Tab. 4.4. Two types of γ-rays were analyzed in this experiment. "Primary γ-rays" are either the first decay of the excited ^{18}F nucleus in a resonant capture or the γ-ray that is emitted along with the direct nonresonant capture of the incoming proton into a final bound state of ^{17}O + p.

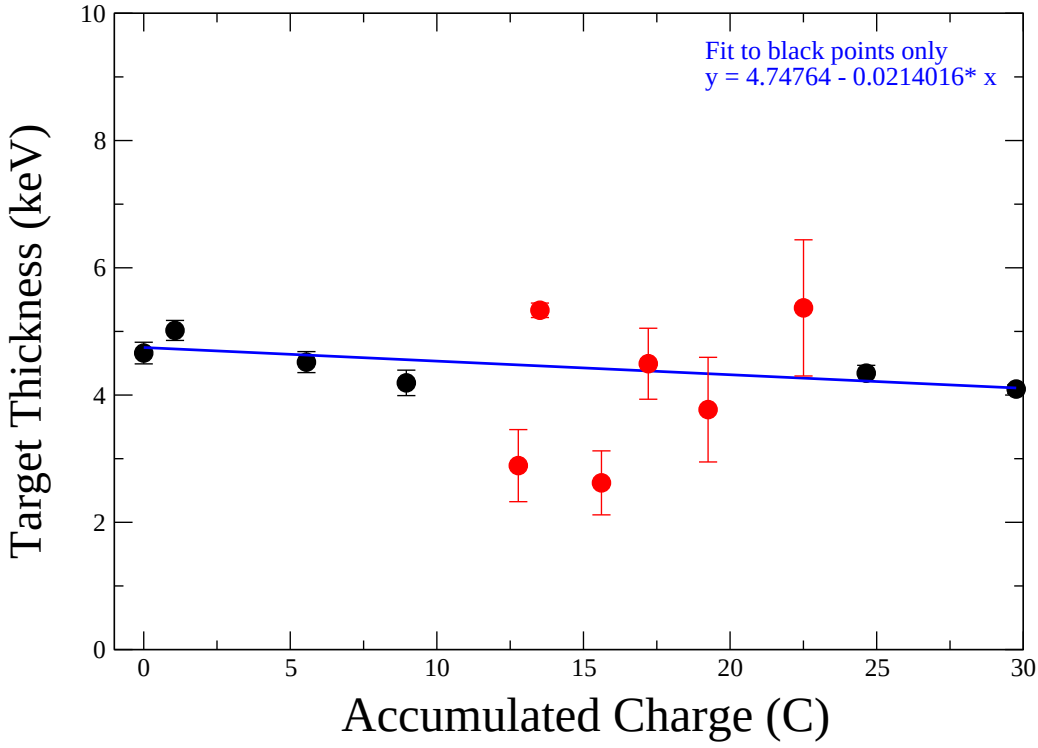

Figure 4.7: Measured ^{17}O target thickness at E_r^{lab} = 519 keV as a function of accumulated BCI on target performed at regular intervals over the course of the ^{17}O(p,γ)^{18}F direct capture cross section measurement.

In either case, the resulting energy for a primary γ-ray is

$$E_\gamma = Q + E_p^{cm} - E_x, \tag{4.4}$$

where Q = 5606.5 is the Q-value of ^{17}O(p,γ)^{18}F; E_p^{cm} is the proton bombarding energy in the center of mass system and E_x is the excitation energy of the level of capture in ^{18}F. "Secondary γ-rays" are the subsequent decays of the ^{18}F after the primary decay of the nucleus. The resulting energy for a secondary γ-ray is

$$E_\gamma = E_{x_i} - E_{x_f}, \tag{4.5}$$

where E_{x_i} and E_{x_f} are the excitation energies of the initial and final levels in the decay of the ^{18}F nucleus, respectively.

Sample spectra for bombarding energies of E_p^{lab} = 400, 325 and 275 keV are shown in Fig. 4.8. Peaks corresponding to decays in ^{18}F resulting from ^{17}O(p,γ)^{18}F are shown in red. The secondary decays are labeled with the excitation energies of the initial and final states. The primary decays are labeled with R/DC (for "resonant" or "direct capture") and the excitation energy of the final level of capture. Peaks corresponding to decays from the ^{12}C(p,γ)^{13}N reaction are also included in this plot. Carbon and fluorine were the major contaminants in the anodized targets. See Ref. [31] for an extensive discussion of contamination of these tantalum backings, where it was found that resistively heating them is critical for minimizing fluorine and carbon contamination. Room background peaks are marked with B and were easily identified when comparing spectra from successive runs with a room background spectrum. A peak from ^{23}Na(p,γ)^{24}Mg was only visible in the E_p^{lab} = 325 keV spectrum. This reaction has a resonance near 325 keV and the peak corresponds to the decay to the ground state of the E_x = 1368 keV state in ^{24}Mg. The data presented in Fig. 4.8 demonstrate a clear and rapid reduction in the number of visible ^{17}O(p,γ)^{18}F reaction decays with decreasing bombarding energy. In addition, as seen in the E_γ = 937 keV peak, a sharp decline in cross section is observed with decreasing bombarding energy.

A high γ-ray energy regime of the Ge spectra collected for E_p^{lab} = 400, 450 and 500 keV is presented in Fig. 4.9. The three background peaks correspond to the decay of the E_x = 6.13 MeV state in ^{16}O, which is populated by the ^{19}F(p,$\alpha\gamma$)^{16}O reaction. The marked peaks correspond to

E_p^{lab} (keV)	Q_{accum} (μC)	Run Time (hours)
500	3211991	14.6
450	3617098	14.0
400	4235046	14.0
325	3780708	15.1
300	4093731	14.1
275	5001844	14.1

Table 4.4: Integrated charge on target and total run times for bombarding energies of 275 - 500 keV.

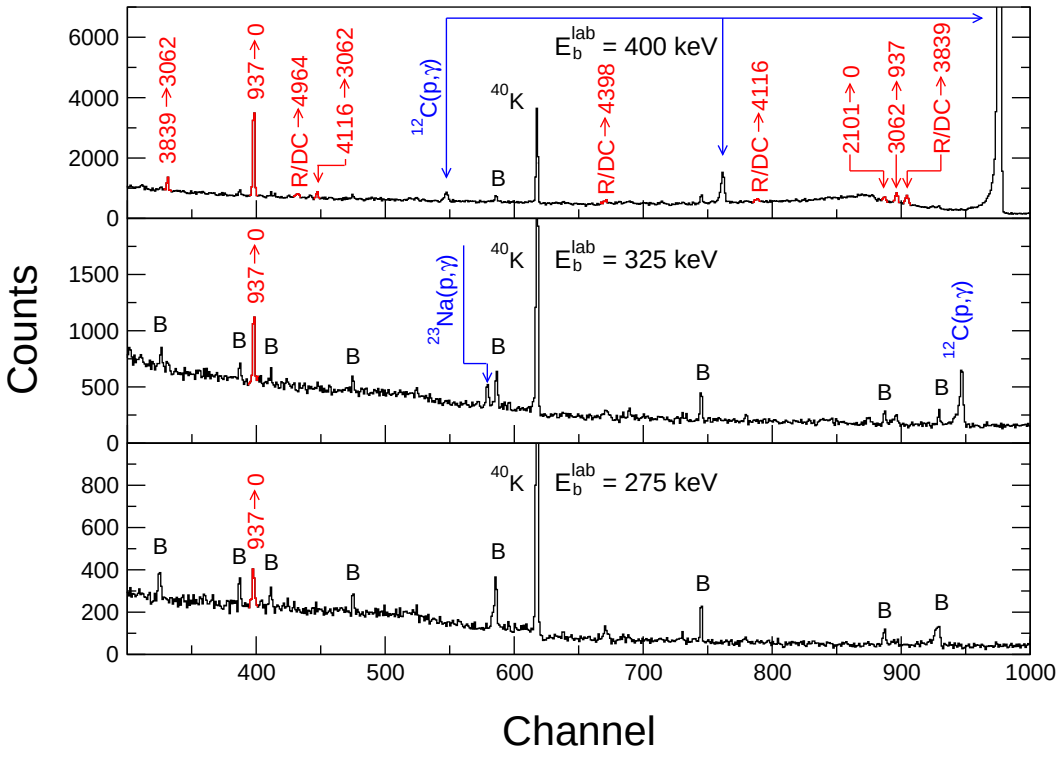

Figure 4.8: Sample γ-ray spectra for bombarding energies of E_p^{lab} = 400 keV (top), 325 keV (middle) and 275 keV (bottom); γ-ray transitions are marked in red; R/DC refers to resonant or direct capture; B corresponds to room background.

the full energy peak at E_γ = 6.13 MeV and the associated single and double escape peaks. Strong resonances exist in ^{19}F(p,$\alpha\gamma$)^{16}O at E_r^{cm} = 459.5 and 323.3 keV, which may both contribute to this beam induced background. The existence of these resonances and the differences in accumulated charge on target for the three runs account for the relative intensities of the fluorine contamination background peaks at E_p^{lab} = 500, 450 and 400 keV. These beam-induced background peaks presented a significant obstacle to this experiment as a result of their effect on the resolution of one of the major primary transition peaks in ^{17}O(p,γ)^{18}F. The capture into the first excited state at E_x = 937 keV is marked in red and is visible in the E_p^{lab} = 400 and 500 keV spectra but has completely merged with the double escape peak in the E_p^{lab} = 450 keV spectrum. The capture into the E_x = 937 keV level is one of the strongest transitions for each of the measured bombarding energies. This missing contribution can be estimated by interpolation of the five observed contributions and this process will be discussed later in this chapter.

Calculation of the total S-factor for the ^{17}O(p,γ)^{18}F reaction requires determination of the total number of proton captures. This can be accomplished by two methods. The first method is counting the total number of primary captures, since each reaction must begin with a capture prior to ^{18}F decay. Alternatively, the secondary transitions ending in the ground state may be counted, since each capture eventually decays to the ground state of ^{18}F. Our calculations have shown that the cross section of the primary capture to the ground state in ^{18}F is insignificant and can be disregarded for the current discussion.

Table 4.5 contains a list of the number of observed secondary decays to the ground state in ^{18}F for each bombarding energy evaluated. The detection efficiency for each secondary γ-ray energy is also included. The E_x = 2101 keV to ground state transition in the E_p^{lab} = 450 keV spectrum was indistinguishable from the background associated with ^{12}C(p,γ)^{13}N. The strongest transition visible at each measured proton energy is the decay of the first excited state, E_x = 937 keV, to the ground state. This represents the only peak seen at the lowest bombarding energy, E_p^{lab} = 275 keV, and the only peak with useful statistics at E_p^{lab} = 300 and 325 keV.

Table 4.6 contains a list of the number of primary transitions detected in each of the six runs. The use of primary decays for determination of the total number of reactions proved more difficult than using the secondaries for two reasons. First, the branching through the primaries was much more

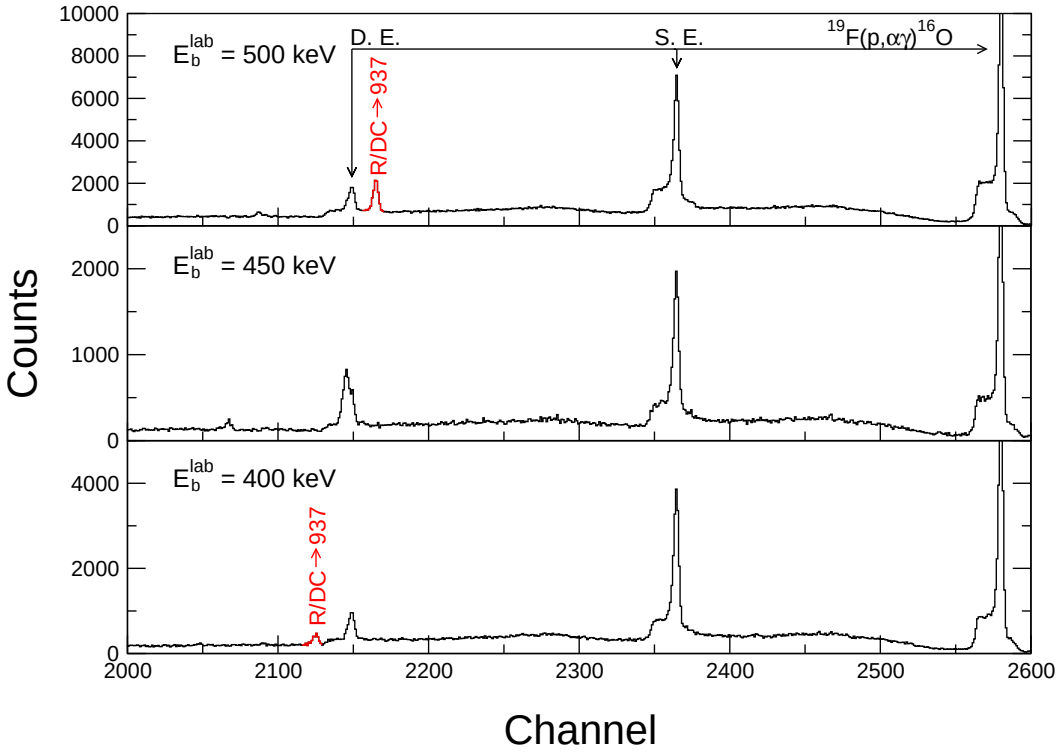

Figure 4.9: Sample γ-ray spectra for bombarding energies of E_p^{lab} = 500 keV (top), 450 keV (middle) and 400 keV (bottom). The peak corresponding to the primary transition to the E_x = 937 keV state in ^{18}F is marked in red. R/DC refers to resonant or direct capture. The three peaks corresponding to decay of the ^{16}O nucleus resulting from the ^{19}F(p,$\alpha\gamma$)^{16}O reaction are marked.

Transition		E_p^{lab} (keV)					
$E_{x_i} \rightarrow E_{x_f}$	η^{peak}	500	450	400	325	300	275
937 → 0	0.0194	30221(218)	11700(179)	5820(109)	1202(95)	689(51)	456(61)
1042 → 0	0.0186	522(74)	229(107)	197(65)			
1081 → 0	0.0183	525(75)	365(123)	144(73)			
2101 → 0	0.0127	522(117)		107(71)			
2523 → 0	0.0110	1031(68)	344(42)	108(30)			
3062 → 0	0.0097	1003(69)	479(42)	243(40)	59(27)	25(10)	
3839 → 0	0.0081	1374(78)	472(50)	287(42)	47(27)	30(13)	

Table 4.5: Counts for secondary decays to the ground state for each bombarding energy. The notation denotes Intensity(uncertainty). Excitation energies are in units of keV. Also included are the associated detection peak efficiency values.

fragmented resulting in more transitions with significant contributions. Secondly, the position of the primary peaks decreased in energy with decreasing bombarding energy, making it more difficult to account for room background contributions. Analysis of the total number of proton captures was further complicated, using either method, by the need to correct for coincidence summing. This required knowledge of the branching ratios of the primary transitions which were not previously available. This will be discussed in depth in Sec. 4.3.4.

4.3.2 Effective Interaction Energy

For measuring a direct capture cross section, the interaction energy is more complicated to determine than with a narrow resonant cross section. All energy dependent quantities can be evaluated at the resonance energy for a narrow resonance. Since interactions take place over the entire width of the target when measuring a smoothly varying cross section, an effective interaction energy is necessary. The effective energy, E_{eff}, is the energy, corresponding to half of the integrated yield, which separates the integrated cross section between the bombarding energy, E_p, and the bombarding energy minus the width of the target, E_p - ΔE, into two equal parts. That is

$$\int_{E_p-\Delta E}^{E_{eff}} \sigma(E)dE = \int_{E_{eff}}^{E_p} \sigma(E)dE. \tag{4.6}$$

The width of the target at the bombarding energy, $\Delta E(E_p)$, is found by correcting the measured target thickness at E_r = 519 keV, $\Delta E(519)$, for the change in stopping power (see Eq. 3.12) from E_r^{lab} = 519

Transition	E_p^{lab} (keV)					
R/DC → E_{x_f}	500	450	400	325	300	275
R/DC → 937	5919(137)		959(71)	241(48)	117(23)	37(11)
R/DC → 1121		334(48)	186(50)			
R/DC → 2101	86(42)					
R/DC → 2523	1047(79)	382(52)	148(33)			
R/DC → 3062	922(70)	437(41)	305(46)	76(31)	45(15)	18(10)
R/DC → 3358	196(49)					
R/DC → 3791	1531(91)		105(55)			33(20)
R/DC → 3839	5194(134)	1654(159)	807(75)	196(44)	122(29)	
R/DC → 4116	973(115)	437(129)	289(69)			
R/DC → 4398	370(105)		241(57)			
R/DC → 4652	341(95)					
R/DC → 4753	153(66)					
R/DC → 4860	110(84)					
R/DC → 4964	544(102)	405(124)	395(86)		137(46)	

Table 4.6: Counts for primary transitions for each bombarding energy. R/DC refers to the combination of resonant and direct capture contributions and excitation energies are in units of keV. The notation denotes Intensity(uncertainty)

keV to the stopping power at the new bombarding energy, using the following equation [1]:

$$\frac{\Delta E(519)}{\epsilon_{eff}(519)} = \frac{\Delta E(E_p)}{\epsilon_{eff}(E_p)}, \tag{4.7}$$

where ΔE(E_{res}^{lab} = 519) is obtained from the fit to the target thickness data shown in Fig. 4.7. This gives:

$$\Delta E = 4.748 - 0.0214 * Q_{accum} \tag{4.8}$$

It is important to know the proper accumulated charge value, Q_{accum}, to use for the bombarding energy of interest. These values are presented in Tab. 4.7 as the "Accumulated BCI Midpoint" for each bombarding energy. This gives one value of Q_{accum} for each bombarding energy. The corresponding E_{res} = 519 keV target thickness was then calculated using Eq. 4.8, yielding a unique target thickness at 519 keV for each of the six bombarding energies. These values are listed in Tab. 4.7. The target thickness was then corrected using Eq. 4.7, to give the target thickness for each bombarding energy at the time the measurement was performed. These values are included in Tab. 4.8.

E_p^{lab} (keV)	Accumulated BCI Range (μC)	Accumulated BCI Midpoint (μC)	$\Delta E(E_r^{lab} = 519)$ (keV)
400	1286560 - 5550983	3418771.5	4.67 $\pm$ 0.15
500	5746554 - 8958545	7352549.5	4.59 $\pm$ 0.15
450	9158208 - 12775306	10966757	4.51 $\pm$ 0.16
325	13024117 - 17208575	15116346	4.42 $\pm$ 0.17
300	18093079 - 22505137	20299108	4.31 $\pm$ 0.19
275	22645148 - 27811369	25228259	4.21 $\pm$ 0.21

Table 4.7: Midpoints of the accumulated BCI ranges and associated target widths at E_r^{lab} = 519 keV resonance for each bombarding energy evaluated.

E_p^{lab} (keV)	$\epsilon_{eff}^{lab}(E_p)\left(\frac{eVcm^2}{atom}\right)$	$\Delta E(E_p^{lab})$ (keV)	E_{eff}^{cm} (keV)
500	(19.37 $\pm$ 0.74)$\times 10^{-15}$	4.67 $\pm$ 0.30	469.88 $\pm$ 0.45
450	(20.39 $\pm$ 0.78)$\times 10^{-15}$	4.82 $\pm$ 0.31	422.59 $\pm$ 0.46
400	(21.50 $\pm$ 0.82)$\times 10^{-15}$	5.26 $\pm$ 0.33	375.19 $\pm$ 0.46
325	(23.53 $\pm$ 0.89)$\times 10^{-15}$	5.45 $\pm$ 0.36	304.31 $\pm$ 0.46
300	(24.35 $\pm$ 0.93)$\times 10^{-15}$	5.49 $\pm$ 0.38	280.70 $\pm$ 0.47
275	(25.19 $\pm$ 0.96)$\times 10^{-15}$	5.54 $\pm$ 0.40	257.09 $\pm$ 0.47

Table 4.8: Effective interaction energies and stopping power corrected target thicknesses for each experimental bombarding energy. The listed stopping powers are calculated using the bombarding energies.

Linear variations in the cross section from $\sigma_1 = \sigma(E_p)$ to $\sigma_2 = \sigma(E_p - \Delta E)$, result in [1, 3]:

$$E_{eff} = E_0 - \Delta E(E_p) + \Delta E(E_p)\left[\frac{\sigma_2}{\sigma_2 - \sigma_1} + \sqrt{\frac{\sigma_1^2 + \sigma_2^2}{2\left(\sigma_1 - \sigma_2\right)^2}}\right]. \tag{4.9}$$

The total cross section curve from Fig. 4.1 was interpolated to find reasonable values of σ_1 and σ_2. The requirement of linearity of the cross section for the use of Eq. 4.9 was the major reason for the choice of a target of $\approx$ 5 keV thickness. The results of the calculations of the effective interaction energies, E_{eff}, are presented in Tab. 4.8.

4.3.3 Cross Sections Before Summing Corrections

The cross section at the effective interaction energy, $\sigma(E_{eff}^{cm})$, for each individual transition was calculated by combining the data from Tab. 4.8 and the following expression [1]

$$\sigma\left(E_{eff}\right) = \frac{Y\left(E\right)}{n} = Y\left(E\right)\frac{\epsilon_{eff}\left(E\right)}{\Delta\left(E\right)}. \tag{4.10}$$

The reaction yield is denoted by Y(E) and n is the number of target nuclei per unit area. The cross section is converted to an astrophysical S-factor by Eq. 1.2. The values necessary for calculation of the S-factor contributions from the secondary transitions are provided in Tabs. 4.5 and 4.8. These S-factor contributions are shown as black data points in Fig. 4.10. Each level in ^{18}F from which a decay to the ground state was detected is included. As discussed previously, some transitions are missing due to varying background contributions and rapidly declining reaction cross sections. The red circles represent reasonable, by eye, estimates of the functional energy dependence of the S-factor contribution for the missing levels. These values are only used to find an approximate contribution for missing levels. Figure 4.11 shows the total S-factor contributions from all secondary decays to the ground state. These data points constitute the sum of the contributions from each of the seven individual levels. The black points represent the sum of the measured contributions and the red points are the sum of the contributions including the estimated missing transitions. The blue points show the direct capture contributions measured by Rolfs [6] with the associated uncertainty of 18%. The latter data were first presented in Fig. 4.1. Figure 4.11 provides a first indication that we do not reproduce the results of Rolfs [6].

S-factor contributions from each observed primary transition were calculated using the values from Tabs. 4.6 and 4.8. These are shown as the black points in Figs. 4.12 and 4.13. The red curves represent polynomial fits to the measured S-factor contributions and in some cases a green curve is also included which represents a second reasonable description of the data. These fits were then used to find the red points, which are estimated values of the contributions from missing transitions. The individual measured transitions were summed and displayed as black points in the bottom right plot in Fig. 4.13. The red points constitute the total S-factor contribution including the missing transitions. The E_{eff}^{lab} = 423 keV S-factor is missing nearly half of the estimated contribution as a result of the

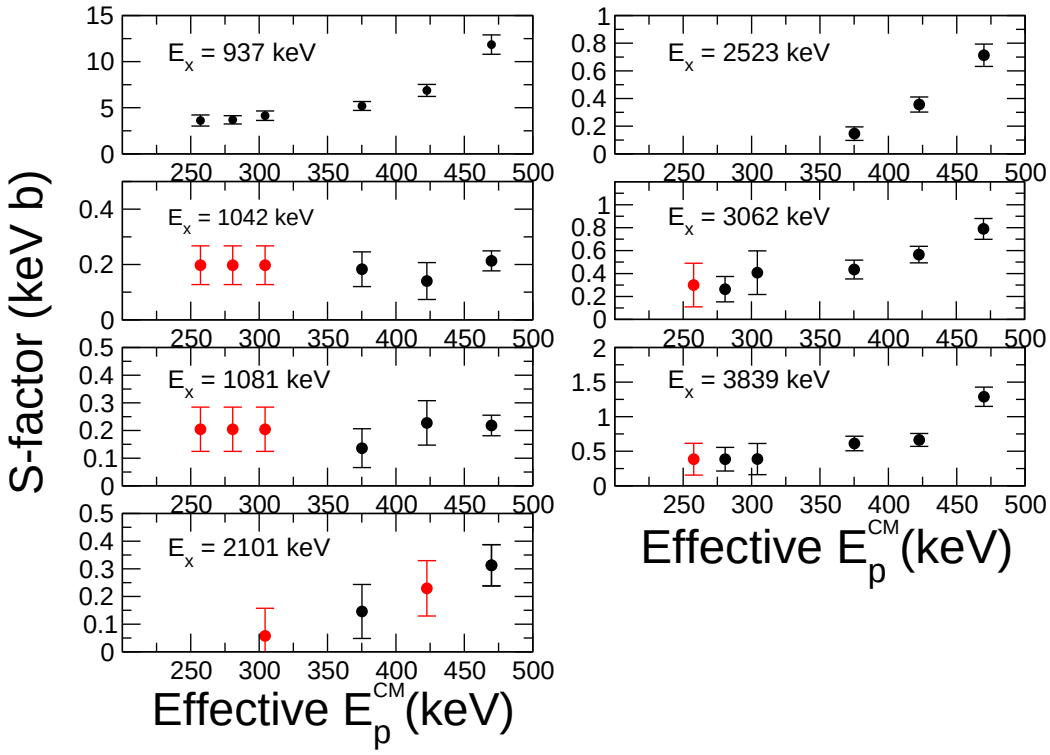

Figure 4.10: Individual S-factor contributions from secondary decays to the ground state ($E_x \rightarrow 0$).

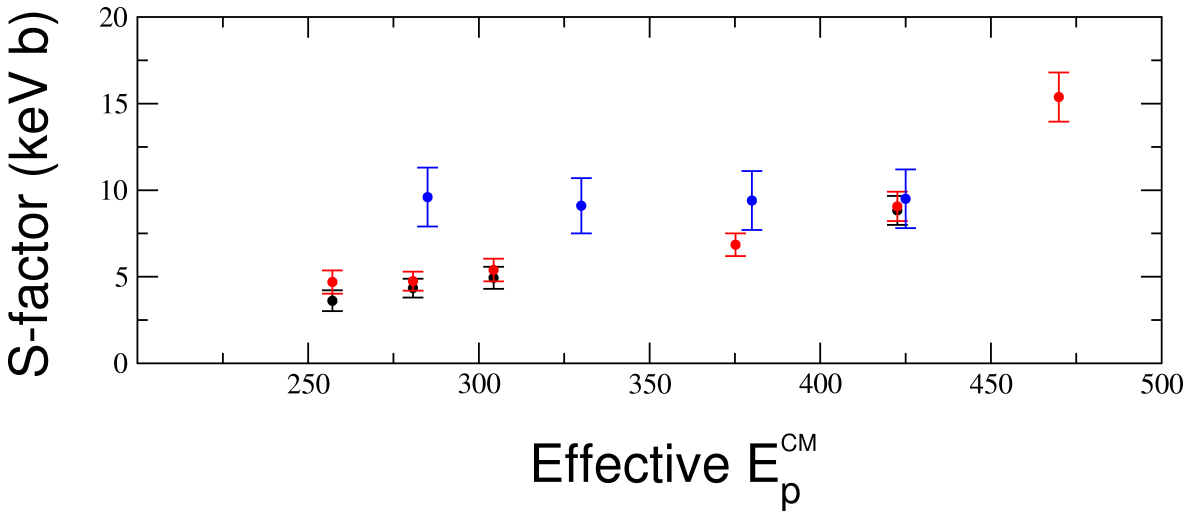

Figure 4.11: Total S-factor contributions from all secondary decays to the ground state ($E_x \rightarrow 0$).

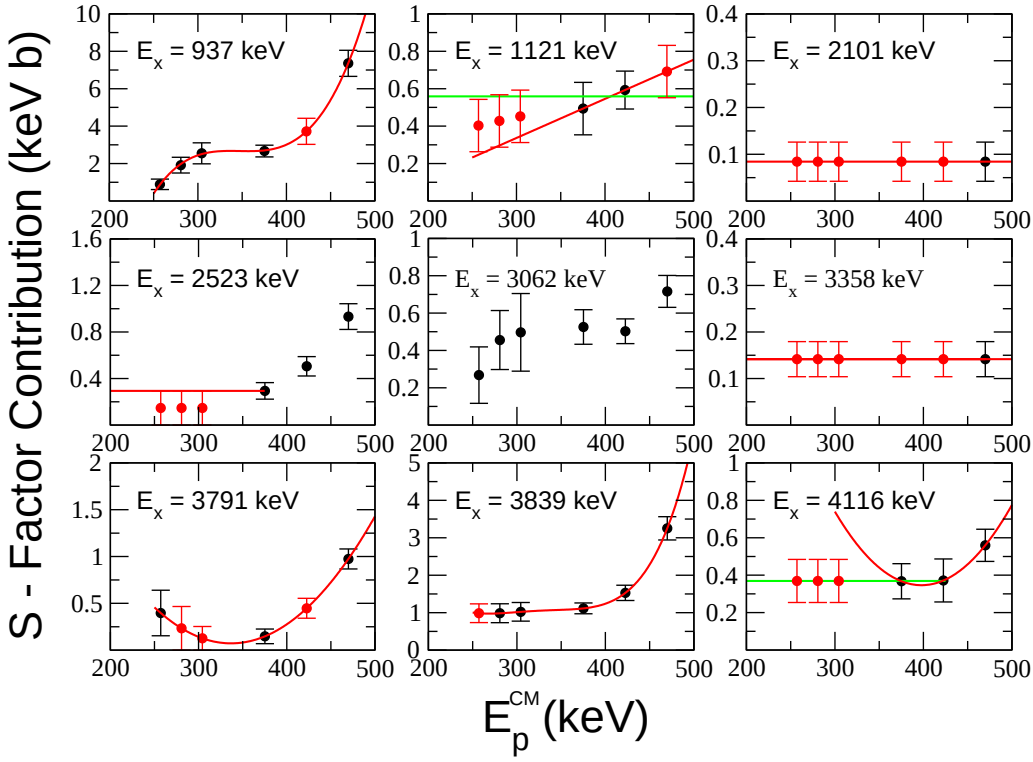

Figure 4.12: S-factor contributions from individual primary transitions I.

target fluorine contamination. In addition, the total S-factor contributions at the effective interaction energies E^{lab}_{eff} = 304, 281 and 257 keV are adjusted significantly more than they were when analyzing the secondary transitions. This is because the primary contributions are far more fragmented, while the vast majority of the secondary contributions are found in the E_x = 937 keV to ground state transition. The adjustments to the primary S-factor contributions may be overestimated for the captures into the E_x = 2101, 3358, 4652, 4753 and 4860 keV levels. These are estimated based only on a single transition seen at E^{cm}_{eff} = 470 keV. These are not final S-factor contributions because they have yet to be corrected for coincidence summing and the effects of this potential overestimation will be further explored. The blue points in Fig. 4.13 are the direct capture contributions to the total S-factor from Ref. [6]. Again, the total measured S-factor contribution, even after correction for missing transitions, does not agree with the direct capture S-factor reported by Rolfs.

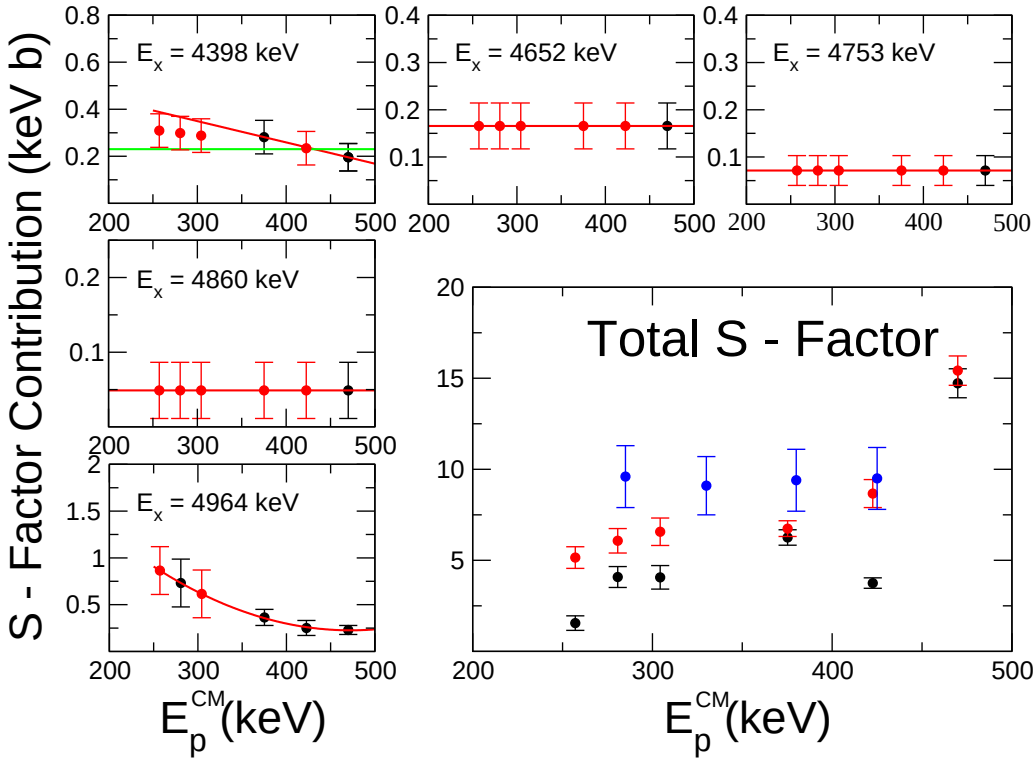

Figure 4.13: S-factor contributions from individual primary transitions II.

4.3.4 Coincidence Summing Corrections

As discussed in Sec. 4.2.2 for the analysis of the ^{56}Co source data, since our detector was located in a close running geometry, coincidence summing effects must be accounted for. The summing corrections were performed using two versions of a C code written by Richard Longland. The first is the same code that was used to summing correct the ^{56}Co and ^{14}N(p,γ)^{15}O data used for the detector efficiency measurements discussed in Sec. 4.2.2. These codes are both based on the matrix formalism presented in Ref. [30] and the specific codes and their use are discussed in detail in Ref. [32]. To properly correct the measured data for coincidence summing, it is necessary to know the detector peak and total efficiencies for each primary and secondary branch in the decay of ^{18}F. The primary and secondary branching ratios are also needed. The secondary transition branchings are well known [33] and the detector peak and total efficiencies were measured and simulated (see Sec. 4.2.2). The primary branching ratios are, however, not known. They result from a combination of capture into the tails of the 557 and 677 keV resonances and direct capture transitions. These primary branches can be found using the matrix formalism of Ref. [30]. This was accomplished by varying the input primary branching ratios needed for the calculations of the summing corrections, iteratively, until the observed number of transitions in the measured spectra were reproduced by the summing corrections code. The code **sumb.c** was updated to allow for decays which have nonzero branching but are not observed in the measured spectra.

Reasonable starting values for the primary branching ratios were needed for input to **sumb.c**. These starting values were found by taking the ratio of the S-factor contribution from an individual primary transition to the total contribution from all observed primary transitions. These individual primary transitions were shown in Figs. 4.12 and 4.13. The relative S-factor contributions from each individual primary transition are presented in Tab. 4.9. These values were used as the initial inputs to the **sumb.c** code for the primary branching ratios. They were iteratively adjusted as described above to find the true primary branching ratios. These output primary branching ratios from **sumb.c** were all within the original uncertainties of the input primary branchings for the E_p^{lab} = 325, 400 and 500 keV data. Thus, the current method for estimating the primary branching ratios from the individual S-factor contributions produced accurate values at these bombarding energies. For the E_p^{lab} = 450 keV

Transition	E_p^{lab} (keV)					
R/DC → E_x	500	450	400	325	300	275
R/DC → 937	0.47(3)	0.43(5)	0.39(3)	0.39(6)	0.32(5)	0.17(5)
R/DC → 1121	0.046(9)	0.068(12)	0.07(2)	0.07(2)	0.07(2)	0.08(3)
R/DC → 2101	0.005(3)	0.010(5)	0.012(6)	0.013(6)	0.014(7)	0.016(8)
R/DC → 2523	0.060(7)	0.058(10)	0.043(10)	0.02(2)	0.02(2)	0.03(3)
R/DC → 3062	0.046(6)	0.058(9)	0.078(14)	0.08(3)	0.08(3)	0.05(3)
R/DC → 3358	.009(2)	0.016(5)	0.021(6)	0.022(6)	0.023(7)	0.028(8)
R/DC → 3791	0.063(7)	0.052(13)	0.022(11)	0.019(19)	0.04(4)	0.08(4)
R/DC → 3839	0.211(19)	0.18(2)	0.16(2)	0.16(4)	0.16(4)	0.19(4)
R/DC → 4116	0.036(6)	0.043(13)	0.054(13)	0.056(18)	0.061(19)	0.07(2)
R/DC → 4398	0.013(4)	0.027(8)	0.042(10)	0.044(12)	0.049(12)	0.060(14)
R/DC → 4652	0.011(3)	0.019(6)	0.025(7)	0.025(8)	0.027(8)	0.032(10)
R/DC → 4753	0.005(2)	0.008(4)	0.011(5)	0.011(5)	0.012(5)	0.014(6)
R/DC → 4860	0.003(2)	0.006(4)	0.007(6)	0.007(6)	0.008(6)	0.010(7)
R/DC → 4964	0.015(3)	0.029(9)	0.054(13)	0.09(4)	0.12(4)	0.17(4)

Table 4.9: Initial values for the primary branching ratio inputs into **sumb.c**. These represent the relative contributions of primary S-factor transitions to each excited level in ^{18}F. The transitions are listed in column one with R/DC for the combination of resonant and direct capture and E_x is the excitation energy in keV.

data, however, the original input branching ratio for the primary transition to the E_x = 937 keV level was strongly adjusted by **sumb.c**. There existed no experimentally observed value for this transition to constrain the branching ratio adjustment and given the success of the E_p^{lab} = 500, 400 and 325 keV estimated branching ratios, the original primary branching estimate for transition to the E_x = 937 keV level was used instead of the adjusted value. Some branching ratios for the primary transitions at E_p^{lab} = 300 keV were varied by **sumb.c** slightly outside the uncertainties on the original input estimates, but this was expected due to the large number of unobserved primary transitions at this bombarding energy. The original primary branching ratios for the E_p^{lab} = 275 keV data were analyzed separately as a result of extreme over-correction of the primary branchings by **sumb.c**.

The second code used for this analysis, **sum.c**, is a simpler version of the matrix formalism used in **sumb.c**. This code assumes that all branchings are known and fixed and calculates a summing corrected total number of disintegrations of the final nucleus. The results of the branching ratio adjustments by **sumb.c** can be used as inputs to **sum.c**. This process was straightforward for the E_p^{lab} = 325, 400, 450 and 500 keV data. The E_p^{lab} = 300 keV data were tested for the effects of assuming a

E_p^{lab} (keV)	E_{eff}^{cm} (keV)	sum corrected disintegrations	937 → 0 correction
500	469.88	2352190 ± 96910	13.4%
450	422.59	947079 ± 85995	13.6%
400	375.19	470054 ± 33045	14.2%
325	304.31	100213 ± 14000	13.7%
300	280.70	62130 ± 9458	15.1%
275	257.09	45287 ± 8917	17.5%

Table 4.10: Final sum-corrected values of the total disintegrations for each of the six different bombarding energies.

flat distribution of the S-factor for the E_x = 2101, 3358, 4652, 4753 and 4860 keV primary transitions. The primary branching ratios were recalculated assuming these transitions to be negligible and the total number of disintegrations of ^{18}F were within the uncertainties of the original calculation. These two calculated values for the total number of disintegrations were averaged for the final result. The E_p^{lab} = 275 keV data were tested in the same way for the effects of removing the same five unseen transitions and the results, which were within uncertainties, were then averaged. For this reason, the inability to adjust the primary branching ratios of the 275 keV data is not of major concern. The final values for the summing corrected total number of disintegrations of ^{18}F measured at each of the six bombarding energies are presented in Tab. 4.10.

The total number of ^{18}F disintegrations is a weighted average of the total value computed for each measured transition. The final average is in excellent agreement with the value calculated from the E_x = 937 keV to ground state transition (937 → 0) alone. The uncertainties in the total number of disintegrations were adopted from the relative uncertainty of the 937 → 0 transition, since this line has the best statistics and was always in agreement with the average. The effects of coincidence summing corrections are also presented in Tab. 4.10. These are illustrated by the 937 → 0 transition. This line should have the largest correction and is therefore a good measure of the effects of coincidence summing on the measured data. These corrections ranged from ≈ 13% to ≈ 17%.

E_p^{lab} (keV)	E_{eff}^{cm} (keV)	$\sigma_{total}(E_{eff}^{cm})$ $(\times 10^{-9} b)$	$S_{total}(E_{eff}^{cm})$ (keV b)	$S_{557+677}(E_{eff}^{cm})$ (keV b)	$S_{DC}(E_{eff}^{cm})$ (keV b)
500	469.88	488 ± 49	17.89 ± 1.80	14.60 ± 3.07	3.29 ± 3.56
450	422.59	178 ± 23	10.80 ± 1.40	6.44 ± 1.31	4.36 ± 1.92
400	375.19	72.7 ± 8.4	8.13 ± 0.94	3.67 ± 0.73	4.47 ± 1.19
325	304.31	18.3 ± 3.1	6.69 ± 1.13	1.99 ± 0.38	4.71 ± 1.19
300	280.70	10.8 ± 1.9	6.46 ± 1.16	1.68 ± 0.32	4.78 ± 1.21
275	257.09	6.6 ± 1.5	6.96 ± 1.53	1.45 ± 0.28	5.52 ± 1.56

Table 4.11: Final measured total cross sections and associated total S-factors. Calculated resonance tail contributions for E_r^{cm} = 557 and 677 keV resonances are also included to allow for the subtraction of the resonance contribution from the total S-factors. This gives the measured direct capture S-factors, $S_{DC}(E_{eff}^{cm})$.

4.3.5 Coincidence Summing Corrected Direct Capture S-factor

Application of summing corrections to the total number of ^{18}F disintegrations allowed for calculation of the measured total cross section for ^{17}O(p,γ)^{18}F. This is presented in Tab. 4.11 along with the total S-factor. The contribution to the total S-factor coming from the tails of the E_r^{cm} = 557 and 677 keV resonances, $S_{557+677}(E_{eff}^{cm})$, is also included. Calculating the resonance tail contribution only required the experimental resonance strengths and widths for the two resonances. The uncertainty in $S_{557+677}(E_{eff}^{cm})$ was found by varying the resonance width over the corresponding uncertainty. This calculation yielded the same result as interpolation of the resonance tail S-factor curve from Fig. 4.1. The resonance tail contribution was then subtracted incoherently from the total S-factor contribution to yield the direct capture contribution, since any interference between the major direct capture transitions and the resonance contribution is proportional to $P_2\,(cos\theta)$ and is therefore negligible at the experimental detection angle of 55°. The results are provided in Tab. 4.11.

Figure 4.14 shows the newly measured total S-factor for ^{17}O(p,γ)^{18}F as red points. These data are shown in comparison with the previous results of Rolfs [6] and Chafa et al. [21] (see Fig. 4.1). A linear S-factor scale is chosen to better compare the current data with the previous descriptions. The measured total S-factor points are in agreement with the predictions of Fox et al. [7] which are represented by the solid black line. This supports the claim made in Ref. [7] that the resonance tail contributions need to be taken into account when considering the measured total S-factor data. It is not correct to assume that the direct capture contribution dominates the total S-factor at every energy

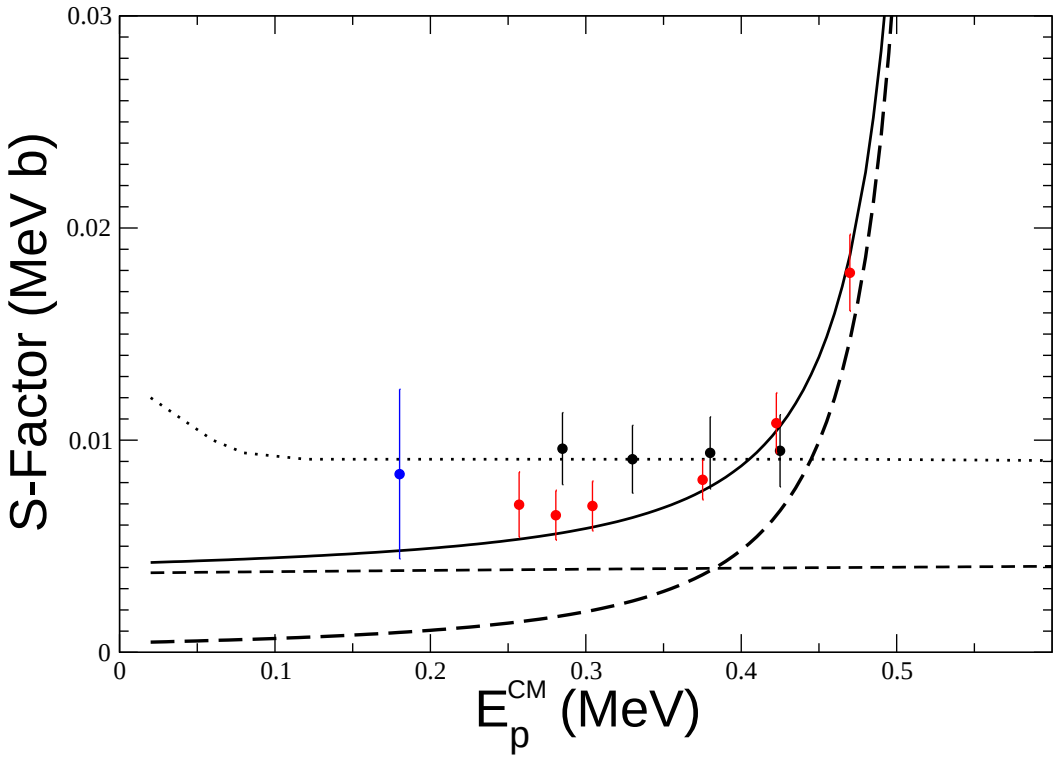

Figure 4.14: Total measured S-factor (red points) from present work. Otherwise the plot is identical to Fig. 4.1 except for the linear S-factor scale.

measured. This measurement also provides an experimental test of the method of estimating direct capture cross sections using measured spectroscopic factors (see Eq. 1.31). This method has been used extensively in the field of nuclear astrophysics, yet previous experimental investigations of its validity are rare.

The measured total S-factor is displayed in Fig. 4.15 as red points. The black dashed line represents the resonance tail contribution from the E_r^{cm} = 557 and 677 keV resonances. Subtraction of the resonant contribution from the total S-factor yielded the direct capture S-factor shown as green points. The direct capture S-factor was assumed to be constant, since the calculated curve presented in Fox et al. [7] is nearly constant over the energy range explored in this measurement. The new direct capture S-factor curve was then chosen to be an average of the extracted direct capture S-factor points. The un-

certainty in each data point has contributions from three sources. The first is a statistical contribution resulting from counting statistics and summing corrections. The second is a systematic uncertainty resulting from stopping powers, detection efficiencies and target thickness, which amounted to $\approx 9\%$ of the measured S-factor. The third is the uncertainty in the resonance tail contributions. The relative magnitudes of these uncertainties can be found in Tab. 4.11. The average of the five direct capture points was weighted by the statistical uncertainty on each point. The uncertainty on the weighted average was then added in quadrature with the average systematic uncertainty of the five points and the average resonance tail contribution of the five points. This resulted in a final constant value for the direct capture S-factor at low energies of:

$$S_{DC}(E_{eff}^{cm}) = 4.6 \pm 1.1 \text{ (keV b)} \qquad \text{for } E_{eff}^{cm} < 450 \text{ keV}. \tag{4.11}$$

This corresponds to a 23% uncertainty on the new direct capture S-factor contribution, which is a factor of 2 smaller than that of Ref. [7]. This is shown as the purple band in Fig. 4.15 and is in agreement with the prediction of Fox et al. [7]. The new direct capture S-factor contribution is well below the S-factor curve from Ref. [6] and at the center of the classical nova Gamow peak range ($\approx$180 keV) they disagree by a factor of ≈ 2. The measured point at E_r^{cm} = 183 keV from Ref. [21] is not useful for comparison purposes because of the large uncertainty associated with this point. New thermonuclear reaction rates were calculated using the direct capture S-factor contribution discussed herein and are presented in Chap. 5.

The work presented in this chapter has been submitted for publication in The Physical Review C.

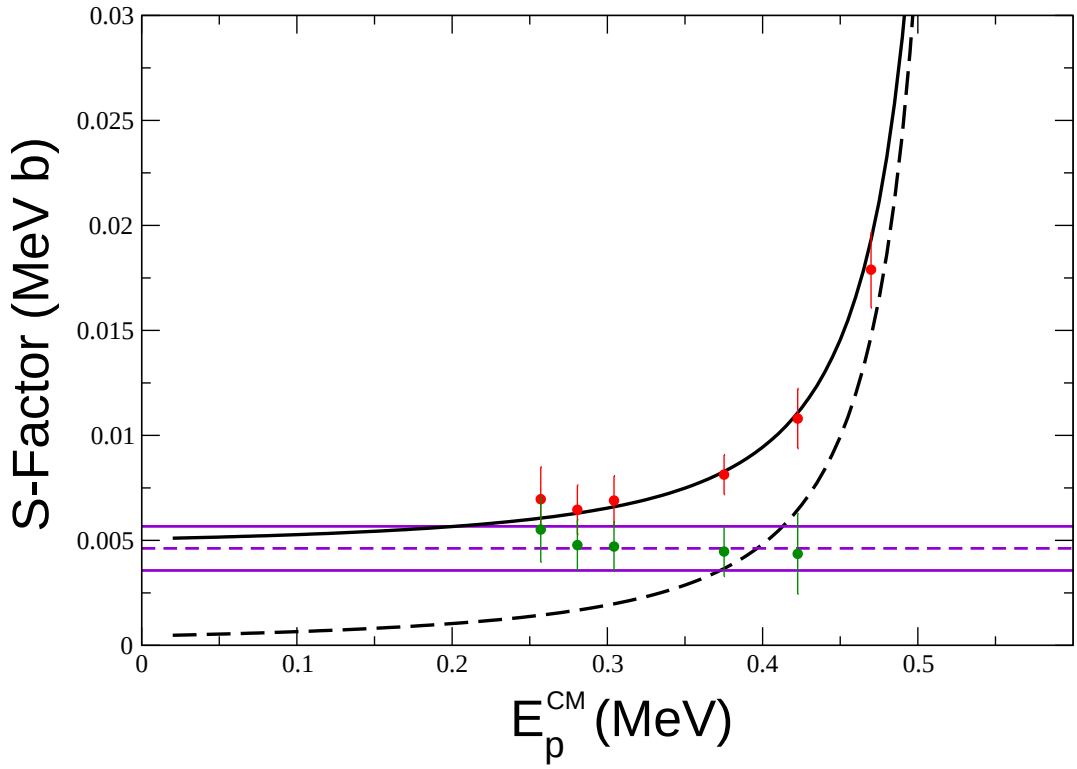

Figure 4.15: Total measured S-factor (red points) from present work. The E_r^{cm} = 557 and 677 keV resonance tail contributions (dashed curve) have been subtracted, leaving the measured direct capture S-factor (green points). The weighted average of these green points give a flat direct capture S-factor curve (purple band) with 23% associated uncertainty. The new total S-factor curve (solid line) is the sum of the resonance and direct capture contributions.

5 Reaction Rate Calculations

The reaction rates of the competing ^{17}O(p,α)^{14}N and ^{17}O(p,γ)^{18}F reactions are of interest to classical nova simulations and other environments where the CNO cycles are in operation. In this chapter the new Monte Carlo method for calculating reaction rates discussed in Sec. 1.5 and the new method of matching experimental rates to statistical model calculations that was presented in Chap. 2 will be combined to calculate new thermonuclear reaction rates for ^{17}O(p,α)^{14}N and ^{17}O(p,γ)^{18}F using the code **RatesMC** [8].

5.1 The ^{17}O(p,α)^{14}N Reaction Rate

The total reaction rate of ^{17}O(p,α)^{14}N consists entirely of resonant contributions. The rate will be made up of contributions from several types of resonances, including subthreshold resonances, low lying resonances, interfering resonances, and both narrow and broad resonances. Each type of resonance will be explored individually in this section, and the specific reaction rate contributions will then be combined to determine the total reaction rate of ^{17}O(p,α)^{14}N.

5.1.1 Narrow Resonance Contributions to the ^{17}O(p,α)^{14}N Reaction Rate

The narrow resonance contribution to the reaction rate is given by Eq. 1.20. For the ^{17}O(p,α)^{14}N reaction there are unresolved discrepancies in the literature values of the narrow resonance strengths. Table 5.1 displays the literature values for the narrow resonances in ^{17}O(p,α)^{14}N. The column labeled "Current" is our best resonance strength that has been derived from the available literature. The NACRE [14] strengths represent a weighted average of the literature values for each of the resonances, but there are some problems with the interpretation of these data.

The strength for the E_r^{cm} = 530 keV resonance is listed in Ref. [34] as an upper limit. The accepted

NACRE [14] strength is taken to be 10% of this value. Though it is the standard practice, 10% is an arbitrary choice. It is not statistically valid to treat this resonance strength as an arbitrary value with a large uncertainty. This must be handled much more carefully by consideration of the partial widths. This procedure is discussed in App. A.1.

The issue of the two $J^{\pi} = 3^{-}$ states at E_r^{cm} = 633.9 keV and E_r^{cm} = 635.5 keV is interesting. It seems to be the case that Brown [35] lists a value that includes both resonances, while Kieser [36] was able to resolve these two states and has listed them separately. The strength quoted by NACRE [14] for the E_r^{cm} = 633.9 keV state is an average of the two strengths listed by Refs. [35, 36]. This is incorrect and should be handled in one of two ways. Either the two states should be separated and the strengths from Ref. [36] should be used for each resonance, or the strengths associated with these two states should be summed and then averaged with the strength listed in Ref. [35]. The second approach was adopted here. The resonance energy was chosen as E_r^{cm} = 633.9 keV to coincide with the energy of the lower of the two resonances. This choice was made for consistency with the listings in Refs. [14, 35].

The final discrepancy in the literature involves the two states listed at E_r^{cm} = 1040.5 keV and E_r^{cm} = 1170.5 keV. NACRE [14] has attributed a strength of $\omega\gamma_{p\alpha}$ = 150 $\pm$ 6 eV to the E_r^{cm} = 1040.5 keV state from Brown [35]. However, it is clear in Ref. [35] that this resonance strength is listed for the E_r^{cm} = 1170.5 keV resonance. Rolfs [34] also quoted a strength of $\omega\gamma_{p\alpha}$ = (150 $\pm$ 6) eV from Brown [35] for the E_r^{cm} = 1170.5 keV resonance. This strength has been incorrectly assigned to the E_r^{cm} = 1040.5 keV resonance by NACRE [14]. The NACRE value of $\omega\gamma_{p\alpha}$ = (109 $\pm$ 15) eV from Kieser [36] does not come from the same table in Ref. [36] as the other values listed in the NACRE table for this reference. Reference [36] does, however, include a list of partial widths for the ^{17}O(p,α)^{14}N reaction, which includes this resonance. If the strength for this resonance is calculated using these partial widths, a value of $\omega\gamma_{p\alpha}$ = (111 $\pm$ 17) eV is obtained.

Owing to the discrepancies explained above, the calculation of the total reaction rate of ^{17}O(p,α)^{14}N will not use the directly measured resonance strengths. Instead, the rate will be calculated by integration over the estimated cross section of these resonances. Although the energy dependence of these resonances is relatively unimportant and integration is a much more tedious procedure, the strengths listed above are not completely understood. Therefore, the partial widths, listed in Ref. [36] for each

E_R^{CM} (keV)	J^π	$\omega\gamma_{p\alpha}$ (eV)				
		Brown	Kieser	Rolfs	NACRE	Current
489.9 ± 1.2	4^-	50.0 ± 5.0	47.9 ± 5.4	-	49.0 ± 3.7	49.0 ± 3.7
530.0 ± 0.3	0^+	-	-	< 0.17	$.017 \pm {}^{.15}_{.017}$	< 0.17
556.7 ± 1.0	3^+	-	-	2.25 ± 0.42	2.25 ± 0.42	2.25 ± 0.42
633.9 ± 0.9	3^-	43 ± 4	29.8 ± 3.5	-	35.5 ± 2.6	46.1 ± 2.9
635.5 ± 3	3^-	-	19.7 ± 2.3	-	19.7 ± 2.3	-
655.5 ± 2.5	1^+	-	5.0 ± 0.6	-	5.0 ± 0.6	5.0 ± 0.6
676.7 ± 1.0	2^+	-	-	5.8 ± 1.2	5.8 ± 1.2	-
704.0 ± 0.9	3^+	100 ± 10	97.0 ± 10.4	-	98.6 ± 7.2	98.6 ± 7.2
779.0 ± 1.8	2^+	23 ± 2	24.3 ± 2.7	-	23.4 ± 1.6	23.5 ± 1.6
878.4 ± 1.6	3^+	39 ± 4	37.6 ± 4.2	-	38.4 ± 2.9	38.3 ± 2.9
960.5 ± 1.6	5^+	-	1.04 ± 0.22	-	1.04 ± 0.22	1.04 ± 0.22
1037.2 ± 0.9	2^-	36 ± 4	38.9 ± 4.8	-	37.2 ± 3.1	37.2 ± 3.1
1040.5 ± 4	1^-	-	-	-	150 ± 16	-
1170.5 ± 1.5	4^+	150 ± 16	-	-	109 ± 15	150 ± 16

Table 5.1: Narrow resonances used in the calculation of the total reaction rate for ^{17}O(p,α)^{14}N. Resonance energies are taken from Ref. [33] and strengths are taken from Refs. [14, 34, 35, 36].

E_R^{cm} (keV)	J^π	Γ_γ (eV)	Γ_p (eV)	Γ_α (eV)
65.1 ± 0.5	1^-	$(4.4 \pm 0.2)\times10^{-1}$	$(18.8 \pm 3.2)\times10^{-9}$	130 ± 5
183.35 ± 0.25	2^-	$(9.6 \pm 3.6)\times10^{-3}$	$(3.99 \pm .24)\times10^{-3}$	13.3 ± 5.5

Table 5.2: Partial widths for the two lowest lying resonances in ^{17}O(p,α)^{14}N. Resonance energies are taken from Ref. [19] for E_r^{cm} = 65.1 keV and averaged from Refs.[7, 21, 25] for E_R^{CM} = 183.35 keV.

of the resonances, will be used in order to construct the Breit-Wigner cross sections. The rate contribution can be calculated using Eq. 1.24. This will be discussed in more detail later in this chapter.

5.1.2 Low-Lying and Subthreshold Resonances

Recall from Sec. 1.3.3 that it is often necessary to take the energy dependence of a resonance into account when calculating the reaction rate. This will require integration over the resonance cross section. The two lowest lying resonances in ^{17}O(p,α)^{14}N at $E_R^{cm} = 65.1$ keV and $E_R^{cm} = 183.4$ keV must be integrated in order to accurately determine their contributions to the total reaction rate at the lower temperatures of interest. Table 5.2 gives the values of the resonance energies and partial widths for both of these resonances. The resonance energy of $E_R^{cm} = 183.35$ keV is an average of the three most recent literature values [7, 21, 25].

The values of the partial widths listed in Tab. 5.2 can be easily calculated from available experimentally measured values for the strengths and total widths. The following values are known for the E_r^{CM} = 65.1 keV resonance:

$$\begin{aligned}
\omega\gamma_{\alpha\gamma}^{65} &= 0.44 \pm 0.02 \text{ eV} \\
\omega\gamma_{p\alpha}^{65} &= (4.7 \pm 0.8) \times 10^{-9} \text{ eV} \\
\Gamma_{\alpha}^{65} &= 130 \pm 5 \text{ eV} \\
\omega_{\alpha\gamma}^{65} &= \frac{2J+1}{(2j_{^{14}N}+1)(2j_{\alpha}+1)} = 1 \\
\omega_{p\alpha}^{65} &= \frac{2J+1}{(2j_{^{17}O}+1)(2j_{p}+1)} = \frac{1}{4}
\end{aligned}$$

The value for $\omega\gamma_{\alpha\gamma}^{65}$ is an average of the values from Refs. [34, 37, 38, 39]; $\omega\gamma_{p\alpha}^{65}$ is a correction to the value from Ref. [40] and Γ_{α}^{65} is taken from Ref. [41].

One can solve for the remaining two partial widths in terms of the above known quantities:

$$\Gamma_{\gamma}^{65} = \frac{\omega\gamma_{\alpha\gamma}}{\omega_{\alpha\gamma}(\Gamma_{\alpha} - \omega\gamma_{\alpha\gamma})} \tag{5.1}$$

$$\Gamma_{p}^{65} = \frac{\omega\gamma_{p\alpha}(\Gamma_{\alpha} + \Gamma_{\gamma})}{\omega_{p\alpha}\Gamma_{\alpha}} \tag{5.2}$$

This gives values of $\Gamma_{\gamma}^{65} = (0.44 \pm 0.02)$ eV and $\Gamma_{p}^{65} = (18.8 \pm 3.2) \times 10^{-9}$ eV.

The strengths for the 183 keV resonance are:

$$\begin{aligned}
\omega\gamma_{\alpha\gamma}^{183} &= 0.016 \pm 0.006 \text{ eV} \\
\omega\gamma_{p\gamma}^{183} &= (1.2 \pm 0.2) \times 10^{-9} \text{ eV} \\
\omega\gamma_{p\alpha}^{183} &= (1.66 \pm 0.17) \times 10^{-3} \text{ eV}
\end{aligned}$$

The value for $\omega\gamma_{p\gamma}^{183}$ is taken from Ref.[7]; $\omega\gamma_{p\alpha}^{183}$ is from the current work and $\omega\gamma_{\alpha\gamma}^{183}$ is from Ref. [34].

Again, using the definitions of the corresponding resonance strengths and solving for the partial

E_R^{cm} (keV)	$C^2S\,\theta_{sp}^2$	Γ_γ (eV)	Γ_α (eV)
-3.12 ± 0.57	0.054 ± 0.018	0.485 ± 0.051	42.8 ± 1.6
-1.64 ± 0.57	≤ 0.0082	0.894 ± 0.074	32.0 ± 2.1

Table 5.3: Input values for subthreshold resonances in ^{17}O(p,α)^{14}N. These will be numerically integrated to find the reaction rate contribution of each resonance. [5, 42]

widths, gives:

$$\Gamma_\alpha^{183} = \frac{3}{5}\left[\frac{\omega\gamma_{\alpha\gamma}\omega\gamma_{p\alpha} + \omega\gamma_{p\gamma}\omega\gamma_{\alpha\gamma} + 4\omega\gamma_{p\gamma}\omega\gamma_{p\alpha}}{\omega\gamma_{\alpha\gamma}}\right] \tag{5.3}$$

$$\Gamma_p^{183} = \frac{12}{5}\left[\frac{\omega\gamma_{\alpha\gamma}\omega\gamma_{p\alpha} + \omega\gamma_{p\gamma}\omega\gamma_{\alpha\gamma} + 4\omega\gamma_{p\gamma}\omega\gamma_{p\alpha}}{\omega\gamma_{p\alpha}}\right] \tag{5.4}$$

$$\Gamma_\gamma^{183} = \frac{3}{5}\left[\frac{\omega\gamma_{\alpha\gamma}\omega\gamma_{p\alpha} + \omega\gamma_{p\gamma}\omega\gamma_{\alpha\gamma} + 4\omega\gamma_{p\gamma}\omega\gamma_{p\alpha}}{\omega\gamma_{p\gamma}}\right] \tag{5.5}$$

Inserting the measured resonance strengths into the above equations gives for the partial widths: Γ_α^{183} = (13.3 $\pm$ 5.6) eV , Γ_p^{183} = (0.00399 $\pm$ 0.00024) eV and Γ_γ^{183} = (0.0096 $\pm$ 0.0036) eV.

For the case of ^{17}O(p,α)^{14}N, there are two subthreshold resonances which may contribute significantly to the total reaction rate at low temperatures. These have resonance energies of $E_r^{cm} = -3.12$ keV and $E_r^{cm} = -1.64$ keV. The proton width for a subthreshold resonance is described by Eq. 1.25. Table 5.3 includes all of the values necessary to calculate the partial widths for these two subthreshold resonances. Note that the values given for the $E_R^{cm} = -1.64$ keV resonance include an upper limit and must be treated carefully. Recall from Sec. 1.5 that the Monte Carlo rate calculation requires a statistically valid distribution for each resonance parameter. The procedure for describing the single particle reduced width for the case of an upper limit value is described in App. A.1. This resonance will have a large affect on the reaction rate at very low temperatures.

5.1.3 Higher Lying Resonances

The contribution to the reaction rate from resonances with $E_r^{cm} \geq$ 489.9 keV is found using Eq. 1.24. The partial widths for each of these resonances are given in Tab. 5.4. This list of higher lying resonances includes the narrow resonances discussed in Sec. 5.1.1 that do not have reliable literature resonance strength values. The partial widths were taken from Ref. [36], and were calculated using an

E_R^{CM} (keV)	J^π	Γ_p (eV)	Γ_α (eV)
489.9 ± 1.2	4^-	138 ± 26	106 ± 17
501.5 ± 3.0	(1^+)	0.20 ± 0.02	33.6 ± 3.3
556.7 ± 1.0	3^+	14000 ± 500	5.0 ± 0.6
633.9 ± 0.9	3^-	58.2 ± 7.0	133.0 ± 23.8
635.5 ± 3.0	3^-	40.8 ± 3.7	137.0 ± 34.7
655.5 ± 2.5	1^+	27 ± 3	575 ± 120
676.7 ± 1.0	2^+	10000 ± 500	27 ± 3
704.0 ± 0.9	3^+	525 ± 117	426 ± 82
779.0 ± 1.8	2^+	109 ± 11	286 ± 87
878.4 ± 1.6	3^+	277 ± 91	123 ± 25
960.5 ± 1.6	5^+	1.2 ± 0.1	560 ± 132
1026.5 ± 10.0	1^-	2920 ± 313	77090 ± 2000
1037.2 ± 0.9	2^-	368 ± 61	231 ± 40
1170.5 ± 1.5	4^+	9000 ± 1000	150 ± 24
1202.5 ± 5.0	2^-	16570 ± 1551	71500 ± 2000
1204.5 ± 10.0	(2^+)	2750 ± 450	210 ± 67
1250.5 ± 10.0	(3^-)	5000 ± 1000	30 ± 7
1594.5 ± 2.1	(4^+)	29400 ± 1000	500 ± 58
1640.5 ± 2.1	(1^+)	5000 ± 1000	55000 ± 5000
1684.5 ± 2.1	3^-	15820 ± 1427	44180 ± 15000

Table 5.4: Input parameters for the resonances to be integrated over for calculation of the total reaction rate in ^{17}O(p,α)^{14}N. Resonance energies taken from Ref. [33] and the particle partial widths are taken from Ref. [36].

R-matrix fit. There are two tables in Ref. [36] which list partial widths for resonances of $E_r^{cm} \geq 489.9$ keV. The values from Tab. 3 of Ref. [36] were chosen because they provide better agreement with the resonance strength values presented in Tab. 5.1. Equation 1.24 takes into consideration the effects of the tails of wider resonances which cannot be estimated using the narrow resonance approximation. Also, interference between resonances, which will be discussed in Sec. 5.1.4, requires knowledge of the full energy dependence of the interfering resonances.

Figure 5.1 shows the relative contributions to the total reaction rate for each of the resonance categories. The individual and total contributions were calculated using the Monte-Carlo sampling code **RatesMC** [8] which is described in Sec. 1.5. The two subthreshold resonances and the two low lying resonances are all considered individually, while the other 20 higher lying resonances listed in Tab. 5.4 are combined. The contributions from the E_r^{cm} = 65.1 and 183 keV resonances dominate the total reaction rate in the temperature range $0.02 < T_9 < 0.3$. The uncertainty in the total reaction rate

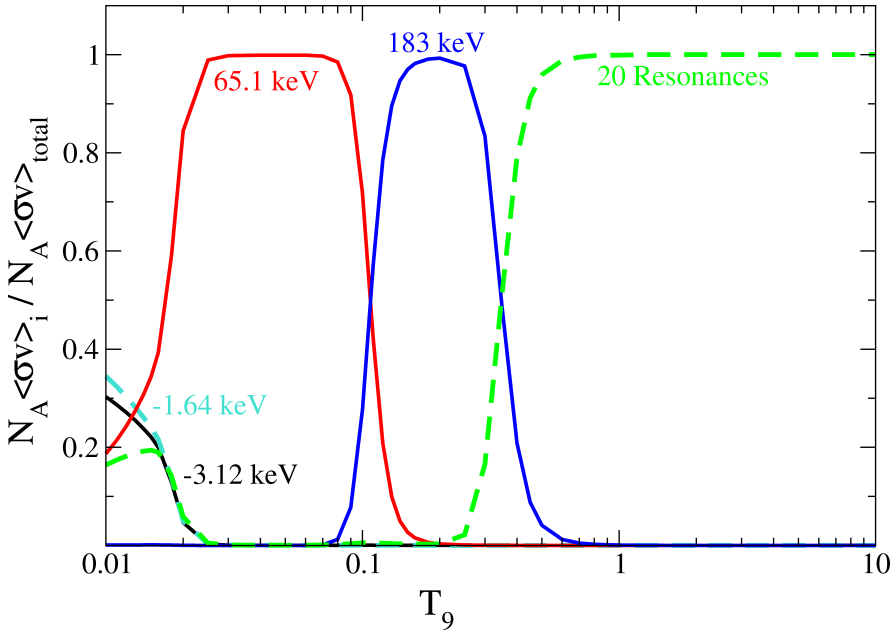

Figure 5.1: Fractional contributions to the reaction rate of ^{17}O(p,α)^{14}N, including the contributions of the 20 resonances from Tab. 5.4, the two low lying resonances and the two subthreshold resonances listed in Tabs. 5.2 and 5.3. Calculations were performed with **RatesMC** [8].

will be dominated by the individual contributions from these two resonances at these temperatures. In the range $T_9 > 0.3$, the total rate is entirely determined by the 20 higher lying resonances. The temperature is now high enough that the low lying and subthreshold resonances no longer contribute noticeably.

The lowest temperatures shown in Fig. 5.1, $T_9 < 0.02$, display a very interesting feature. Not only do the subthreshold resonances become important, the contributions from the individual resonances are all so small that the tails of the higher lying resonances also contribute significantly to the total reaction rate. The contribution of these tails would not be seen if the narrow resonant reaction rate formalism were used to calculate the rates. This is a distinct advantage of integrating over the entire Breit-Wigner energy dependence of the resonances.

5.1.4 Interference

Interference between levels of the same J^π is described in Ref. [43] by the simple equation:

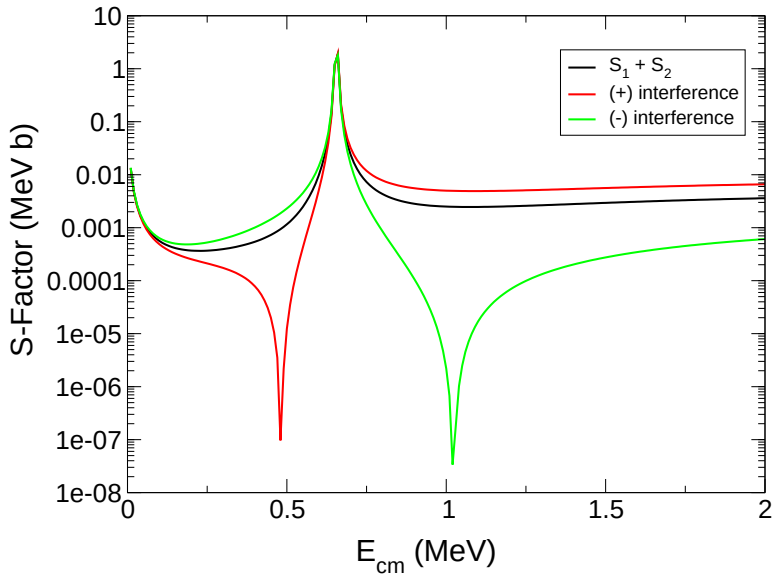

Figure 5.2: Interference between two J^{π} = 1^{+} resonances in ^{17}O(p,α)^{14}N at E_r^{cm} = -3.12 keV and 655 keV.

$$S_{total}(E) = S_1(E) + S_2(E) \pm 2\sqrt{S_1(E)S_2(E)}cos(\delta_1 - \delta_2), \tag{5.6}$$

which comes from squaring the sum of reaction amplitudes with arbitrary phases. The phase shifts of the two interfering resonances, δ_i, are given in Ref. [43] by:

$$\delta_i = tan^{-1}\left[\frac{\Gamma_i(E)}{2(E - E_{R_i})}\right], \tag{5.7}$$

with E_{r_i}, the resonance energies of the interfering resonances. The interference between two resonances may be either constructive or destructive and an experimental measurement is necessary to resolve the ambiguity. If the interference is constructive on one side of a resonance it will be destructive on the opposite side of that resonance, since the phase shift will flip signs at E = E_{r_i}.

The effects of interference on the uncertainties of the total reaction rate will be larger if the sign of the interference term is not known, since this will result in an uncertain shape for the interference S-factor. The effects of interference between five pairs of resonances on the S-factor have been plotted

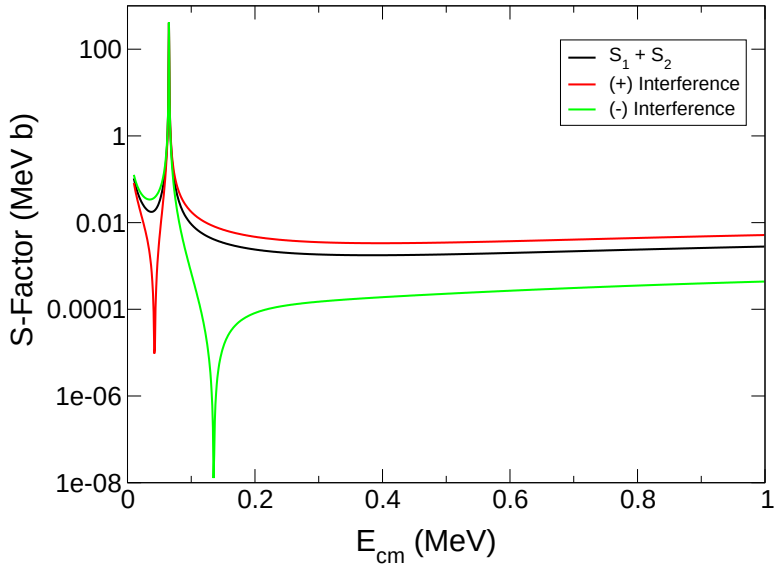

Figure 5.3: Interference between two J^{π} = 1^{-} resonances in ^{17}O(p,α)^{14}N at E_r^{cm} = -1.64 keV and 65 keV. The value of the spectroscopic factor for the subthreshold resonance is an upper limit. These curves were calculated using the upper limit value.

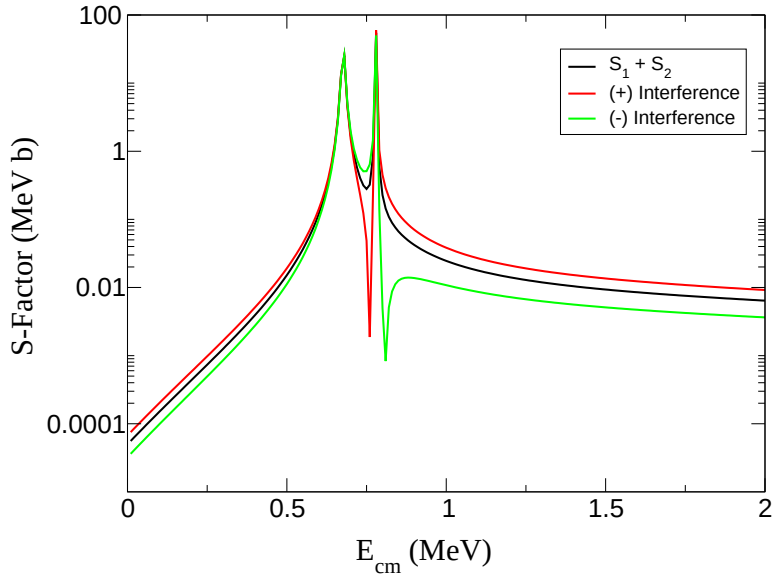

Figure 5.4: Interference between two J^{π} = 2^{+} resonances in ^{17}O(p,α)^{14}N at E_r^{cm} = 677 keV and 779 keV.

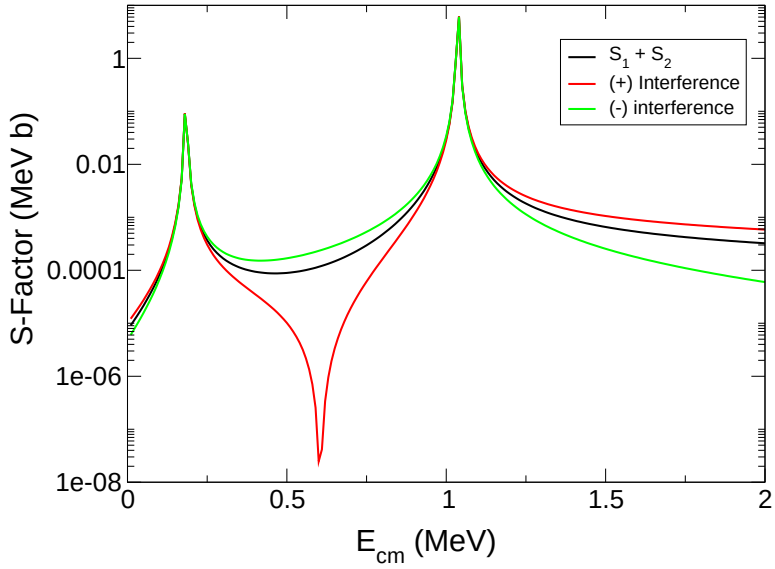

Figure 5.5: Interference between two $J^{\pi} = 2^{-}$ resonances in ^{17}O(p,α)^{14}N at E_r^{cm} = 183 keV and 1037 keV.

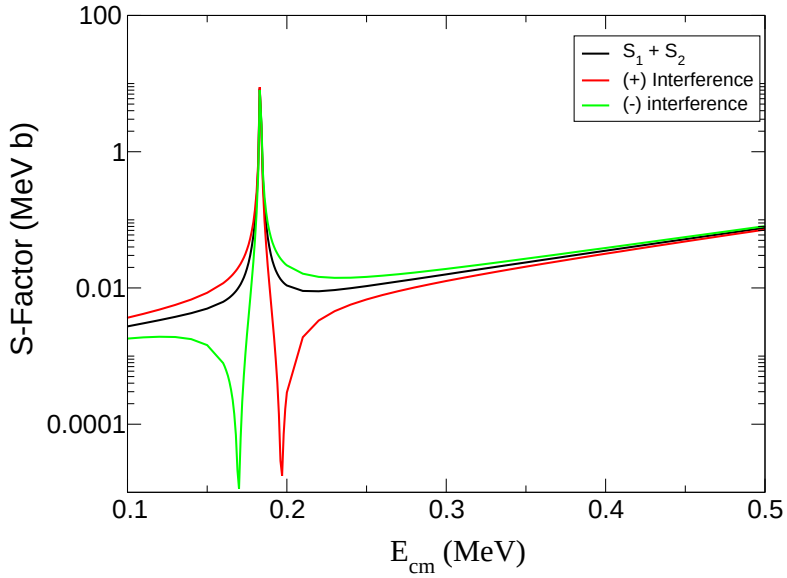

Figure 5.6: Interference between two $J^{\pi} = 2-$ resonances in ^{17}O(p,α)^{14}N at E_r^{cm} = 183 keV and 1202 keV.

in Figs. 5.2 through 5.6. There are three curves in each plot, corresponding to the S-factors for two resonances summed incoherently and the results using either the (+) or (-) interference sign in Eq. 5.6.

It is important to determine which pairs of interfering resonances will contribute significantly to the total reaction rate uncertainties. If a specific pair of resonances contributes an uncertainty which is several orders of magnitude less than the uncertainty on the total reaction rate, the interference between these resonances may be ignored and the individual contributions to the reaction rate for each of them simply summed incoherently. In order to determine the significance of the uncertainty from interference between a pair of resonances, the contribution to the total reaction rate of the two interfering resonances, including uncertainties, is calculated separately. This is then compared to the analytical reaction rate calculated assuming there are no interfering resonances. The analytical reaction rate is a simple calculation of the total reaction rate that uses the literature value for each resonance parameter without taking uncertainties or interference into account. The final recommended rate will be calculated rigorously using **RatesMC** [8], but the analytical rate was used for studying the interferences since it is very time consuming to use a Monte Carlo approach for this purpose.

Figure 5.7 (bottom panel) shows a comparison of the ^{17}O(p,α)^{14}N analytical reaction rate and the reaction rate calculated assuming that only the $J^\pi = 1^-$ resonances at E_r^{cm} = -1.64 and 65.1 keV interfere. All rates and uncertainties were divided by the analytical rate for comparison purposes. A value of $C^2S\theta_{sp}^2$ = 0.0041 was chosen for the product of the spectroscopic factor and the proton reduced width for the E_r^{cm} = -1.64 kev resonance. This is half of the upper limit value from Tab. 5.3. The interference between these two states may be an even more significant source of error in the calculation of the total reaction rate if the value is actually larger and a proper statistical distribution for this parameter will be used for the Monte Carlo rate calculation (see App. A.1).

The interference contributions shown in Figs. 5.7 and 5.8 indicate that the effects of the $J^\pi = 1^-$ resonances will dominate the reaction rate uncertainties caused by interference. This is also shown quantitatively in Tab. 5.5, where the uncertainties in the final reaction rate caused by specific interfering resonance pairs are compared as a percentage of the total analytical reaction rate at a temperature of 0.01 GK. This temperature has been chosen as a reference temperature for comparison purposes only. Of the remaining 4 pairs of interfering resonances, the $J^\pi = 2^-$ resonances at E_r^{cm} = 183 and 1203 keV contribute the most uncertainty to the total reaction rate at this temperature. Therefore, for

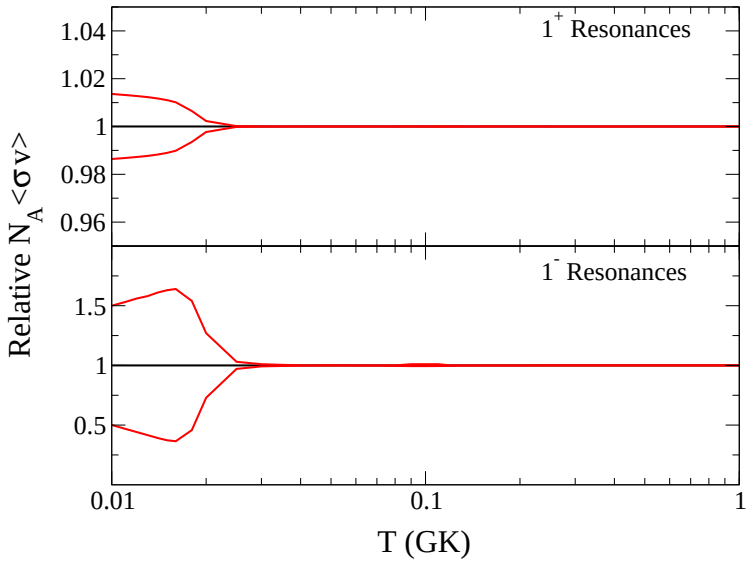

Figure 5.7: Tests of the significance of interference effects on the total reaction rate uncertainties from individual pairs of resonances. The top panel shows the reaction rate uncertainty from the interference between the J^{π} = 1^{+} resonances at E_r^{cm} = -3.1 keV and 655 keV divided by the total analytical reaction rate. The bottom panel shows the reaction rate uncertainty from the interference between the J^{π} = 1^{-} resonances at E_r^{cm} = -1.6 keV and 65.1 keV divided by the total analytical reaction rate.

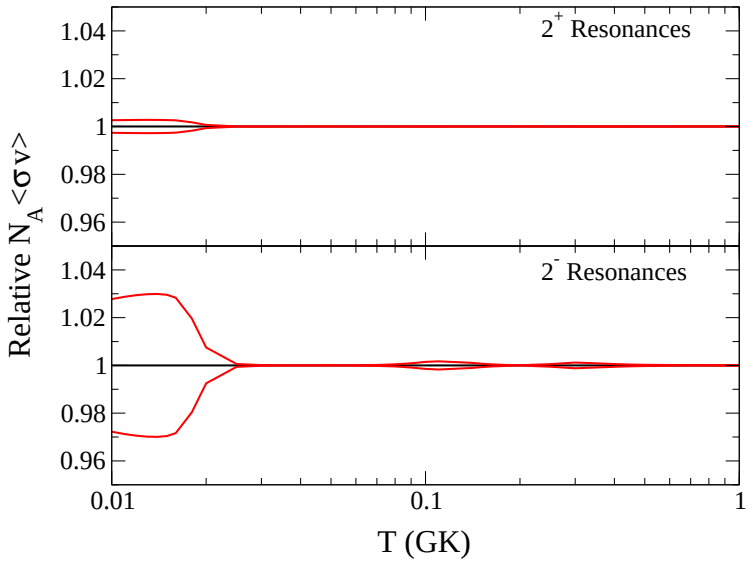

Figure 5.8: Tests of the significance of interference effects on the total reaction rate uncertainties from individual pairs of resonances. The top panel shows the reaction rate uncertainty from the interference between the $J^{\pi} = 2^{+}$ resonances at E_r^{cm} = 677 keV and 779 keV divided by the total analytical reaction rate. The bottom panel shows the reaction rate uncertainty from the interference between the $J^{\pi} = 2^{-}$ resonances at E_r^{cm} = 183 keV and 1203 keV divided by the total analytical reaction rate.

E_R^{cm} (keV)	J^π	Deviation from analytical rate
-3.12 and 655	1^+	1.36%
-1.64 and 65.1	1^-	50.1%
677 and 779	2^+	0.26%
183 and 1037	2^-	0.044%
183 and 1202.5	2^-	2.78%

Table 5.5: Effects of interference between pairs of resonances are compared to the total analytical reaction rates. The temperature of T_9 = 0.01 has been chosen as a reference for comparison between pairs of resonances. The deviation from the analytical rate is the ratio of the uncertainty in the total reaction rate from interference between the given pair of resonances to the total reaction rate calculated analytically.

the final rate calculations, only the interference between these two pairs of resonances will be considered. All other interferences between resonances will be considered insignificant for the final reaction rate of ^{17}O(p,α)^{14}N. The interference contributions are only significant below a temperature of T_9 = 0.03.

5.1.5 Total Reaction Rate for ^{17}O(p,α)^{14}N

The calculation of the total reaction rate of ^{17}O(p,α)^{14}N includes a combination of all the contributions discussed previously in this chapter. The total rate calculation is performed using **RatesMC** (see Sec. 1.5). A Porter-Thomas distribution with a mean proton reduced width of $\langle\theta^2\rangle$ = 0.05 (see appendix A.1) has been chosen to describe the the proton reduced width of the subthreshold resonance at E_r^{cm} = -1.64 keV. This resonance was not accounted for in the rate calculation of Ref. [21]. Table 5.6 gives the calculated values for the total Monte Carlo reaction rate of ^{17}O(p,α)^{14}N. The recommended rate is the median of the sampled rates. A number of 10,000 samples was chosen to ensure good statistics. The lower and upper limits listed define a 68% coverage probability. Also included in Tab. 5.6 are the lognormal parameters μ and σ for each temperature. These may be used to construct an approximate log-normal distribution describing the output rate probability density. A random variable that is made up of a sum of many contributing factors will be described by a Gaussian probability density function. Since the reaction rate is made up of a product of contributing factors, however, it should be described by a lognormal probability density function [8]. A histogram of the sample of calculated rate values for ^{17}O(p,α)^{14}N at a temperature of T_9 = 0.05 is displayed in Fig. 5.9. The

T_9	LL	Recommended	UL	μ	σ
0.010	5.04×10^{-25}	5.89×10^{-25}	6.98×10^{-25}	$-5.578\times10^{+01}$	1.66×10^{-01}
0.011	5.36×10^{-24}	6.21×10^{-24}	7.28×10^{-24}	$-5.343\times10^{+01}$	1.57×10^{-01}
0.012	4.38×10^{-23}	5.02×10^{-23}	5.85×10^{-23}	$-5.134\times10^{+01}$	1.47×10^{-01}
0.013	2.88×10^{-22}	3.30×10^{-22}	3.81×10^{-22}	$-4.946\times10^{+01}$	1.42×10^{-01}
0.014	1.60×10^{-21}	1.82×10^{-21}	2.08×10^{-21}	$-4.775\times10^{+01}$	1.35×10^{-01}
0.015	7.68×10^{-21}	8.73×10^{-21}	9.98×10^{-21}	$-4.618\times10^{+01}$	1.32×10^{-01}
0.016	3.34×10^{-20}	3.78×10^{-20}	4.31×10^{-20}	$-4.472\times10^{+01}$	1.28×10^{-01}
0.018	5.86×10^{-19}	6.78×10^{-19}	7.87×10^{-19}	$-4.183\times10^{+01}$	1.48×10^{-01}
0.020	1.28×10^{-17}	1.57×10^{-17}	1.91×10^{-17}	$-3.870\times10^{+01}$	1.98×10^{-01}
0.025	1.24×10^{-14}	1.52×10^{-14}	1.86×10^{-14}	$-3.182\times10^{+01}$	2.00×10^{-01}
0.030	1.44×10^{-12}	1.73×10^{-12}	2.08×10^{-12}	$-2.708\times10^{+01}$	1.82×10^{-01}
0.040	5.13×10^{-10}	6.05×10^{-10}	7.17×10^{-10}	$-2.123\times10^{+01}$	1.69×10^{-01}
0.050	1.61×10^{-08}	1.89×10^{-08}	2.22×10^{-08}	$-1.778\times10^{+01}$	1.64×10^{-01}
0.060	1.51×10^{-07}	1.78×10^{-07}	2.11×10^{-07}	$-1.554\times10^{+01}$	1.67×10^{-01}
0.070	7.27×10^{-07}	8.59×10^{-07}	1.02×10^{-06}	$-1.397\times10^{+01}$	1.69×10^{-01}
0.080	2.33×10^{-06}	2.77×10^{-06}	3.28×10^{-06}	$-1.280\times10^{+01}$	1.72×10^{-01}
0.090	6.04×10^{-06}	7.11×10^{-06}	8.35×10^{-06}	$-1.185\times10^{+01}$	1.62×10^{-01}
0.100	1.59×10^{-05}	1.80×10^{-05}	2.05×10^{-05}	$-1.092\times10^{+01}$	1.27×10^{-01}
0.110	4.87×10^{-05}	5.28×10^{-05}	5.75×10^{-05}	$-9.847\times10^{+00}$	8.38×10^{-02}
0.120	1.59×10^{-04}	1.68×10^{-04}	1.79×10^{-04}	$-8.689\times10^{+00}$	6.10×10^{-02}
0.130	4.83×10^{-04}	5.12×10^{-04}	5.42×10^{-04}	$-7.578\times10^{+00}$	5.76×10^{-02}
0.140	1.32×10^{-03}	1.40×10^{-03}	1.48×10^{-03}	$-6.574\times10^{+00}$	5.76×10^{-02}
0.150	3.19×10^{-03}	3.38×10^{-03}	3.58×10^{-03}	$-5.689\times10^{+00}$	5.89×10^{-02}
0.160	6.95×10^{-03}	7.36×10^{-03}	7.81×10^{-03}	$-4.911\times10^{+00}$	5.91×10^{-02}
0.180	2.52×10^{-02}	2.68×10^{-02}	2.84×10^{-02}	$-3.620\times10^{+00}$	6.00×10^{-02}
0.200	7.00×10^{-02}	7.44×10^{-02}	7.89×10^{-02}	$-2.599\times10^{+00}$	6.01×10^{-02}
0.250	4.29×10^{-01}	4.54×10^{-01}	4.81×10^{-01}	-7.891×10^{-01}	5.85×10^{-02}
0.300	$1.59\times10^{+00}$	$1.67\times10^{+00}$	$1.77\times10^{+00}$	5.155×10^{-01}	5.39×10^{-02}
0.350	$5.87\times10^{+00}$	$6.28\times10^{+00}$	$6.73\times10^{+00}$	$1.838\times10^{+00}$	6.92×10^{-02}
0.400	$2.32\times10^{+01}$	$2.55\times10^{+01}$	$2.81\times10^{+01}$	$3.240\times10^{+00}$	9.52×10^{-02}
0.450	$8.22\times10^{+01}$	$9.13\times10^{+01}$	$1.02\times10^{+02}$	$4.515\times10^{+00}$	1.07×10^{-01}
0.500	$2.41\times10^{+02}$	$2.68\times10^{+02}$	$2.99\times10^{+02}$	$5.591\times10^{+00}$	1.09×10^{-01}
0.600	$1.26\times10^{+03}$	$1.40\times10^{+03}$	$1.55\times10^{+03}$	$7.241\times10^{+00}$	1.06×10^{-01}
0.700	$4.15\times10^{+03}$	$4.58\times10^{+03}$	$5.06\times10^{+03}$	$8.430\times10^{+00}$	9.94×10^{-02}
0.800	$1.03\times10^{+04}$	$1.12\times10^{+04}$	$1.23\times10^{+04}$	$9.327\times10^{+00}$	9.24×10^{-02}
0.900	$2.09\times10^{+04}$	$2.27\times10^{+04}$	$2.48\times10^{+04}$	$1.003\times10^{+01}$	8.55×10^{-02}
1.000	$3.73\times10^{+04}$	$4.03\times10^{+04}$	$4.36\times10^{+04}$	$1.061\times10^{+01}$	7.90×10^{-02}
1.250	$1.12\times10^{+05}$	$1.19\times10^{+05}$	$1.27\times10^{+05}$	$1.169\times10^{+01}$	6.46×10^{-02}
1.500	$2.51\times10^{+05}$	$2.65\times10^{+05}$	$2.79\times10^{+05}$	$1.249\times10^{+01}$	5.40×10^{-02}
1.750	$4.76\times10^{+05}$	$4.99\times10^{+05}$	$5.22\times10^{+05}$	$1.312\times10^{+01}$	4.73×10^{-02}
2.000	$8.03\times10^{+05}$	$8.39\times10^{+05}$	$8.77\times10^{+05}$	$1.364\times10^{+01}$	4.41×10^{-02}
2.500	$(1.71\times10^{+06})$	$(1.79\times10^{+06})$	$(1.87\times10^{+06})$	$(1.440\times10^{+01})$	(4.39×10^{-02})
3.000	$(3.05\times10^{+06})$	$(3.18\times10^{+06})$	$(3.33\times10^{+06})$	$(1.497\times10^{+01})$	(4.39×10^{-02})
3.500	$(4.86\times10^{+06})$	$(5.08\times10^{+06})$	$(5.31\times10^{+06})$	$(1.544\times10^{+01})$	(4.39×10^{-02})
4.000	$(7.15\times10^{+06})$	$(7.47\times10^{+06})$	$(7.80\times10^{+06})$	$(1.583\times10^{+01})$	(4.39×10^{-02})
5.000	$(1.30\times10^{+07})$	$(1.36\times10^{+07})$	$(1.42\times10^{+07})$	$(1.642\times10^{+01})$	(4.39×10^{-02})
6.000	$(2.03\times10^{+07})$	$(2.12\times10^{+07})$	$(2.21\times10^{+07})$	$(1.687\times10^{+01})$	(4.39×10^{-02})
7.000	$(2.86\times10^{+07})$	$(2.98\times10^{+07})$	$(3.12\times10^{+07})$	$(1.721\times10^{+01})$	(4.39×10^{-02})
8.000	$(3.76\times10^{+07})$	$(3.93\times10^{+07})$	$(4.11\times10^{+07})$	$(1.749\times10^{+01})$	(4.39×10^{-02})
9.000	$(4.71\times10^{+07})$	$(4.93\times10^{+07})$	$(5.15\times10^{+07})$	$(1.771\times10^{+01})$	(4.39×10^{-02})
10.000	$(5.91\times10^{+07})$	$(6.18\times10^{+07})$	$(6.45\times10^{+07})$	$(1.794\times10^{+01})$	(4.39×10^{-02})

Table 5.6: Reaction rates for ^{17}O(p,α)^{14}N calculated using the Monte Carlo code, **RatesMC** [8]. The recommended rate is the median of the sampled distribution; μ and σ are the parameters of a log-normal distribution approximating the sampled distribution. The rates were matched to Hauser-Feshbach rates adopted from Ref. [12] at 2.115 GK (see Chap. 2 for matching procedure)

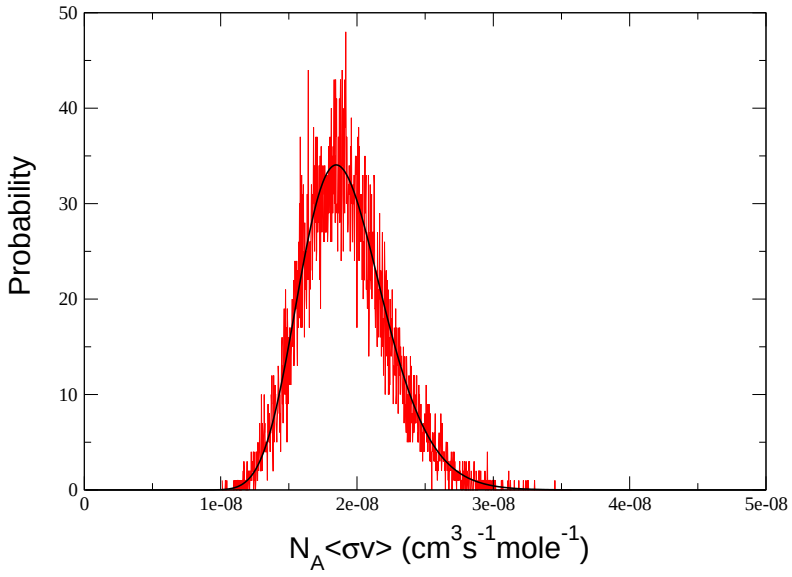

Figure 5.9: Histogram of the distribution of reaction rates calculated using the Monte Carlo code, **RatesMC** [8] for T_9 = 0.05. The histogram is overlayed by a lognormal distribution with parameters of μ = -1.78 and σ = 0.164 taken from Tab. 5.6

black curve represents a log-normal distribution with μ = -17.78 and σ = 0.164, as listed in Tab. 5.6. The lognormal approximation is a very good description of the Monte Carlo distribution. Similar results are found at all other temperatures.

Figure 5.10 displays a comparison between the rates calculated in the present work and those presented in Ref. [21]. There are two interesting aspects. First, at low Temperatures ($T_9 < 0.02$) the new rates are much larger and have a much larger uncertainty than those presented in Ref. [21]. This results from including the subthreshold resonance at E_r^{cm} = -1.64 keV, which was disregarded in Ref. [21]. Interference effects were also taken into account here and these were shown to be important at temperatures below T_9 = 0.03 (see Sec. 5.1.4). Both of these effects will contribute to the discrepancies between these two sets of reaction rates. The second effect is that the rates diverge at the highest temperatures shown ($T_9 > 1.0$). This discrepancy is caused by the fact that the present calculation includes all the levels listed in Tab. 5.4, while the rates from Ref. [21] include only those resonances listed in Tab. 5.1. The resonances that are not included in Tab. 5.1 but are taken into

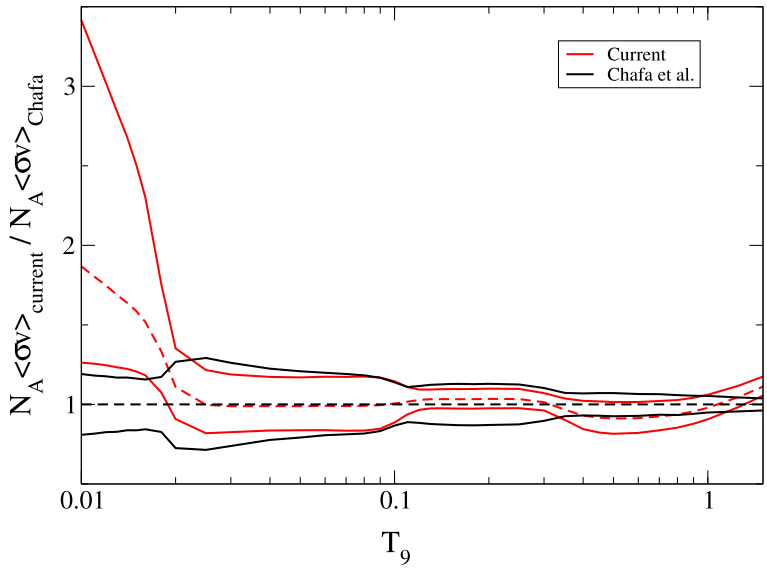

Figure 5.10: Comparison of the total reaction rate of ^{17}O(p,α)^{14}N calculated in the present work, compared to those presented in Reference [21]. All reaction rates and upper and lower limits were normalized to the recommended rates from Ref. [21]

account in Tab. 5.4 are all located at higher excitation energies.

5.2 The ^{17}O(p,γ)^{18}F Reaction Rate

New reaction rates for ^{17}O(p,γ)^{18}F can be calculated using the newly measured direct capture S-factor presented in Chap. 4. These reaction rates will be calculated following the same procedure used for calculating the rates of ^{17}O(p,α)^{14}N presented in Sec. 5.1.5. First, accurate values for all of the known resonance parameters must be compiled from the literature and used to make an input file for the Monte Carlo reaction rate code. These will be combined with the new direct capture S-factor and new reaction rates will be presented.

5.2.1 Narrow Resonances in ^{17}O(p,γ)^{18}F

There are several narrow resonances which contribute to the reaction rate of ^{17}O(p,γ)^{18}F, but there are problems with the values of the resonance strengths quoted in the literature. As discussed in Ref.

Resonances in ^{17}O(p,α)^{14}N		
E_R^{CM} (keV)	$\omega\gamma_{p\gamma}$ (eV)	
	Rolfs renormalized	Sens
489.9±1.2	0.013±0.0016	0.0068±0.0013
530.0±0.6	0.110±0.025	0.079±0.015
556.7±1.0	0.335±0.075	0.235±0.044
633.9±0.9	0.160±0.026	0.14±0.20
676.7±1.0	0.455±0.094	0.287±0.053
704.0±0.9	0.0320±0.0071	0.0252±0.0049
779.0±1.8	0.0300±0.0078	0.0216±0.044
878.4±1.6	0.0180±0.0070	0.0127±0.0041
1037.2±0.9	0.215±0.051	0.165±0.033
1170.5±1.5	0.140±0.028	0.071±0.013
1196.6±1.6	0.0270±0.0092	0.0205±0.0047
1270.9±1.8	0.0500±0.0186	0.0193±0.0052

Table 5.7: Literature values for narrow resonances used in ^{17}O(p,γ)^{18}F. Resonance energies are taken from Ref. [33] and strengths are from Ref. [34, 44].

[7], the $\omega\gamma_{p\gamma}$ values quoted in Ref. [6] are normalized to an incorrect strength of the E_r^{cm} = 633 keV in ^{27}Al(p,γ)^{28}Si. The strengths were normalized to a value of $\omega\gamma_{p\gamma}$ = 0.44 $\pm$ 0.07 eV, while the correct value taken from Ref. [13] is $\omega\gamma_{p\gamma}$ = 0.264 $\pm$ 0.016 eV. The data from Ref. [6] need to be renormalized to the correct strength. These renormalized values are listed in Tab. 5.7. Also included in Tab. 5.7 are the resonance strengths measured by Sens et al. [44]. For each of the resonances listed, the strengths are systematically lower in Ref. [44] than the renormalized values of Ref. [34]. Fox et al. [7] used an average of the two strengths and Chafa et al. [21] used a weighted average for the final resonance strengths. The experiment presented in Chap. 4 included measured resonance strengths for both the E_r^{cm} = 144 keV in ^{18}O(p,γ)^{19}F and the E_r^{cm} = 490 keV resonance in ^{17}O(p,γ)^{18}F. The result for the E_r^{cm} = 144 keV resonance strength from the present work is in agreement with the literature [1]. The renormalized strength of Rolfs et al. [34] for the E_r^{cm} = 490 keV is in agreement with the present measurement of this resonance (see Sec. 4.2.3). For these reasons, the resonance strengths of Ref. [44] will be disregarded for the purposes of calculating the reaction rate of ^{17}O(p,γ)^{18}F.

5.2.2 Broad and Interfering Resonances

Each of the resonances included in Tab. 5.7 will be treated as narrow except the E_r^{cm} = 556.7 keV, 676.7 keV and 1037.2 keV resonances. The width of these resonances requires the inclusion of the energy dependence of their cross sections in the integration of the reaction rate. The particle partial widths Γ_p and Γ_α for each of these states can be found in Tab. 5.2 and the γ-ray partial widths, Γ_γ, can be easily derived using their respective resonance strengths listed in Tab. 5.7. This results in final values of Γ_γ = 0.57$\pm$0.13 eV, 1.09$\pm$0.23 eV and 0.84$\pm$0.20 eV for the above resonances, respectively.

Interference effects are considered for three pairs of resonances: the 1^- resonances at E_r^{cm} = -1.6 and 65 keV, the 2^- resonances at E_r^{cm} = 183 and 1037 keV, and the 2^+ resonances at E_r^{cm} = 677 and 779 keV. The partial widths for the two subthreshold resonances and the E_r^{cm} = 65 keV resonance can be found in Sec. 5.1.2. Recall that the proton partial width, Γ_p, for the subthreshold resonance at E_r^{cm} = -65 keV is an upper limit value and its treatment is specifically addressed in Sec. 5.1.2.

5.2.3 Total Reaction Rate for ^{17}O(p,γ)^{18}F

Combining the resonance strengths for the narrow resonances in Tab. 5.7 and the partial widths listed above, the total reaction rates for ^{17}O(p,γ)^{18}F can now be calculated using the Monte Carlo procedure. The results are presented in Tab. 5.8.

The new rates for the ^{17}O(p,γ)^{18}F reaction are compared to the rates calculated by Chafa et al. [21] in the top panel of Fig. 5.11. Notice that for the peak temperature range important to classical novae (T = 0.1 -0.4 GK) the reaction rate has a significantly smaller uncertainty and is lower than that of Ref. [21]. This is a result of using a smaller direct capture contribution from the present work that has a factor of two smaller uncertainty than that of Chafa et al. [21]. This is discussed in detail in Sec. 4.3.5. At low temperatures the present rate is consistent with the recommended rate of Ref. [21]. The uncertainty on the total reaction rate, however, is significantly smaller. This is again a result of the dominance of the direct capture contribution below T = 0.03 GK (see Fig. 9 from Ref. [7]). At high temperatures (T $>$ 0.4 GK) the rate is dominated by the contribution of resonances with $E_r^{cm} \geq$ 489 keV. The present rates are higher than those of Ref. [21] because the renormalized strengths of Rolfs et al. [34] were used here. The bottom panel of Fig. 5.11 shows a comparison of the current reaction

T_9	LL	Recommended	UL	μ	σ
0.010	2.95×10^{-25}	3.58×10^{-25}	4.38×10^{-25}	$-5.629\times10^{+01}$	2.02×10^{-01}
0.011	3.10×10^{-24}	3.78×10^{-24}	4.64×10^{-24}	$-5.393\times10^{+01}$	2.01×10^{-01}
0.012	2.51×10^{-23}	3.09×10^{-23}	3.81×10^{-23}	$-5.183\times10^{+01}$	2.08×10^{-01}
0.013	1.64×10^{-22}	1.99×10^{-22}	2.45×10^{-22}	$-4.996\times10^{+01}$	2.03×10^{-01}
0.014	8.83×10^{-22}	1.08×10^{-21}	1.33×10^{-21}	$-4.827\times10^{+01}$	2.05×10^{-01}
0.015	4.08×10^{-21}	4.98×10^{-21}	6.14×10^{-21}	$-4.675\times10^{+01}$	2.07×10^{-01}
0.016	1.65×10^{-20}	2.02×10^{-20}	2.50×10^{-20}	$-4.534\times10^{+01}$	2.05×10^{-01}
0.018	1.98×10^{-19}	2.42×10^{-19}	2.96×10^{-19}	$-4.287\times10^{+01}$	2.03×10^{-01}
0.020	1.69×10^{-18}	2.06×10^{-18}	2.51×10^{-18}	$-4.072\times10^{+01}$	1.99×10^{-01}
0.025	1.67×10^{-16}	1.97×10^{-16}	2.32×10^{-16}	$-3.616\times10^{+01}$	1.62×10^{-01}
0.030	8.35×10^{-15}	9.69×10^{-15}	1.12×10^{-14}	$-3.227\times10^{+01}$	1.46×10^{-01}
0.040	2.13×10^{-12}	2.47×10^{-12}	2.88×10^{-12}	$-2.672\times10^{+01}$	1.53×10^{-01}
0.050	6.56×10^{-11}	7.62×10^{-11}	8.88×10^{-11}	$-2.330\times10^{+01}$	1.52×10^{-01}
0.060	6.61×10^{-10}	7.66×10^{-10}	8.88×10^{-10}	$-2.099\times10^{+01}$	1.48×10^{-01}
0.070	3.61×10^{-09}	4.13×10^{-09}	4.76×10^{-09}	$-1.930\times10^{+01}$	1.40×10^{-01}
0.080	1.38×10^{-08}	1.58×10^{-08}	1.79×10^{-08}	$-1.797\times10^{+01}$	1.32×10^{-01}
0.090	4.31×10^{-08}	4.93×10^{-08}	5.66×10^{-08}	$-1.682\times10^{+01}$	1.37×10^{-01}
0.100	1.21×10^{-07}	1.39×10^{-07}	1.61×10^{-07}	$-1.579\times10^{+01}$	1.44×10^{-01}
0.110	3.13×10^{-07}	3.64×10^{-07}	4.25×10^{-07}	$-1.482\times10^{+01}$	1.54×10^{-01}
0.120	7.69×10^{-07}	9.02×10^{-07}	1.07×10^{-06}	$-1.391\times10^{+01}$	1.64×10^{-01}
0.130	1.78×10^{-06}	2.11×10^{-06}	2.52×10^{-06}	$-1.306\times10^{+01}$	1.75×10^{-01}
0.140	3.87×10^{-06}	4.65×10^{-06}	5.65×10^{-06}	$-1.227\times10^{+01}$	1.92×10^{-01}
0.150	7.96×10^{-06}	9.65×10^{-06}	1.19×10^{-05}	$-1.154\times10^{+01}$	2.03×10^{-01}
0.160	1.53×10^{-05}	1.87×10^{-05}	2.33×10^{-05}	$-1.088\times10^{+01}$	2.16×10^{-01}
0.180	4.85×10^{-05}	5.99×10^{-05}	7.57×10^{-05}	$-9.710\times10^{+00}$	2.30×10^{-01}
0.200	1.29×10^{-04}	1.60×10^{-04}	2.02×10^{-04}	$-8.729\times10^{+00}$	2.32×10^{-01}
0.250	8.64×10^{-04}	1.05×10^{-03}	1.32×10^{-03}	$-6.841\times10^{+00}$	2.21×10^{-01}
0.300	3.89×10^{-03}	4.61×10^{-03}	5.57×10^{-03}	$-5.371\times10^{+00}$	1.84×10^{-01}
0.350	1.64×10^{-02}	1.87×10^{-02}	2.15×10^{-02}	$-3.974\times10^{+00}$	1.37×10^{-01}
0.400	6.87×10^{-02}	7.71×10^{-02}	8.69×10^{-02}	$-2.561\times10^{+00}$	1.18×10^{-01}
0.450	2.53×10^{-01}	2.85×10^{-01}	3.22×10^{-01}	$-1.253\times10^{+00}$	1.21×10^{-01}
0.500	7.85×10^{-01}	8.86×10^{-01}	$1.01\times10^{+00}$	-1.186×10^{-01}	1.26×10^{-01}
0.600	$4.59\times10^{+00}$	$5.20\times10^{+00}$	$5.94\times10^{+00}$	$1.651\times10^{+00}$	1.29×10^{-01}
0.700	$1.65\times10^{+01}$	$1.87\times10^{+01}$	$2.13\times10^{+01}$	$2.932\times10^{+00}$	1.28×10^{-01}
0.800	$4.31\times10^{+01}$	$4.88\times10^{+01}$	$5.55\times10^{+01}$	$3.889\times10^{+00}$	1.26×10^{-01}
0.900	$9.03\times10^{+01}$	$1.02\times10^{+02}$	$1.15\times10^{+02}$	$4.626\times10^{+00}$	1.22×10^{-01}
1.000	$1.62\times10^{+02}$	$1.82\times10^{+02}$	$2.06\times10^{+02}$	$5.206\times10^{+00}$	1.22×10^{-01}
1.250	$4.49\times10^{+02}$	$5.02\times10^{+02}$	$5.66\times10^{+02}$	$6.222\times10^{+00}$	1.15×10^{-01}
1.500	$8.59\times10^{+02}$	$9.59\times10^{+02}$	$1.08\times10^{+03}$	$6.868\times10^{+00}$	1.13×10^{-01}
1.750	$1.33\times10^{+03}$	$1.48\times10^{+03}$	$1.66\times10^{+03}$	$7.305\times10^{+00}$	1.10×10^{-01}
2.000	$1.82\times10^{+03}$	$2.02\times10^{+03}$	$2.25\times10^{+03}$	$7.613\times10^{+00}$	1.07×10^{-01}
2.500	$2.69\times10^{+03}$	$2.99\times10^{+03}$	$3.32\times10^{+03}$	$8.004\times10^{+00}$	1.05×10^{-01}
3.000	$3.38\times10^{+03}$	$3.74\times10^{+03}$	$4.13\times10^{+03}$	$8.227\times10^{+00}$	1.02×10^{-01}
3.500	$3.85\times10^{+03}$	$4.25\times10^{+03}$	$4.71\times10^{+03}$	$8.356\times10^{+00}$	9.98×10^{-02}
4.000	$4.14\times10^{+03}$	$4.56\times10^{+03}$	$5.03\times10^{+03}$	$8.425\times10^{+00}$	9.86×10^{-02}
5.000	$4.33\times10^{+03}$	$4.78\times10^{+03}$	$5.26\times10^{+03}$	$8.471\times10^{+00}$	9.55×10^{-02}
6.000	$4.24\times10^{+03}$	$4.66\times10^{+03}$	$5.14\times10^{+03}$	$8.449\times10^{+00}$	9.60×10^{-02}
7.000	$4.04\times10^{+03}$	$4.44\times10^{+03}$	$4.90\times10^{+03}$	$8.400\times10^{+00}$	9.72×10^{-02}
8.000	$3.80\times10^{+03}$	$4.18\times10^{+03}$	$4.61\times10^{+03}$	$8.340\times10^{+00}$	9.59×10^{-02}
9.000	$3.58\times10^{+03}$	$3.93\times10^{+03}$	$4.32\times10^{+03}$	$8.276\times10^{+00}$	9.56×10^{-02}
10.000	$3.34\times10^{+03}$	$3.68\times10^{+03}$	$4.04\times10^{+03}$	$8.211\times10^{+00}$	9.47×10^{-02}

Table 5.8: Reaction rates of ^{17}O(p,γ)^{18}F calculated using the Monte Carlo code, **RatesMC** [8]. The recommended rate is the median of the sampled distribution; μ and σ are the parameters of a log-normal distribution approximating the sampled distribution.

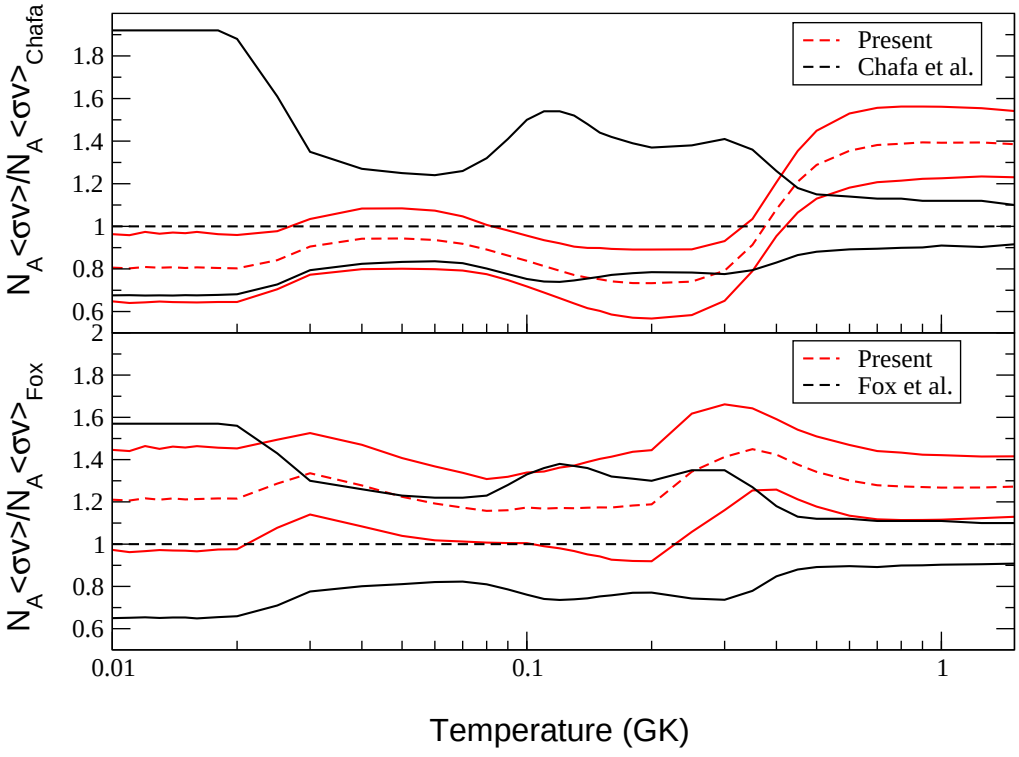

Figure 5.11: (bottom panel)Comparison of the present total reaction rates of ^{17}O(p,γ)^{18}F with those presented in Ref. [7]. All reaction rates and upper and lower limits were divided by the recommended rates from Ref. [7]. (top panel) Comparison of the present total reaction rates of ^{17}O(p,γ)^{18}F with those presented in Ref. [21]. All reaction rates and upper and lower limits were divided by the recommended rates from Ref. [21]

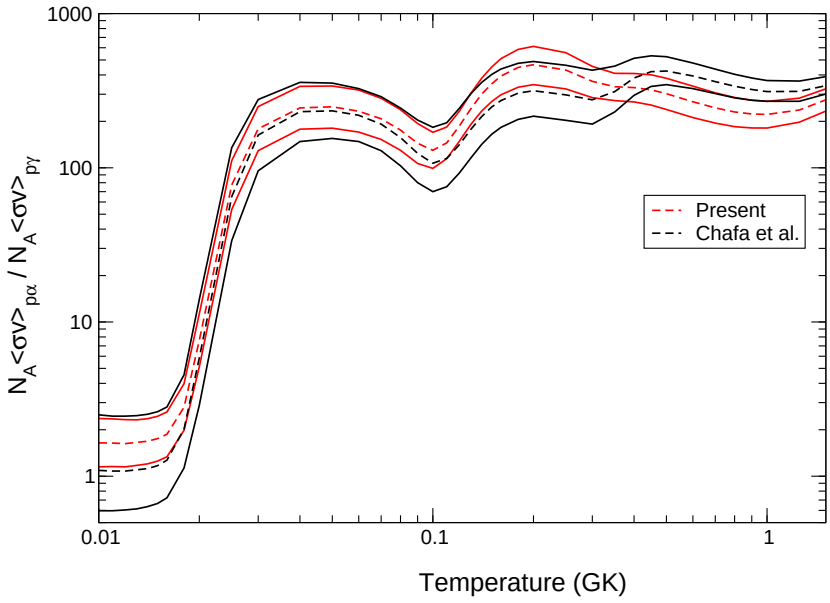

Figure 5.12: Comparison of the ratio of ^{17}O(p,α)^{14}N to ^{17}O(p,γ)^{18}F rates calculated in the present work to those from Chafa et al. [21]

rate and the rate of Fox et al. [7]. In the temperature regions where the contribution of direct capture dominates, the two reaction rates are in agreement, though the present rates have smaller uncertainties than those of Ref. [7]. The present rates are again larger at high temperature because of the use of the renormalized resonance strengths from Rolfs [34] for the high energy resonances.

Figure 5.12 shows a comparison of the ratio of reaction rates for the ^{17}O(p,α)^{14}N to the ^{17}O(p,γ)^{18}F reaction, derived from the present work and from Chafa et al. [21]. There are several interesting features to notice. First, the uncertainties on the present rate ratio are smaller at all temperatures than those from Ref. [21]. This is a result of a more precise direct capture contribution and the inclusion of more ^{17}O(p,γ)^{18}F resonances, along with a more reliable Monte Carlo method of reaction rate calculations. Another feature is that the new ratio never falls below unity at low temperatures. A ratio below unity is not ruled out by Chafa et al [21]. This finding is important for stellar nucleosynthesis because it means that the ^{17}O(p,α)^{14}N rate is always stronger than the ^{17}O(p,γ)^{18}F rate. The present ratio is higher at nova temperatures, including a factor of 1.5 greater at T = 0.2 GK, as a result of

the smaller direct capture contribution to the ^{17}O(p,γ)^{18}F reaction rate. It is important to note that the reduction in the present uncertainties, however, is far more important, because this will allow for better constraint of classical nova simulations. There is also a small dip in the present ratio at the highest temperatures as a result of the decrease in the ^{17}O(p,γ)^{18}F reaction rate seen in Fig. 5.11.

The new reaction rates derived in the present work will be submitted for publication in the near future.

6 Summary and Conclusion

Classical novae are explosive binary stellar systems with peak temperatures of T = 0.1 - 0.4 GK. They involve the accretion of hydrogen rich material from a main sequence star onto the surface of a small, dense white dwarf partner. Studies of the nova ejecta give information of both the underlying white dwarf and the path of nucleosynthesis in these systems. Observed elemental abundances from the ejecta serve as much needed constraints for the modeling of these explosions. Classical novae are also thought to be the most bountiful source of ^{15}N, ^{17}O and perhaps ^{13}C in the universe [18]. Short-lived ^{18}F, which emits β-decay radiation, is also produced in novae and may be observable when the envelope becomes transparent. These 511 keV γ-rays can be detected, providing more constraints for nova simulations. These explosive environments involve hundreds of nuclear reactions that are accounted for when modeling the nucleosynthesis. Only a restricted number of these nuclear reactions actually substantially affect nucleosynthesis in these environments. The ^{17}O(p,γ)^{18}F and ^{17}O(p,α)^{14}N reactions have an important effect on nucleosynthesis in classical novae, since they determine the destruction of ^{17}O and the production of ^{18}F. For instance, the greater the ^{17}O(p,γ)^{18}F rate, the higher the ^{18}F abundance produced. The greater ^{17}O(p,α)^{14}N reaction, however, the lower the relative abundance of ^{18}F to CNOI elements produced. The quality of the reaction rates of these two ^{17}O + p reactions have been vastly improved as a result of the current work.

The E_r^{lab} = 193 keV resonance in ^{17}O(p,γ)^{18}F has been the object of recent contention in the literature with a disagreement in measured strengths presented by Fox et al. [18] of $\omega\gamma_{p\gamma}$ = (1.2 $\pm$ 0.2)$\times 10^{-6}$ eV and Chafa et al. [21] of $\omega\gamma_{p\gamma}$ = (2.2 $\pm$ 0.4)$\times 10^{-6}$ eV. The dominant contribution to this reaction rate, however, comes from the direct capture process. The values in the published literature for the direct capture cross section differ by a factor of two [6, 7]. A measurement of the direct capture of ^{17}O(p,γ)^{18}F at energies of $E_p^{lab} < 500$ keV has been presented in Chap. 4 and the

results have already been submitted for publication [28]. This experiment reached an energy of $E_p^{cm} \approx$ 250 keV, just inside the Gamow peak for nova temperatures. The resulting direct capture S-factor of S(E) = 4.6 $\pm$ 1.1 keV b is a factor of two lower than the original value of Rolfs [6] and agrees with the calculated predictions of Fox et al. [7]. Experimental uncertainties ($\pm$ 23%) of the direct capture S-factor have been established for the first time. The improved uncertainty has a marked effect on the final reaction rate, which is discussed in detail in Chap. 5.

For the competing ^{17}O(p,α)^{14}N reaction, the E_r^{lab} = 193 keV resonance is the only notable contributor to the reaction rate at nova conditions. This resonance was first measured by Chafa et al. [19]. A remeasurement of this resonance using anodized instead of the implanted targets of Ref. [19] is presented in Chap. 3 and this work has already been published in Ref. [27]. This resulted in a resonance strength of $\omega\gamma_{p\alpha}$ = (1.66 $\pm$ 0.17)$\times 10^{-3}$ eV [27], which is in agreement with the measurement of Ref. [19]. Subsequently, this resonance strength was remeasured using a completely different technique at ORNL and their result also confirmed the original measurement of Ref. [19].

A new method for extrapolating experimental reaction rates to high stellar temperatures has been presented in Chap. 2 and the results have been published in Refs. [15, 16]. This new method illuminates some flaws of current matching procedures used in nuclear astrophysics and further explains the shortcomings of the Gamow peak concept when applied to narrow resonances. It is shown that this concept breaks down at high temperatures, which is precisely the region over which most laboratory rates need to be extrapolated. This new procedure, based on the statistical distribution of fractional rate contributions, provides a proper description of the energy burning region at all temperatures and should replace the previous method for determining a matching temperature.

The dominant rate contributions at nova temperatures for both the ^{17}O(p,α)^{14}N reaction and ^{17}O(p,γ)^{18}F reaction have been successfully measured in the current work. These results have been used in combination with a Monte Carlo code in order to estimate new reaction rates. The new rates for ^{17}O(p,γ)^{18}F and ^{17}O(p,α)^{14}N are presented in Chap. 5. The (p,α) rate has been found to be significantly higher at low temperatures compared to the results of Ref. [21] and the rate uncertainties in the temperature range of interest for classical novae have been improved by a factor of $\approx$ 2. The (p,γ) reaction rates have remarkably improved uncertainties compared to literature rates [7, 21].

Given these considerable improvements, the next obvious step will be to perform new hydrody-

namical nova simulations using the current ^{17}O + p reaction rates. This will allow for more accurate nucleosynthesis results, which should significantly affect the understanding of the destruction of ^{17}O and production of ^{18}F in classical novae. Preparations for these simulations are underway and results will be provided in the near future.

A Appendix

A.1 Probability Density Function for the Spectroscopic Factor

Often it is the case that the only available literature data for the γ-ray or particle partial width of a known nuclear level is an upper limit. It is not statistically correct to assume that the true value is equally likely to be any result below the upper limit. Instead, recall from Eq. 1.25 that the particle partial width can be found from the spectroscopic factor, S. The spectroscopic factor describes the relative probability that a compound nucleus can be described by an individual single particle state [1]. The spectroscopic factor is made up of the square of an amplitude which is proportional to a matrix element of the nuclear Hamiltonian [8]. These matrix elements form a Gaussian probability density function centered around zero. The Gaussian distribution for the matrix elements, M, has the form

$$f(M) = \frac{1}{\sqrt{2\pi\sigma^2}} \exp\left(-\frac{M^2}{2\sigma^2}\right). \tag{A.1}$$

The probability density function for the spectroscopic factor, S $\propto M^2$, can be easily derived from the Gaussian distribution of the nuclear matrix elements, M. For a Gaussian distribution centered around zero, the mean of the distribution is $\langle M \rangle = 0$ and the variance will be $\sigma^2 = \langle M^2 \rangle - \langle M \rangle^2 = \langle M^2 \rangle$. Consider a change in variables from $f(M)dM$ to $g(S)dS$. We have S $= kM^2$, where k is a proportionality constant. This gives $dM = \frac{1}{2k\sqrt{S}} dS$. Rewriting $f(M)$ in terms of S gives the new form

$$f(M)dM = \frac{1}{\sqrt{2\pi\sigma^2}} \exp\left(-\frac{M^2}{2\sigma^2}\right) dM = \frac{C}{\sqrt{S}} \exp\left(-\frac{S}{2k\sigma^2}\right) dS = g(S)dS. \tag{A.2}$$

Substituting the known variance of the original Gaussian, the final function of S becomes

$$g(S) = \frac{C}{\sqrt{S}} \exp\left(-\frac{S}{2\langle S \rangle}\right). \tag{A.3}$$

This makes use of the identity $\langle S \rangle = k\langle M^2 \rangle$ and a constant, C. $g(S)$ is a chi-squared distribution with one degree of freedom, also known as the Porter-Thomas distribution. This is the functional

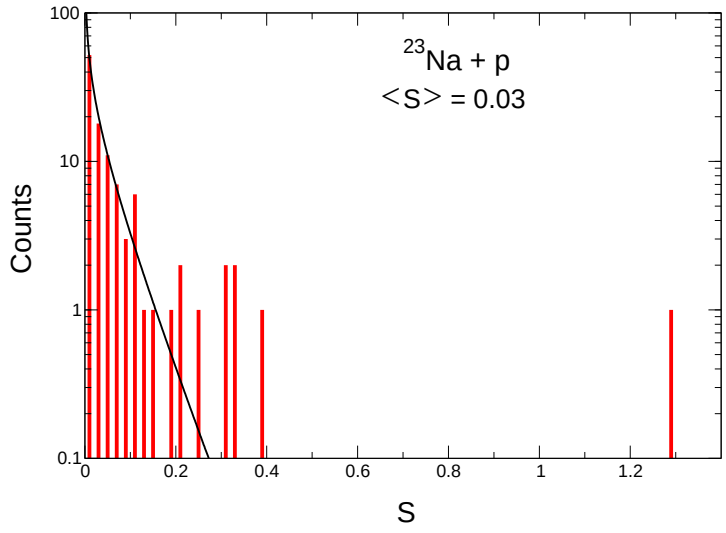

Figure A.1: Histogram of measured proton spectroscopic factors in ^{24}Mg. The solid line is a Porter-Thomas fit to the data resulting in a distribution mean of $\langle S \rangle = 0.03$. Data taken from Refs. [45, 46]

dependence of the spectroscopic factors for a given nucleus and exit channel. It is clear that this distribution highly favors spectroscopic factors with very low values. These low values are the most difficult to measure experimentally. This results in experimental data sets that are highly skewed toward larger values of the mean. It is very important to develop an accurate procedure for describing the distribution of spectroscopic factors, so that they may be properly sampled by the Monte Carlo procedure when accounting for an unknown spectroscopic factor.

The rest of this section is dedicated to determining a Porter-Thomas fit to the known spectroscopic factors for unbound levels in six different nuclei. The final goal is to determine the mean, $\langle S \rangle$, of a Porter-Thomas distribution that may be used to randomly sample the proton spectroscopic factor of an unknown level in ^{18}F. Since there are not sufficient measured spectroscopic factor values available for ^{18}F, it is necessary to look to other nuclei. Mitchell et al. have done extensive studies on the proton spectroscopic factors of ^{24}Mg, ^{28}Si, ^{30}P, ^{32}S, ^{36}Ar, and ^{40}Ca. These data sets will be fit in order to accurately describe the distribution of proton spectroscopic factors for the levels in these nuclei and to estimate a value for a given level in ^{18}F.

Figures A.1 - A.6 display histograms of the proton spectroscopic factors for six different nuclei.

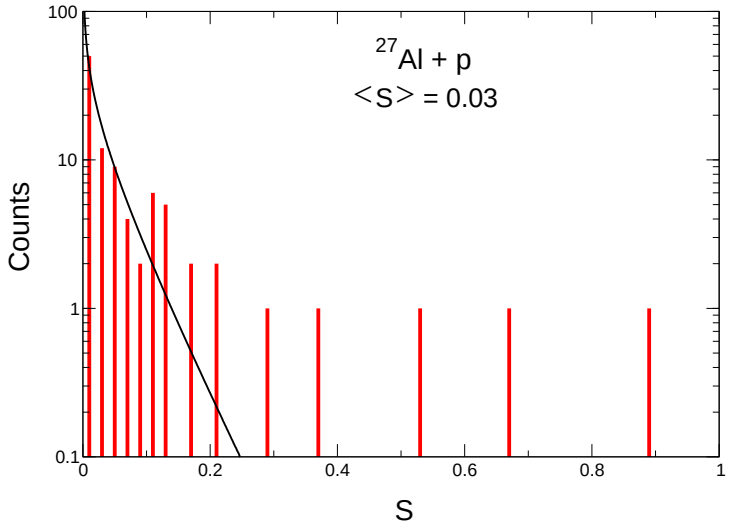

Figure A.2: Histogram of measured proton spectroscopic factors in ^{28}Si. The solid line is a Porter-Thomas fit to the data resulting in a distribution mean of $\langle S \rangle = 0.03$. Data taken from Refs. [47]

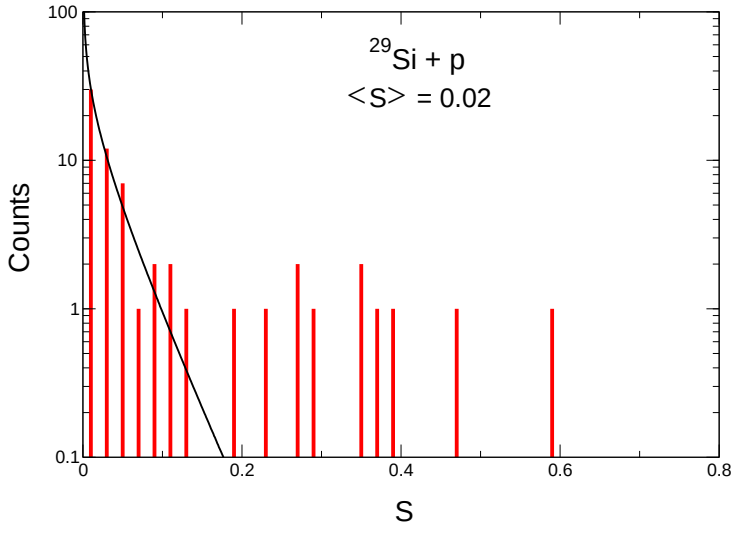

Figure A.3: Histogram of measured proton spectroscopic factors in ^{30}P. The solid line is a Porter-Thomas fit to the data resulting in a distribution mean of $\langle S \rangle = 0.02$. Data taken from Refs. [47, 48, 49]

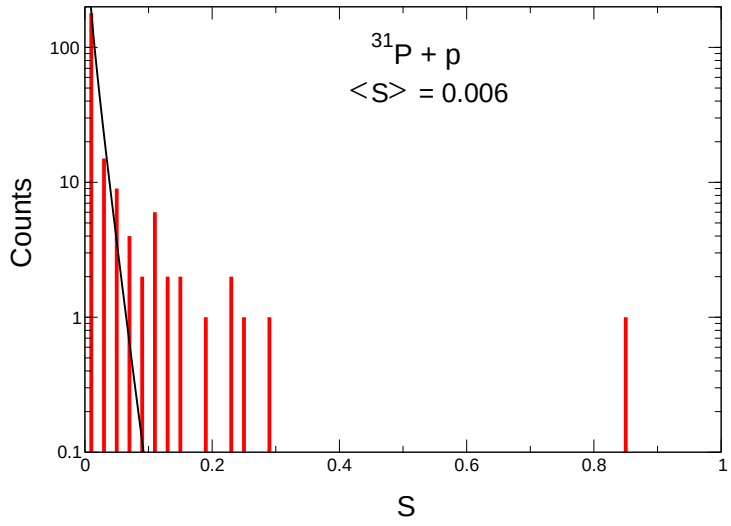

Figure A.4: Histogram of measured proton spectroscopic factors in ^{32}S. The solid line is a Porter-Thomas fit to the data resulting in a distribution mean of $\langle S \rangle = 0.006$. Data taken from Refs. [50, 51]

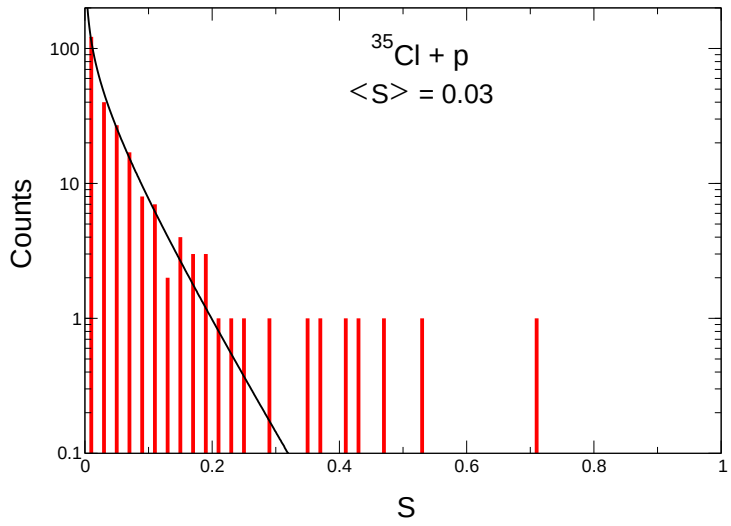

Figure A.5: Histogram of measured proton spectroscopic factors in ^{36}Ar. The solid line is a Porter-Thomas fit to the data resulting in a distribution mean of $\langle S \rangle = 0.03$. Data taken from Refs. [52]

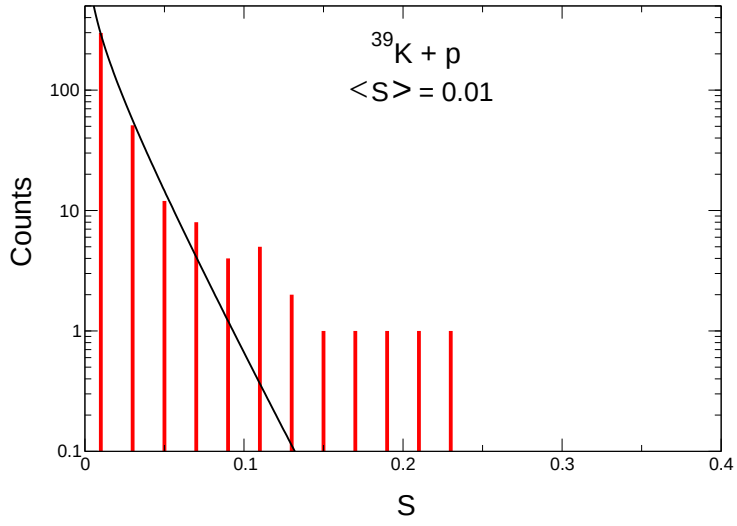

Figure A.6: Histogram of measured proton spectroscopic factors in ^{40}Ca. The solid line is a Porter-Thomas fit to the data resulting in a distribution mean of $\langle S \rangle = 0.01$. Data taken from Refs. [53]

Included in each plot is a Porter-Thomas fit to the spectroscopic factor data. This fit determines the best value for the mean of the distribution describing these data. It is important to note that the Porter-Thomas distribution describes the probability density function for a given nucleus and specific set of quantum numbers. The data that were fit, however, constitute a combination of levels with different orbital angular momenta, ℓ. The result is that the Porter-Thomas fits do not describe the above data very accurately. Since there is not sufficient experimental data to separate by specific quantum numbers, the current method is the best first approach for describing the proton spectroscopic factor distributions in these six nuclei. The fits seem to describe the lower values of the proton spectroscopic factor reasonably well, however.

There are still not sufficient data to describe the probability distribution of an unknown proton spectroscopic factor through the exploration of individual nuclei. For this reason, the spectroscopic factors for the six nuclei from Figs. A.1 - A.6 will be combined into a total set of 1127 proton spectroscopic factors. For the purposes of combining the available data, the proton dimensionless reduced widths will be used instead of the spectroscopic factors. The dimensionless reduced width,

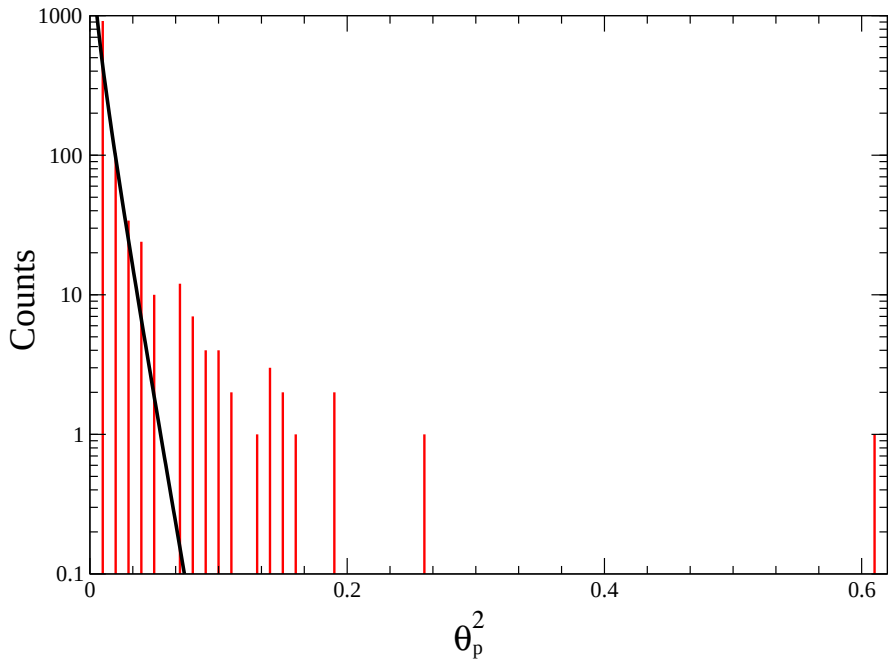

Figure A.7: Histogram of measured dimensionless reduced proton widths for unbound states in ^{24}Mg, ^{28}Si, ^{30}P, ^{32}S, ^{36}Ar and ^{40}Ca. The solid line is a least-squares Porter-Thomas fit to the data resulting in a distribution mean of $\langle\theta_p^2\rangle = 0.0043$.

θ^2, may be calculated from the spectroscopic factor by the following equation from Ref. [1],

$$\theta^2 = C^2 S \theta_{sp}^2 = \gamma^2 \left(\frac{\mu R^2}{\hbar} \right), \tag{A.4}$$

where θ_{sp}^2 refers to the dimensionless single particle reduced width [4]; γ^2 is the reduced width of the level and is usually the value listed in the literature; μ is the reduced mass of the target and projectile and R is the nuclear radius, with $R = 1.25(A_t^{1/3} + A_p^{1/3})$ [4].

Figure A.7 displays a histogram of the combined dimensionless reduced proton widths for levels from all six nuclei. The Porter-Thomas fit to the data resulted in a mean value of $\langle\theta^2\rangle = 0.0043$. A parallel work has found a similar value of $\langle\theta^2\rangle = 0.0045$ [8]. This value of 0.0045 will be adopted for the mean of the Porter-Thomas distribution describing the entire data set.

Another test of how accurately the data is described by a Porter-Thomas distribution is to normalize each data point to its specific Porter-Thomas curve. The reduced widths will be collected into groups sharing the same A and ℓ values. The dimensionless reduced widths in each of these small

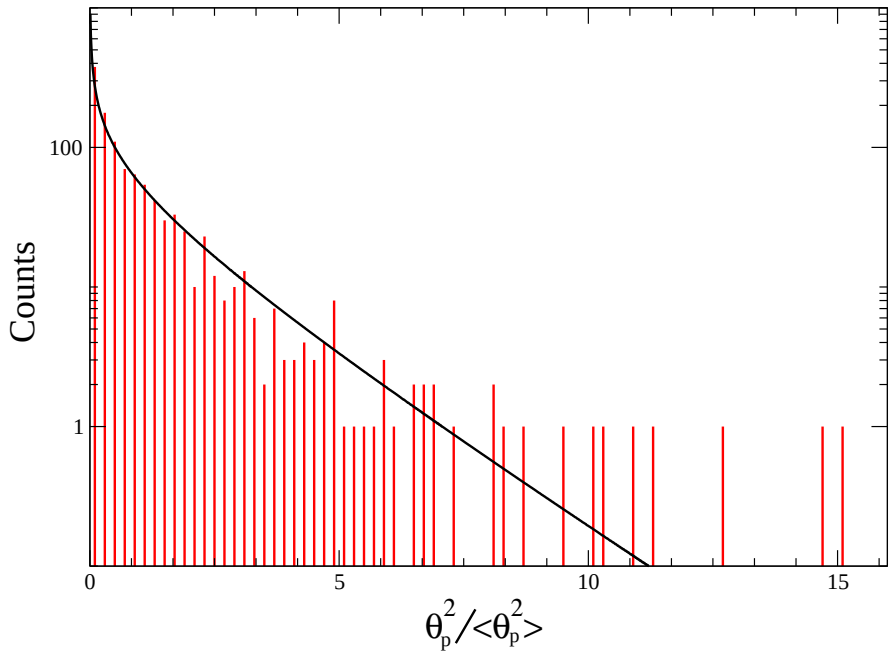

Figure A.8: Histogram of measured dimensionless reduced proton widths for unbound states in ^{24}Mg, ^{28}Si, ^{30}P, ^{32}S, ^{36}Ar and ^{40}Ca. Each θ^2 value is divided by the local average of θ_p^2 for levels of the same A and ℓ values. The solid line represents a Porter-Thomas distribution with mean of $\frac{\theta^2}{\langle\theta^2\rangle} = 1$.

groups will be averaged and each specific value will be divided by its local sample average. The data will then be recombined, producing a larger data set with each point normalized to the mean of its group of common quantum numbers. This results in a global mean of $\frac{\theta^2}{\langle\theta^2\rangle} = 1$. These normalized data are plotted in figure A.8 and appear to be much more accurately described by a Porter-Thomas distribution than the unnormalized data sets. Plots similar to Fig. A.8 are usually found in the literature for exactly this reason. The value of $\langle\theta_p^2\rangle$, however, cannot be determined by fitting $\frac{\theta^2}{\langle\theta^2\rangle} = 1$ and the purpose of this plot is simply to illustrate the fact that the Porter-Thomas distribution is an accurate description of the distribution of dimensionless reduced widths.

A.2 Anodized Targets

The oxygen targets used for this project were made by oxidizing tantalum backings via anodization using oxygen enriched water. Anodization is a well understood process, producing targets of high stability and well defined stoichiometry. It involves dissociating water and combining the resultant

O^{2-} ions with ionized metal. The anodization process follows the chemical reaction [54]:

$$2Ta + 5H_2O = Ta_2O_5 + 5H_2. \tag{A.5}$$

The procedure is to first apply a positive voltage to a Ta backing and to ground another Ta sheet that is isolated from the target backing. These tantalum pieces are each fastened to either side of an anodization chamber. The chamber used for the current work is shown in Fig. A.9. The chamber allows for isolation of the two metal sheets and acts as a container for the volume of water which must span the gap between the Ta sheets. The anodizing voltage will pull electrons off the Ta, forming Ta^{5+} ions, and will also dissociate the water. This will supply the O^{2-} ions. The Ta^{5+} and O^{2-} ions will combine to form a well defined Ta_2O_5 compound [24]. KI crystals should be added to the water prior to anodization in order to facilitate the flow of charged ions and electrons through the solution. The solution should consist of 1 mg of KI per 0.5 mL of water [24].

The thickness of the target is proportional to the anodization voltage chosen. Figure A.10 shows the linear dependence of target thickness on anodization voltage. These data are for the 151 keV resonance in ^{18}O(p,γ)^{19}F and were measured with six ^{18}O enriched targets prepared by Chris Fox. The fit to the data in Fig. A.10 was used to determine the 30 V anodization voltage of the ^{17}O target from Chap. 4. The target thickness saturates very quickly and an anodization time of 2 minutes was chosen to be certain that saturation was reached.

Once an anodization voltage is chosen, the water is inserted into the anodization chamber via a syringe. This fills the gap between the target backing (anode) and the diode metal. After application of the anodization voltage, the target backing is removed from the chamber and should have a very clear oxygen deposition on the surface. The actual color is voltage dependent, but all targets are very bright and uniform. It is important to ensure that the anodization chamber is completely full of water, otherwise there may be non-anodized portions of the target area. These will appear as holes in the oxygen coloring and will result in nonuniform, unusable targets. These nonuniform targets can be fixed by immediately rotating the target backing and re-anodizing it over the same surface. Since the target thickness is only a function of anodization voltage, re-anodization should result in a uniform target as long as the voltage is exactly the same as during the first anodization. Great care should be

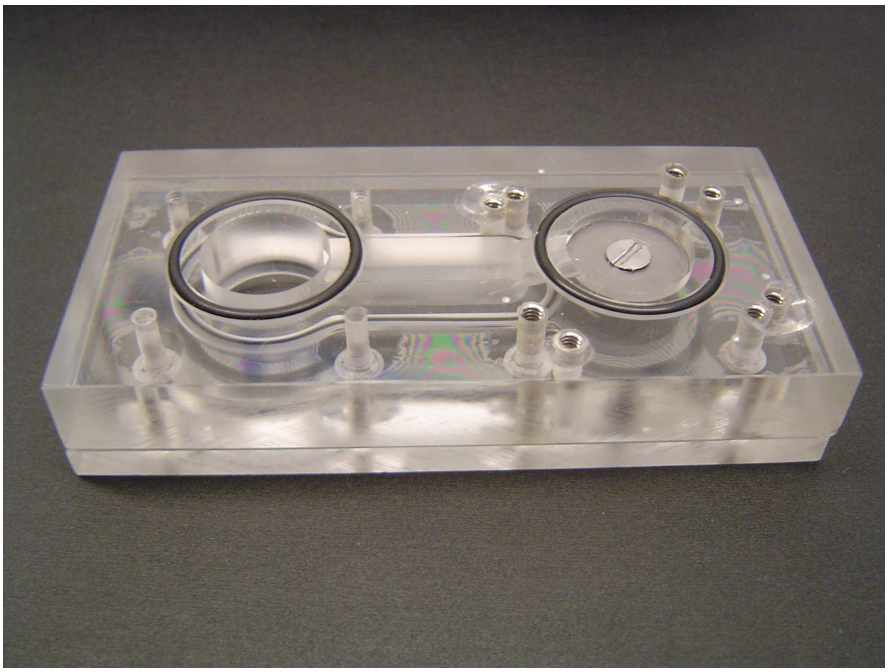

Figure A.9: Anodization chamber used for the production of all of the enriched oxygen targets from the current work.

taken when removing the target backing in order to allow for efficient recollection of the expensive isotopically enriched water.

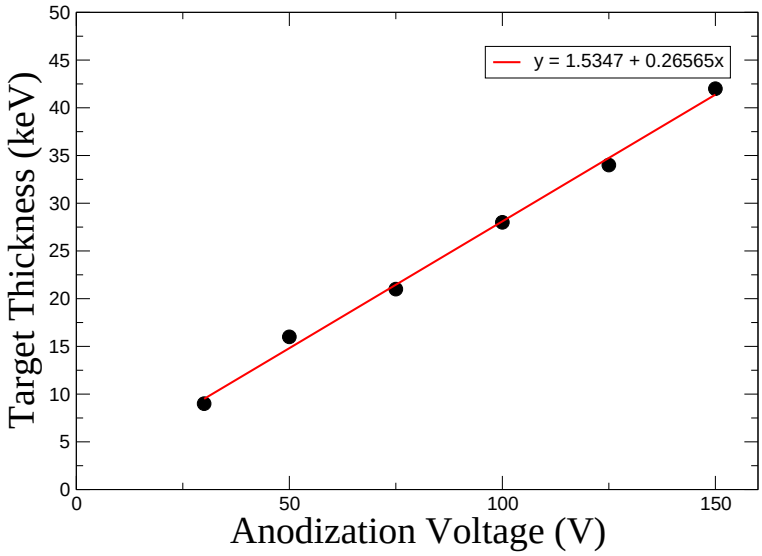

Figure A.10: Target thicknesses of ^{18}O targets made with a range of anodizing voltages. The targets were made and tested by Chris Fox using the E_r^{lab} = 151 keV resonance ^{18}O(p,γ)^{19}F reaction. The data were adopted from his run book.

BIBLIOGRAPHY

[1] C. Iliadis, *Nuclear Physics of Stars* (Wiley-VCH, 2007).

[2] J. Jose, M. Hernanz, and C. Iliadis, Nucleosynthesis in classical novae, Nucl. Phys. A **777**, 550 (2006).

[3] C. Rolfs, *Cauldrons in the Cosmos* (The University of Chicago Press, 1988).

[4] C. Iliadis, Proton single-particle reduced widths for unbound states, Nucl. Phys. A **618**, 166 (1997).

[5] C. Iliadis and M. Wiescher, Spectroscopic factors from direct proton capture, Phys. Rev. C **69**, 064305 (2004).

[6] C. Rolfs, Spectroscopic Factors from Radiative Capture Reactions, Nuc. Phys. A **217**, 29 (1973).

[7] C. Fox *et al.*, Thermonuclear reaction rate of $^{17}\mathrm{O}(p,\gamma)^{18}\mathrm{F}$, Phys. Rev. C **71**, 055801 (2005).

[8] R. Longland *et al.*, Charged-Particle Thermonuclear Reaction Rates: I. Monte Carlo Method and Statistical Distributions, To be submitted for publication .

[9] W. Fowler and F. Hoyle, Neutrino processes and pair formation in massive stars and supernovae, Astrophys. J. Suppl. **9**, 201 (1964), app. C.

[10] P. M. Endt, Energy levels of A = 21-44 nuclei (VII), Nucl. Phys. A **521**, 1 (1990).

[11] P. M. Endt, Supplement to energy levels of A = 21-44 nuclei (VII), Nucl. Phys. A **633**, 1 (1998).

[12] T. Rauscher and F. K. Thieleman, Astrophysical Reaction Rates from Statistical Model Calculations, Atomic Data and Nucl. Data Tables **75**, 1 (2000).

[13] C. Iliadis, J. D'Auria, S. Starrfield, W. Thompson, and M. Wiescher, Proton-induced Thermonuclear Reaction Rates for A=20-40 Nuclei, Astrophys. J. Supp. Series **134**, 151 (2001).

[14] C. Angulo *et al.*, A compilation of charged-particle induced thermonuclear reaction rates, Nucl. Phys. A **656**, 3 (1999).

[15] J. R. Newton *et al.*, Gamow peak in thermonuclear reactions at high temperatures, Phys. Rev. C **75**, 045801 (2007).

[16] J. R. Newton, R. Longland, and C. Iliadis, Matching of experimental and statistical-model thermonuclear reaction rates at high temperatures, Phys. Rev. C **78**, 025805 (2008).

[17] A. Coc, M. Hernanz, J. Jose, and J. P. Thibaud, Influence of new reaction rates on ^{18}F production in novae, Astron. Astrophys. **357**, 561 (2000).

[18] C. Fox *et al.*, Explosive Hydrogen Burning of ^{17}O in Classical Novae, Phys. Rev. Lett. **93**, 081102 (2004).

[19] A. Chafa *et al.*, Hydrogen Burning of ^{17}O in Classical Novae, Phys. Rev. Lett. **95**, 031101 (2005).

[20] A. Chafa *et al.*, Erratum: Hydrogen Burning of ^{17}O in Classical Novae, Phys. Rev. Lett. **96**, 019902 (2006).

[21] A. Chafa *et al.*, Experimental determination of the ^{17}O$(p,\alpha)^{14}$N and ^{17}O$(p,\gamma)^{18}$F reaction rates, Phys. Rev. C **75**, 035810 (2007).

[22] H. Becker *et al.*, Hydrogen depth profiling using ^{18}O ions, Z. Phys. A **351**, 453 (1995).

[23] J. Ziegler and J. Biersack, computer program SRIM, 2003.

[24] D. Phillips and J. Pringle, Preparatoin of isotopic oxygen targets via the anodic oxidation of tantalum, Nucl. Instrum. Methods **135**, 389 (1976).

[25] B. H. Moazen *et al.*, Measurement of the 183 keV resonance in ^{17}O$(p,\alpha)^{14}$N using a novel technique, Phys. Rev. C **75**, 065801 (2007).

[26] S. Agostinelli *et al.*, Nucl. Inst. Methods A **506**, 055801 (2003), We used the low-energy extensions of Geant4 according to www.ge.infn.it/GEANT4/lowE/index.html; for the low-energy library of α-particle stopping powers we employed the results of: ICRU Report 49, International Commission on Radiation Units and Measurements, Bethesda, MD, USA (1993).

[27] J. R. Newton, C. Iliadis, A. E. Champagne, R. Longland, and C. Ugalde, Remeasurement of the 193 keV resonance in ^{17}O$(p,\alpha)^{14}$N, Phys. Rev. C **75**, 055808 (2007).

[28] J. R. Newton *et al.*, Measurement of ^{17}O(p,γ)^{18}F between the narrow resonances at E_r^{lab}=193 and 519 keV, submitted to Phys. Rev. C .

[29] R. Longland, C. Iliadis, A. E. Champagne, C. Fox, and J. R. Newton, Nuclear astrophysics studies at the LENA facility: The γ-ray detection system, Nucl. Inst. and Meth. A **566**, 452 (2006).

[30] T. M. Semkow, G. Mehmood, P. P. Parekh, and M. Virgil, Coincidence summing in gamma-ray spectroscopy, Nucl. Inst. and Meth. A **290**, 437 (1990).

[31] R. Longland, S. Daigle, J. Cesaratto, C. Iliadis, and J. R. Newton, Triangle Universities Nuclear Laboratory Report No., , 2009 (unpublished).

[32] R. Longland, Low Yield Measurements at the Laboratory for Experimental Nuclear Astrophysics, (2004), M. Phys. Thesis, University of Surrey.

[33] D. R. Tilley, H. R. Weller, C. M. Cheves, and R. M. Chasteler, Energy levels of light nuclei A = 18-19, Nucl. Phys. A **595**, 1 (1995).

[34] C. Rolfs, A. M. Charleworth, and R. E. Azuma, Nuclear structure of ^{18}F :(I). Radiative capture experiments, Nucl. Phys. A **199**, 257 (1973).

[35] R. E. Brown, Experimental Study of the $^{17}O(p,a)^{14}N$ Reaction and a Calculation of the Rate of this Reaction in the CNO Cycle in Stars, Phys. Rev. **125**, 347 (1962).

[36] W. E. Kieser, R. E. Azuma, and K. P. Jackson, The ^{17}O$(p,\alpha)^{14}$N reaction: Physics and astrophysics, Nuc. Phys. A **331**, 155 (1979).

[37] P. D. Parker, ^{14}N(α,γ)F^{18} Reaction, Phys. Rev. **173**, 1021 (1968).

[38] I. Berka, K. P. Jackson, C. Rolfs, A. M. Charlesworth, and R. E. Azuma, Isospin mixing of the 5605 and 5668 keV states in ^{18}F in the light of a new state at 5603 keV, Nucl. Phys. A **288**, 317 (1977).

[39] H. Becker, W. E. Kieser, C. Rolfs, H. P. Trautvetter, and M. Wiescher, Resonance strengths of some light nuclei, Z. Phys. A **305**, 319 (1982).

[40] J. C. Blackmon *et al.*, Measurement of the ^{17}O(p,α)^{14}N Cross Section at Stellar Energies, Phys. Rev. Lett. **74**, 2642 (1995).

[41] H. B. Mak *et al.*, The alpha widths of the 5603, 5605 and 5668 keV states in ^{18}F, Nuc. Phys. A **343**, 79 (1980).

[42] V. Landre *et al.*, ^{17}O(^{3}He,d)^{18}F reaction and its implication in the ^{17}O destruction in the CNO cycle in stars, Phys. Rev. C **40**, 1972 (1989).

[43] C. Rolfs and W. S. Rodney, Hydrogen burning of ^{17}O in the CNO cycle., Nucl. Phys. A **250**, 295 (1975).

[44] J. C. Sens, A. Pape, and R. Armbruster, A spectroscopic study of ^{18}F (II). The ^{17}O(p,γ)^{18}F reaction, Nucl. Phys. A **199**, 241 (1973).

[45] J. R. Vanhoy, *Proton resonance spectroscopy in ^{24}Mg*, PhD thesis, Duke University, 1986.

[46] J. R. Vanhoy, E. G. Bilpuch, C. R. Westerfeldt, and G. E. Mitchell, Proton resonances in ^{24}Mg from E$_x$=12.7 to 15.7 MeV, Phys. Rev. C **36**, 920 (1987).

[47] R. O. Nelson, *Proton resonance spectroscopy in ^{28}Si and ^{30}P*, PhD thesis, Duke University, 1983.

[48] R. O. Nelson, E. G. Bilpuch, C. R. Westerfeldt, and G. E. Mitchell, Proton resonance in ^{28}Si from E$_x$=12.5 to 13.4 MeV, Phys. Rev. C **29**, 1656 (1984).

[49] R. O. Nelson, E. G. Bilpuch, C. R. Westerfeldt, and G. E. Mitchell, Proton resonances in ^{28}Si from E$_x$=13.4 to 14.5 MeV, Phys. Rev. C **30**, 755 (1984).

[50] D. F. Fang, *Proton resonance spectroscopy in ^{32}S*, PhD thesis, Duke University, 1987.

[51] D. F. Fang, E. G. Bilpuch, C. R. Westerfeldt, and G. E. Mitchell, Proton resonances in ^{32}S from E$_x$=9.83 to 12.74 MeV, Phys. Rev. C **37**, 28 (1988).

[52] W. K. Brooks, *Proton resonance spectroscopy in ^{36}Ar*, PhD thesis, Duke University, 1988.

[53] B. J. Warthen, *Proton Resonance Spectroscopy in ^{40}Ca*, PhD thesis, Duke University, 1987.

[54] S. Wosu, Anodic oxidation of tantalum in water and biological solutions using current limiting constant voltage method, Journ. of Mater. Sci. **42**, 4087 (2007).